Projectional Radiography of a Supercritical Fluid

Experimental-numerical feasibility study

J. W. Blokker

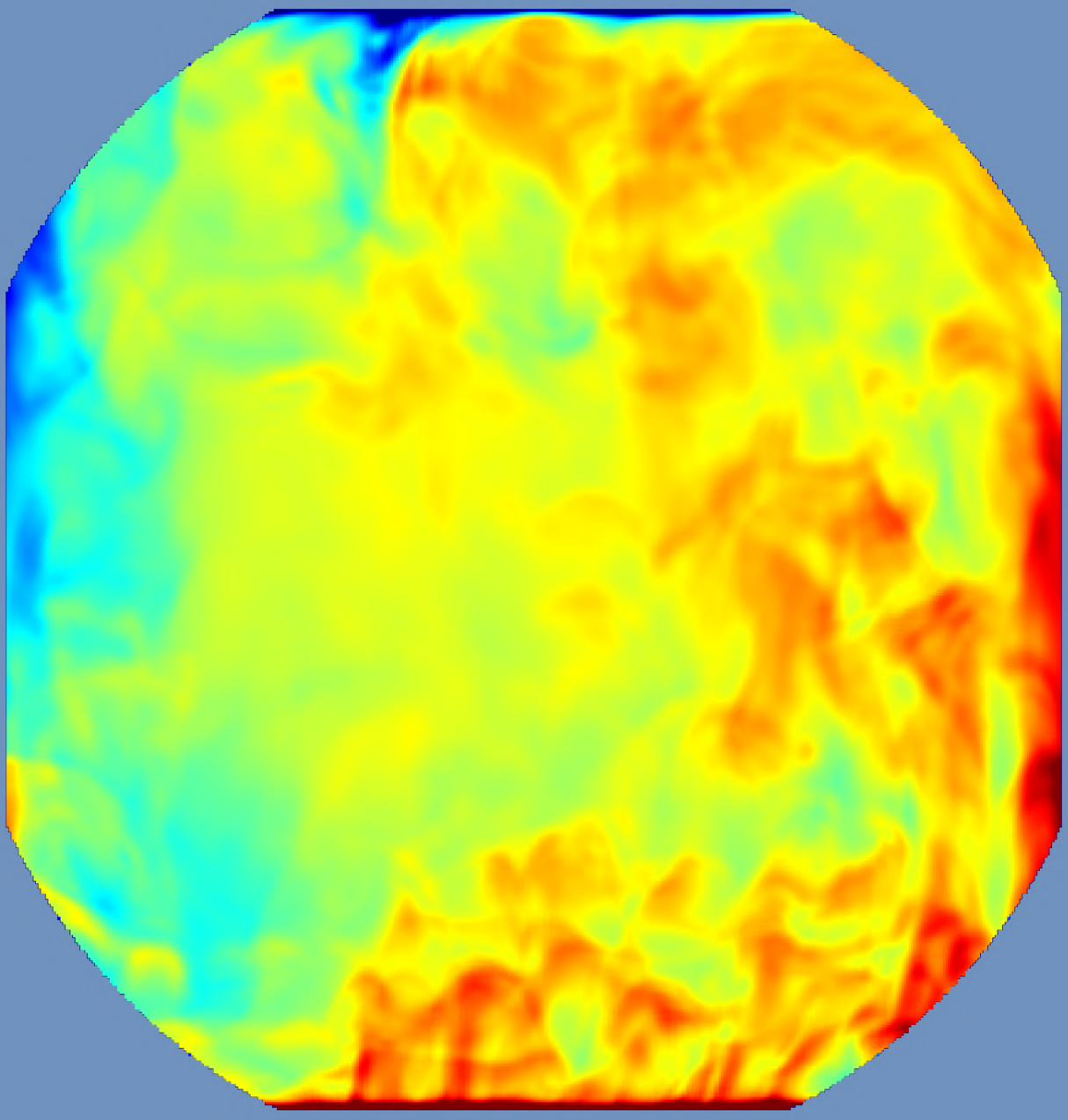

Delft University of Technology

TU Delft

Projectional Radiography of a Supercritical Fluid

Experimental-numerical feasibility study

by

J. W. Blokker

to obtain the degree of Master of Science
at the Delft University of Technology,
to be defended publicly on Tuesday January 1, 2013 at 10:00 AM.

Student number: 4306120
Supervisor: dr. ir. M. Rohde, TU Delft

TU Delft Delft University of Technology

Preface

Abstract

Contents

1

Introduction

1.1. Background

DISCOVERED in 1822 by Baron Charles Cagniard de la Tour [1], super critical (SC) fluids have become a staple in many branches of industry, being used for a multitude of applications. A few examples are SC fluid extraction, chromatography and impregnation [1, 2]. Besides these applications, SC fluids can also be used in energy generation, where they function as cooling fluids for power plants. Using SC fluids allows the plants to generate energy more efficiently, as increasing the temperature difference between source and sink increases the efficiency. Coal-fired power plants using this technology are already in use and their designs continue to be improved, with their efficiency expected to reach approximately 50-55% in the near future [3]. Although there are none in use at the moment of writing, research is ongoing with the aim of designing a nuclear power plant which uses supercritical fluids, the so-called supercritical water-cooled reactor (SCWR) [4]. The SCWR is not a recent concept. As early as the 1960's research has been done, continuing into the 1970's [5–10]. After this period interest declined for a period of twenty years, until it rose again at the start of the 1990's. This design is one of the six Generation IV [11] nuclear reactor designs currently in development and boasts multiple advantages over current nuclear power plants, for example its higher efficiency (about 45% vs. 35%) [12].

Simply put SCWRs are a combination of a traditional Light Water Reactor (LWR) and a supercritical Fossil Power Plant (FPP) [13]. These reactors use high temperature and pressure (374 °C and 22.1 MPa respectively) water as coolant and as such operate above the critical point of water, making it supercritical. An overview of a typical SCWR system is shown in figure 1.1(a). The high temperature of the supercritical water when it leaves the core is what allows the thermal efficiency of the SCWR to be considerably higher than that of conventional LWRs.

Although this design seems promising, there are still many challenges to overcome before it can be implemented. A major one is the validity of current models for calculating supercritical heat transfer. At SC conditions the material properties of fluids can change very rapidly with a small change in temperature. An example of this can be seen in figure 1.1(b), where the density of water around 647 K is displayed. It is clear that the density decreases rapidly between 646 and 648 K. Similar extreme behaviour can be observed for other material properties, such as the viscosity or heat capacity. As a result the behaviour of fluids at SC conditions is very complex and calculations of the heat transfer therefore very complicated compared to the situation at sub-critical conditions. Experimental studies have been done in the past, mapping the heat transfer in pipe and annular geometries. Unfortunately, the results of these studies are very specific and cannot be applied to different situations. Besides experimental studies theoretical research has also been done, but the resulting models are still unable to accurately predict heat transfer.

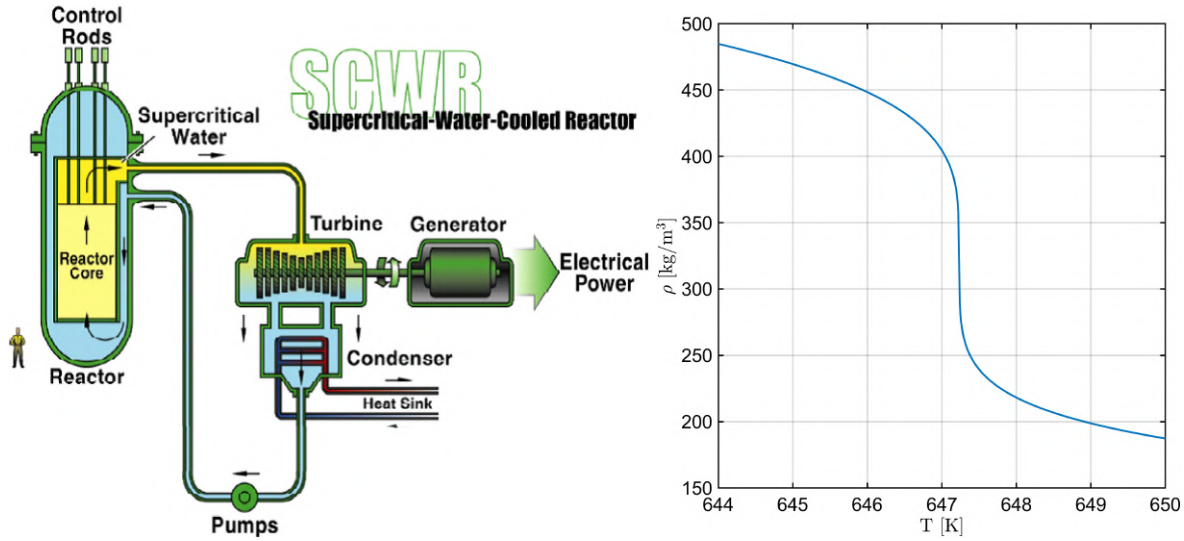

(a) A typical SCWR system [13].

(b) Density of water as a function of temperature at a constant pressure of 22.1 MPa. Values retrieved from the CoolProp database [14].

Figure 1.1: Overview of a typical SCWR (left) and the density of water (right) around 647 K at a pressure of 22.1 MPa.

1.2. Prior research

ACCORDING to an overview made by Yoo [15], in which they present the progress made in understanding the mechanics behind the behaviour of SC fluids, buoyancy, flow acceleration, and the sharp variations in temperature dependent properties are substantial contributors to the complex nature of supercritical fluids. From this study it is concluded that the majority of experimental studies were done with regards to heat transfer, while only a small number of studies looked into the fluid mechanics of SC fluids as the development of the techniques required for such research has been limited by technical difficulties and high expenses. As such the call is made for the development of techniques that allow for more advanced visualization and measurement of SC fluids.

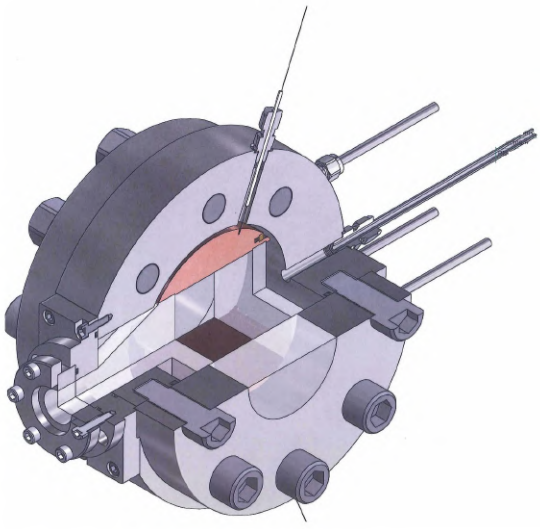

Figure 1.2: Picture of the Rayleigh-Bénard convection cell used by Valori et al. [16]

Since then multiple studies have been done in this direction, one of which by Valori et al. [16]. The aim of this study was to see if it is possible to perform non-intrusive velocity measurements using particle image velocimetry (PIV) in a supercritical fluid. In order to do so a system was designed in which a SC fluid flow driven by Rayleigh-Bénard (RB) convection could be studied, displayed in figure 1.2. The fluid selected for this study was fluoroform (CHF_3), also known as trifluoromethane or by its ASHRAE number R-23. This compound was chosen due to the relative ease with which it can be brought into supercritical state, as its critical point is at approximately 4.8 MPa and 299 K [17]. Using this method they measured both instantaneous and time-averaged velocity fields in the mid plane of the central cubic cell. As SC fluids are associated with sharp changes in density over small length scales, a preliminary study was done to identify the effects of the resulting optical distortion using background-oriented schlieren (BOS).

Three cases were studied, characterized by the position in the supercritical region; near the liquid phase, in the region with the highest density gradient and near the gas phase. The results showed in all cases the

existence of a large-scale-circulation (LSC) roll which covered the entire mid plane. These kind of structures are commonplace in RB convection. Although these results provided greater insight into the behaviour of SC liquids, the principle behind PIV resulted in a 2D projection of a 3D flow structure. According to literature it is possible to combine BOS with the conjugate gradient method (CGM) to calculate density values [18]. In the case of a two dimensional flow local density values can be calculated, while only integrated density values can be calculated for a three dimensional flow. Ultimately, the BOS results were not combined with the CGM to calculate the integrated densities as this was not relevant to the project. Although this is still an option for future research there might be another possibility to investigate density fields in the cell: radiography.

Radiography is an imaging technique that uses (non-)ionizing radiation to form images of an object. Currently, the most commonly used type of radiation for this purpose is X-ray, being used in both medical and industrial applications. Part of the incoming radiation is either absorbed or scattered in the object, with the amount of attenuation largely dependent on the density of the object. When the object is irradiated from only one direction it is called projectional radiography (PR) and the result is a 2D image. 3D images can be generated by irradiating the object from many different angles after which the results can be processed into a three-dimensional image. This is called computed tomography (CT). The main benefit of CT compared to PR is that CT gives insight into the internal structure of the object, while PR only gives an 'average' density along a line perpendicular to the plane of the image.

Study of supercritical fluids using radiography has been done before, although most of these studies used neutron imaging techniques, e.g. those by Balaskó et al. [19] and Maxim et al. [20] who studied supercritical water. X-rays also have been used by Kawamoto et al. [21], using a synchrotron to generate X-rays to study magmatism or by Chaudhary et al. [22], who used a very specialized device that allowed for high-resolution X-ray computed tomography (HRXCT) and radiography to perform wettability measurements. A disadvantage of these techniques is that it is either difficult to get access to these resources, as they are limited in availability and in high demand, causing long wait times or that the equipment necessary is very expensive. Furthermore, there is often a limitation in sample size, geometry etc. when using these techniques.

A solution to these problems is to use a technique that is more easily accessible. At the moment of writing and to the authors knowledge radiographical imaging using conventional X-ray tubes and detectors as seen in hospitals has never been performed on a supercritical fluid. Some advantages of using these relatively 'simple' pieces of equipment are lower cost, ease of access and the ability to completely cover large samples with an X-ray beam, irradiating all parts simultaneously. This comes at a cost of resolution, as the detectors used in these setups have pixels that are larger in size than those of specialized detectors as they need to be considerably larger to be able to generate an image that covers as much of the sample as possible. Using X-ray radiography also has an advantage compared to BOS, as the refractive index for X-ray radiation is very close to unity for any material [23], so optical distortion will very likely be negligible.

1.3. Research goals and report outline

THE original aim of this research was to see if it is possible to use common radiographical equipment to perform non-intrusive measurements on the density field of a supercritical fluid and if the fine structures of such a field can be resolved. Furthermore, if this was possible the boundaries would be pushed to study its limitations and to see when all details are lost. To this purpose both instantaneous and time-averaged measurements of the fluid would be performed. The system studied would be the same as studied by Valori et al. [16], displayed in figure 1.2. For a detailed discussion see chapter four of their paper. Unfortunately, due to the steel container surrounding the central cubical cell it would only be possible to irradiate the center from the side with the windows, as the steel shields the parts of the detector directly behind it from all direct radiation.

Unfortunately, due to the emergence of COVID-19 and the subsequent lockdown in The Netherlands all experimental work at the TU Delft had to be stopped and staff and students alike had to start working from home. Only some preliminary measurements had been done at this point. As a result this project could not be continued in its current form and had to be revised so it could be done from home. The decision was made that the project would be mainly numerical and would focus on simulating the planned measurements to get an indication of the resulting image quality and the effect of noise and similar phenomena on the ability to resolve details. As mentioned earlier it should in theory be possible to use the results from the BOS measurements by Valori et al. [16] in combination with the conjugate gradient method to calculate integrated density

values. In the case that simulation of the measurements is finished early an option would be to actually calculate these values. The results can then be used to get an idea of the density field in the cell or in the future compared to the results from actual measurements. However, it became quickly clear that it was very unlikely that there would be enough time for this and so this idea was scrapped.

In order to complete the new objectives the following research questions have to be answered:

- Is it possible to construct a model that accurately simulates projectional radiography measurements on the RB-cell?
- If so, will these measurements result in images that contain enough information to study the density structures in the cell?
- Can the results of the simulation be used to quantify or predict errors due to noise, scattering etc. and help correct for this in the actual measurements?

In the next chapter some physical background information will be given regarding X-ray imaging and its most important aspects alongside some information on supercritical fluids. In chapter 3 the experimental approach is explained, including the original project plan, the preliminary measurements and additional measurements. In chapter 4 the numerical approach is discussed, detailing the different parts of the model and approximations made accompanied by pseudo-code. Following that, in chapter 5 the results are presented and discussed. Finally, in chapter 6 the research questions are answered, a conclusion is presented and recommendations and advice are given for future research.

2

Physical background information

In this chapter background information on X-ray imaging supercritical fluids are given. The first section explains the process of creating images using X-rays and is subdivided in three parts each examining a major component of this imaging technique. The second section gives a general overview of supercritical fluids.

2.1. X-ray imaging

The history of using X-rays as an imaging tool starts with their discovery on November 8, 1895 by Wilhelm Conrad Roentgen, who would later be awarded the first Nobel Prize in Physics for his discovery. Just one year after his discovery the first X-ray machine was installed in a medical facility, indicating how much of a breakthrough this technique was for medical diagnostics. Ever since then, technology has continued to be improved. For the interested reader Behling [24] gives a detailed overview of this process up until 2007.

X-rays are part of the electromagnetic spectrum, occupying the high-energy part of the spectrum together with gamma rays. There is no official consensus on how to differentiate between these two forms of radiation as terminology differs between scientific disciplines. In astrophysics the distinction is made based on energy, with photons with an energy above 100 keV defined as gamma rays and those with an lower energy as X-rays. In physics the distinction is made based on origin of the photons; gamma rays originate from the nucleus of an atom and X-rays from the electron cloud surrounding it. This second definition will be used in this report.

X-ray imaging is a form of attenuation or transmission imaging. The key principle behind this technique is that particles or waves passing through an object interact with its matter and as a consequence are reduced in intensity. The strength of this attenuation is dependent on the material and density of the matter the particles or waves interact with as well as their energy. As a result, a beam that was homogeneous in intensity before entering the object emerges with a space dependent intensity out of the object. The differences in intensity result in contrast when detected by the image receptor, forming an image. In figure 2.1 the first medical image taken by Roentgen is displayed. This photo, taken just over a month after his discovery of X-rays, shows his wife's hand. It is clear that the bone in the fingers attenuates the incoming X-rays more than the surrounding tissue, resulting in a high contrast.

The process of creating an image using X-rays can be divided into three sequential parts. First X-rays are produced, usually by accelerating and then decelerating electrons. After their creation a fraction of the X-rays travel towards the object that is studied. Entering the object, part of the X-rays is attenuated which is the second part. Finally, unattenuated X-rays emerge from the object and travel to the detector, where a fraction is converted to a measured signal.

2.1.1. X-ray production & characteristics

X-ray production

The first man-made X-rays were produced by stopping high-energy electrons in a target, usually glass. For this reason the radiation produced was called bremsstrahlung, which translates to braking radiation. As a

Figure 2.1: First X-ray image created by Roentgen, showing his wife's hand [25].

electron approaches a nucleus it experiences its electric field and is deflected from its original trajectory due to the Coulomb force. Due to the deflection the electron is decelerated and it loses kinetic energy. As energy should be conserved this energy is emitted as X-rays. A depiction of this process can be seen in figure 2.2 where a electron is deflected and emits a photon with energy $h\nu$. When traveling through the target material an electron can experience one or more 'collisions', losing its entire or a fraction of its kinetic energy at each interaction. As a result the energy spectrum of the emitted X-rays is continuous and is only limited in the maximum allowed X-ray energy by the Duane-Hunt law, which states that the maximum energy of the X-rays can not be larger than the kinetic energy of the electrons bombarding the target.

Besides bremsstrahlung there is another process that produces X-rays as a result of high-energy electrons interacting with matter. Incident electrons not only interact with the nuclei of target material, but can also interact with the surrounding electrons. If the energy of the incoming electron is higher than the binding energy of the orbital electron it collides with it can eject it from its shell and ionize the atom. This leaves a vacancy in the shell it was ejected from. Following this, an electron from an outer shell will fall down to fill that vacancy, emitting a photon. This process is illustrated in figure 2.3. Here an electron with kinetic energy E_0 collides with an electron in the K-shell transferring an energy ΔE. The primary electron continues on a altered path with energy $E - \Delta E$. The secondary electron ejected from the K-shell has a kinetic energy of $\Delta E - E_k$, where E_k is the binding energy of the K-shell. The hole created in the K-shell can now be filled by an electron from an outer shell, in this case the L- or M-shell. As the electrons in the shells can only occupy the allowed quantum states and the Pauli exclusion principle states that no two electrons can occupy the same quantum state the energies of the photons emitted have discrete energies, equal to the difference in binding energies of the shells. For example, an electron falling from the L-shell to the K-shell emits a photon with energy $h\nu = E_K - E_L$. As the binding energies of the shells are different for each element the energies of the photons emitted in this process are also element dependent. For heavier elements the differences in binding energies are high enough that the photons emitted can be considered X-rays. These are called characteristic X-rays. Furthermore the orbital electron that falls down leaves a hole in its own shell. If the hole is not located

in the outer-shell an electron can again fall down to fill the vacancy, also emitting an characteristic X-ray. This process, called a characteristic cascade, continues until the hole is located in the outer shell of the atom. The cascade does not necessarily happen in a fixed order. A vacancy in the K-shell is most likely to be filled by an electron from the L-shell, but transitions from higher orbitals are also possible albeit with much lower probabilities.

Although in most cases the excessive energy of a transition from higher to lower orbital is radiated away as a photon it is also possible that this energy is transferred to an outer-shell electron, ejecting it from its shell. This is called the Auger effect and the resulting electrons are called Auger electrons. The energy of such an electron is equal to the difference in initial and final binding energy of the transitioning electron minus the binding energy of the ejected electron. In the case of an electron transitioning from the L-shell to the K-shell and the Auger electron being ejected from the M-shell this energy is equal to $(E_k - E_L) - E_M$.

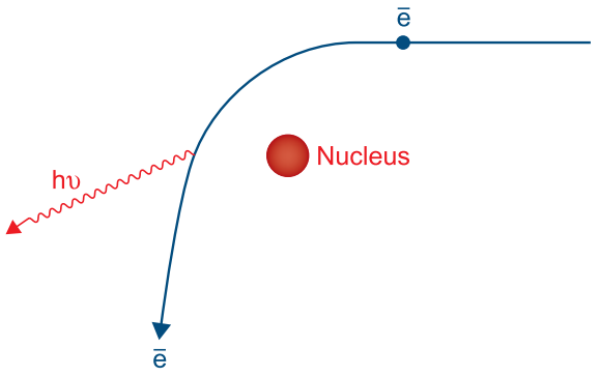

Figure 2.2: Bremsstrahlung process [26].

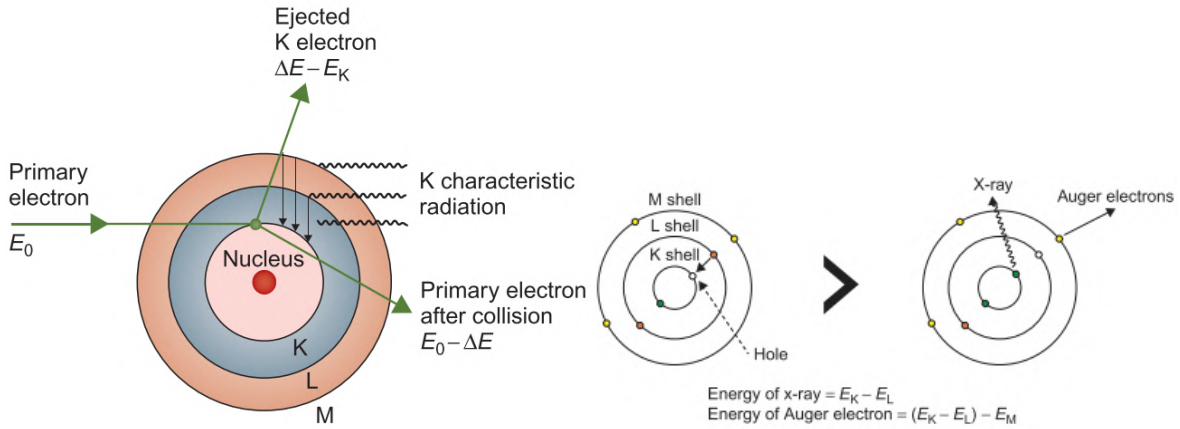

(a) Ejection of a secondary electron due to electron-electron interaction.

(b) Electron transition from a higher to lower orbital resulting in the creation of a characteristic X-ray or the ejection of an Auger electron.

Figure 2.3: Production of characteristic X-rays and Auger electrons [26].

In modern diagnostic imaging the most common machine to produce X-rays is the X-ray tube. A simplified diagram showing the most important components can be seen in figure 2.4. Such a tube is essentially almost the same as the device used by Roentgen for his discovery, although much more sophisticated. Inside the tube there is a vacuum. Electrons are emitted from the cathode filament due the thermionic emission. A material that is often used for the filament is tungsten because of its high melting point (3370 °C). After emission, the electrons are accelerated towards the anode due to a high voltage applied between the cathode and anode. The anode is covered by the target, which in most cases is also made from tungsten. There are two main reasons for choosing this material. First of all, the efficiency of producing bremsstrahlung scales linearly with the atomic number Z while the energy loss per atom depends on the square of the atomic number (Z^2) [26].

Heavier elements are therefore better for production of X-rays. The second reason is again its high melting point. The efficiency of a material at producing X-rays can be approximated by

$$\eta = 9 \times 10^{-10} ZV \tag{2.1}$$

where V is the potential between the cathode and anode in volts [27]. Efficiency is in this case defined as the ratio between the output energy of the X-rays and the input energy of the electrons. For tungsten (Z=74) with a tube potential of 100 kV this gives an efficiency of less than 1%. The remaining electron energy is converted to heat, necessitating the target material to have a high melting point. The electrons strike the target, producing X-rays which can only escape through the window as the lead casing absorbs all X-rays emitted in other directions. In most cases the X-ray tube includes a filter behind the window. The purpose of this filter is to attenuate the lower-energy X-rays as they would all be absorbed in the target, yielding no contribution to image creation but would contribute to the total dose received by for example a patient.

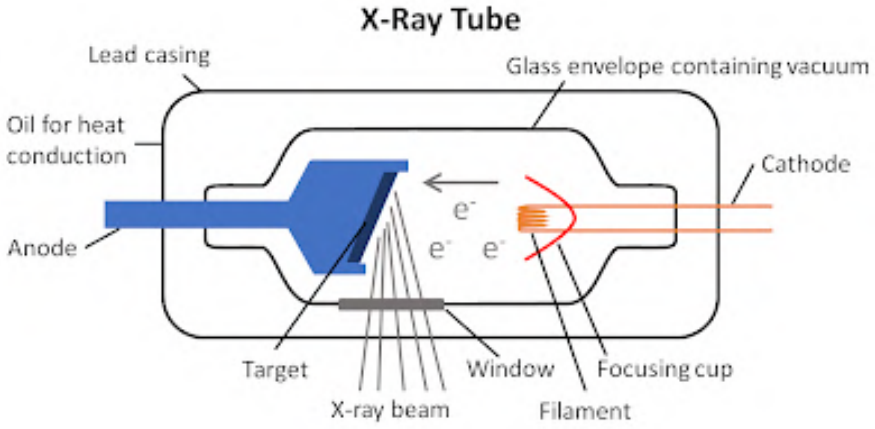

Figure 2.4: Diagram of an X-ray tube [28].

In order to create images as sharp as possible the focal spot, the area where the X-rays emerge from, should be as small as possible. To minimize this area the electron beam has to be as narrow as possible, but this means the heat generation is very localized which can present a problem. A solution to this problem is to place the target at an angle as depicted in figure 2.5. By placing the target at an angle the effective focal spot size is smaller than the actual focal spot size.

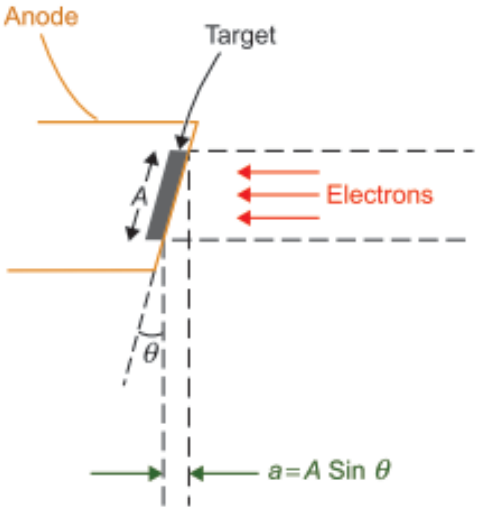

Figure 2.5: Diagram of an X-ray tube target placed at an angle to reduce effective focal spot size [26].

X-ray characteristics

Figure 2.6 shows simulated spectra of filtered X-rays produced in a tungsten target for tube voltages from 80 to 140 kV. The spectra consist of the continuous X-ray distribution corresponding to bremsstrahlung superimposed by the discrete energy peaks of the characteristic X-rays. It is easy to see that the maximum X-ray energy is indeed limited by the tube voltage. As the tube voltage increases the characteristic peaks increase drastically in intensity, but as they are very narrow they do not contribute much to the total integrated intensity. For example, at 140 kV the contribution of the characteristic X-rays is less than 7% of the total intensity.

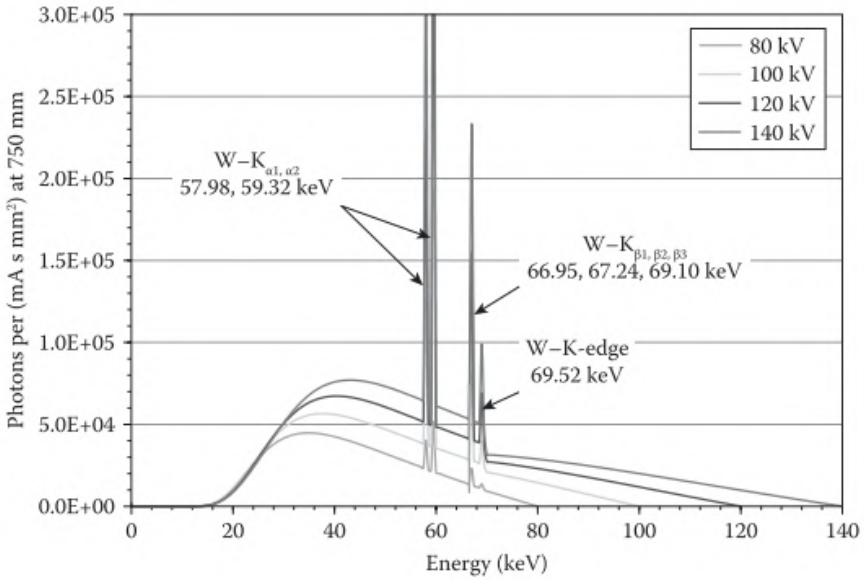

Figure 2.6: Simulated spectra of X-rays produced in a tungsten target at an angle of 10° filtered by 2 mm of aluminium for various tube voltages. The X-rays are emitted along the central beam axis [24].

Ideally, the radiation emitted by an X-ray tube would be isotropic, meaning that the X-rays are emitted in all directions with equal probability and that beam intensity would only depend on the distance from the X-ray tube. Unfortunately this is not true. Using classical physics, the radiated power per unit solid angle of a decelerating electron is given by

$$\frac{dP}{d\Omega} = \frac{q^2 a^2}{4\pi c^3} \sin^2\theta \tag{2.2}$$

where q is the electron charge, a the acceleration, c the speed of light and θ the angle with the forward direction. According to this equation, energy is not radiated equally in all directions, but has peaks in intensity at angles perpendicular to the acceleration. If the velocity of the electron is small compared to the speed of light this equation can be used quite accurately. Electrons however should be considered relativistic particles if their kinetic energy is higher than 16 keV, which is almost always true in diagnostic imaging. Instead of a Galilean transform the Lorentz transform has to be used to change the frame of reference and equation 2.2 changes to

$$\frac{dP}{d\Omega} = \frac{q^2 a^2}{4\pi c^3} \frac{\sin^2\theta}{(1-\beta\cos\theta)^5} \tag{2.3}$$

for acceleration parallel to the velocity. Here β is the ratio between the velocity of the electron and the speed of light. As β increases the angular distribution becomes more and more enhanced in the forward direction. The effect of this can be seen in figure 2.7, where the angular factor $\frac{\sin^2\theta}{(1-\beta\cos\theta)^5}$ is illustrated for increasing tube voltages and electron velocities. The particle acceleration is assumed constant.

This effect is a great tool for radiation therapy as forward enhancement aids in generating very narrow radiation beams and the conversion efficiency increases at higher tube voltages. X-ray tubes that are used for radiation therapy therefore use thin electron-opaque, X-ray transparent transmission targets. Conversely, for diagnostic imaging this effect is not particularly useful for multiple reasons given by Behling [24] in section 2.6 and only 'reflected' X-rays are used. In order to increase efficiency thick targets are used. The angular distribution of X-rays generated in a thin target is illustrated in figure 2.8 for tube voltages ranging from 100

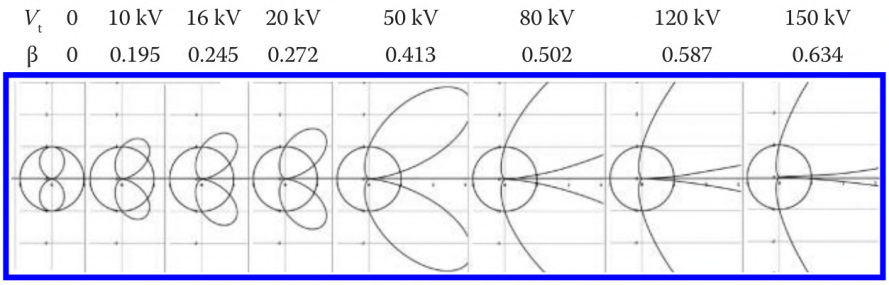

Figure 2.7: Effect of higher tube voltage and particle velocity on the angular distribution of radiated energy by an electron [24].

kV to 20 MV. It should be noted that the distribution of the 'reflected' X-rays is less anisotropic than that of the X-rays in the forward direction. Furthermore, the angular distribution is also dependent on the energy of the X-rays. Due to the Duane-Hunt limit high-energy X-rays can only be generated if the incoming electron still has most of its kinetic energy and thus can only be created during the first couple of collisions. Consequently the electrons still 'remember' where they came from. X-rays with a lower energy can still be generated after many collisions, which result in the electrons diffusing and 'forgetting' their origin. This results in the distribution of X-rays becoming more isotropic as their energy decreases. Measurements by Gonzales et al. [29] confirmed this for the forward direction.

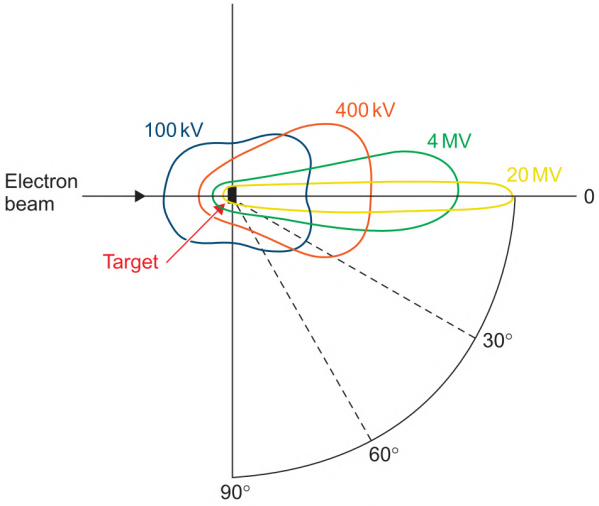

Figure 2.8: Schematic illustration of the angular distribution of bremsstrahlung X-rays generated in a thin target [26].

In contrast to bremsstrahlung X-rays characteristic X-rays do not originate from high-speed electrons but from atoms in the target that can be viewed to be at rest and in the same inertial frame as the observer. Characteristic X-rays therefore do not experience relativistic effects and are independent of tube voltage, resulting in an isotropic emission.

Besides the relativistic effect influencing the angular distribution of bremsstrahlung there is another effect that influences the distribution for both continuous and characteristic X-rays. This is called the heel effect, named after its angular distribution profile. Examples of this profile can be seen in figure 2.9(b). Because X-rays are generated at various depths in the X-ray tube target they have to travel to the target surface to escape. This results in target-intrinsic attenuation. X-rays that emitted at an smaller angle with respect to the target surface have a longer path length in the target than X-rays emitted at an angle closer to the surface normal and thus are attenuated more. This effect becomes more pronounced at very small take-off angles resulting in the characteristic heel profile. It also increases as the target ages because of deformation of the target surface due to thermal cycling and the emergence of microcracks allowing electrons to penetrate deeper. Looking at figure 2.9(a) it can be seen that this effect is stronger in-plane (top to bottom) than out-of-plane (left to right). Comparing the influence of relativistic effects and heel effect shows that the heel effect has a much stronger influence on the angular distribution of the total intensity.

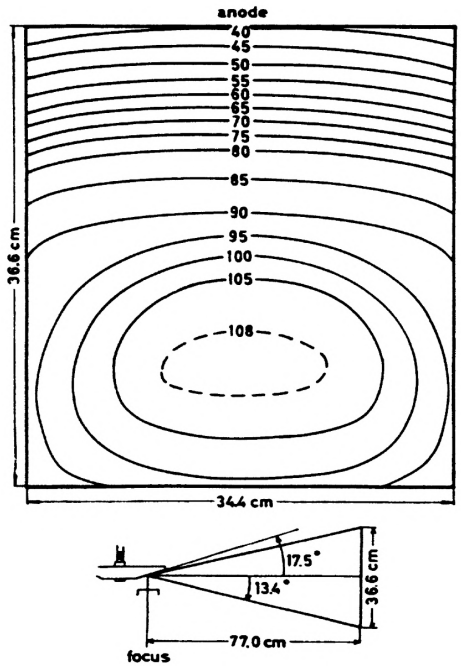

(a) Measurement of the heel effect. Intensity is measured in terms of air kerma [30].

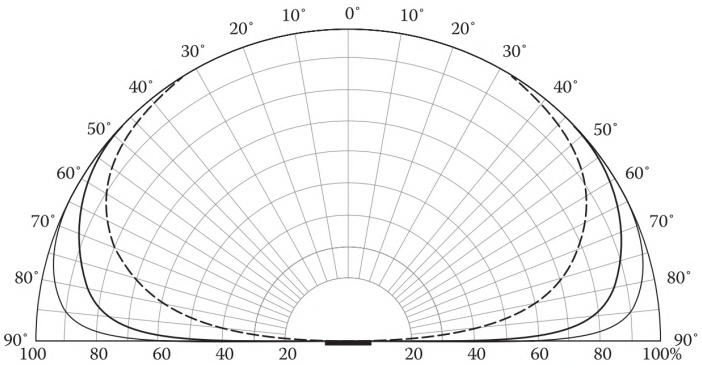

(b) X-ray intensity distribution showing the heel effect. The solid lines are from measurements with 70 kV tube voltage and two different filters. The dashed line is from a 10 kV tube voltage measurement [24].

Figure 2.9: Heel effect.

2.1.2. X-ray interaction with matter

As mentioned in the beginning of this chapter X-ray images are created by projecting a beam onto an object and detecting the X-rays that are transmitted. The contrast in the image is a result of some parts of the object attenuating the beam more than others. The attenuation is due to the X-rays interacting with the atoms in the medium its moving through. As photons and thus X-rays are neutral particles they move in straight lines until they have an interaction. These interactions are stochastic in nature and therefore the travel distance between interactions can only be described in terms of average or expected length such as the mean free path. There are different types of interaction, the most important being absorption, scattering and pair production. The attenuation of X-rays in a medium can be described by using the Lambert-Beer law [31]. Let us take the most simple example: a monoenergetic pencil beam incident on a homogeneous slab. In ideal circumstances the attenuation of the beam in the slab can be described by

$$I(x) = I_0 e^{-\mu x} \tag{2.4}$$

Here $I(x)$ is the intensity of the beam transmitted through the slab with thickness x without having undergone any interaction, I_0 the intensity of the incident beam and μ the linear attenuation coefficient which for X- or gamma rays is usually measured in cm^{-1}. For very small path lengths μ can be viewed as the probability that a photon undergoes an interaction along that path. It is inversely proportional to the mean free path: $\mu = l^{-1}$. Although equation 2.4 is nice in its simplicity, it does not tell the whole story. First of all, μ is not only dependent on the material, but also on the energy E of the incoming radiation. Secondly, apart from the material itself μ is also dependent on the density of the material. It is easy to imagine that water is better at stopping X-rays in liquid form than in gaseous form. It is therefore more convenient to use the mass attenuation coefficient μ_ρ instead. It is defined as $\mu_\rho = \frac{\mu}{\rho}$, units $cm^2 \cdot g^{-1}$ and is independent of the material density. This coefficient is plotted for various elements in figure 2.12(a). It can be seen that μ_ρ decreases exponentially with increasing energy. As a result X-rays with a lower energy are attenuated harder than high-energy X-rays. This causes a phenomenon called beam hardening to occur in a polyenergetic X-ray beam and is shown in figure 2.10. As filtration increases the total intensity of the beam decreases but the relative contribution of the high-energy X-rays increases and the mean energy of the spectrum shifts towards higher energies. By explicitly showing the dependence on energy and density equation 2.4 becomes

$$I(x,E) = I_0(E) e^{-\mu_\rho(E)\rho x} \tag{2.5}$$

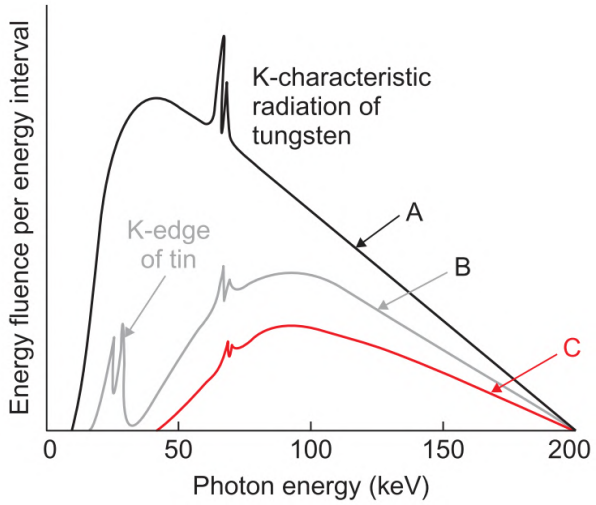

Figure 2.10: Beam hardening of an X-ray spectrum due to increasing filtration [26]. Curve A is filtered by aluminium, B by tin and aluminium and C by copper, tin and aluminium.

Finally, equation 2.5 does not take into account that X-rays that are scattered instead of absorbed can still reach the detector. For narrow beams this additional contribution to the intensity is fairly small, but for broad beams and thick, high density slabs it can be quite considerable. A way to correct for this is to use the buildup factor B. Tabulated values for different materials and geometries exist, but unfortunately in practice the buildup factor has to be determined experimentally or calculated using radiation transport theory. This is because it is strongly dependent on the geometry and composition of the system and the tabulated values can therefore not be generalized in most cases. Taking this into account equation 2.5 can be rewritten into

$$I(x,E) = B(x,E)\,I_0(E)\,e^{-\mu_\rho(E)\rho x} \tag{2.6}$$

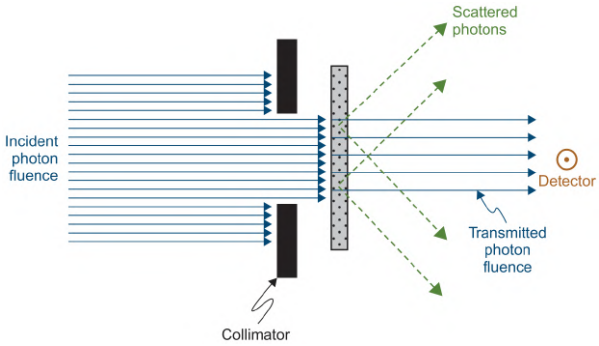

Figure 2.11: Diagram illustrating an experiment using X-rays [26]. A collimator is used to turn the broad beam into a pencil beam. Part of the beam is absorbed or scattered while the remainder is transmitted and reaches the detector.

Additionally, a collimator or an anti-scatter grid can be placed in front of the detector to filter out scattered radiation and limit the effect of scattering. Figure 2.11 shows a diagram of an experiment using a pencil beam. Equation 2.6 can be used to calculate attenuation of monoenergetic X-rays, but as described in section 2.1.1 the X-rays produced by an X-ray tube are polyenergetic. Equation 2.6 is no longer valid as it does not take into account the spectral distribution of the X-rays. At this point it is useful to discard the abstract quantity I and introduce two more concrete quantities: the photon fluence Φ and energy fluence Ψ. The photon fluence is defined as the number of photons dN incident on a sphere of cross-sectional area dA: $\Phi = \frac{dN}{dA}$, usually expressed in cm^{-2}. The energy fluence is related to the photon fluence as it is the radiant energy incident on a sphere of cross-sectional area dA and can be calculated from the photon fluence by using $\Psi = \Phi E$ with Φ

the fluence of photons with energy E. The unit of energy fluence is usually either J·m^{-2} or eV·cm^{-2} depending on the context. For use with polyenergetic photons they can be replaced by their differential counterparts:

$$\Phi_E(E) = \frac{d\Phi(E)}{dE} \quad \text{and} \quad \Psi_E(E) = \frac{d\Psi(E)}{dE} = \frac{d\Phi(E)}{dE} \cdot E \tag{2.7}$$

These are called the photon fluence differential in energy/photon fluence spectrum and the energy fluence differential in energy/energy fluence spectrum. $\Phi_E(E)$ could for example be one of the spectra shown in figure 2.6. These quantities can then be used in combination with the integral version of the Lambert-Beer law to calculate the total photon fluence or energy fluence transmitted through piece of material. One last adjustment that has to be made is that until now it has been assumed that the density of the object is homogeneous. More often than not this is not true and variations in density have to be accounted for by integrating over the path length. Implementing these final changes gives the following equations:

$$\Phi(x) = \int \Phi_{E,0}(E) e^{-\int_0^x \mu_\rho(E)\rho(x')dx'} dE \tag{2.8}$$

$$\Psi(x) = \int \Psi_{E,0}(E) e^{-\int_0^x \mu_\rho(E)\rho(x')dx'} dE \tag{2.9}$$

The buildup factor has been omitted from these equations for simplicity. As mentioned earlier, there are multiple types of interaction between X-rays and matter. Until now all these interactions have been combined into one attenuation coefficient, either linear or mass. A better fitting name would be the total linear/mass attenuation coefficient. Although this name is occasionally used in literature it can be safely assumed that if the attenuation coefficient is discussed without specifying its nature it is the total attenuation coefficient. The most important interactions are absorption due to the photoelectric effect, coherent scattering, incoherent scattering and to a certain degree pair production, although this last one is only relevant for therapeutic X-ray treatment. The total mass attenuation coefficient can thus be split into the following coefficients:

$$\mu_{\rho,tot} = \mu_{\rho,pe} + \mu_{\rho,coh} + \mu_{\rho,inc} + \mu_{\rho,pp} \tag{2.10}$$

For carbon, iron and lead these coefficients are plotted in figures 2.12(b), 2.12(c) and 2.12(d) while their total attenuation coefficients are compared in 2.12(a). It should be noted that the pair production coefficients do not appear in these plots. Their absence will be explained later.

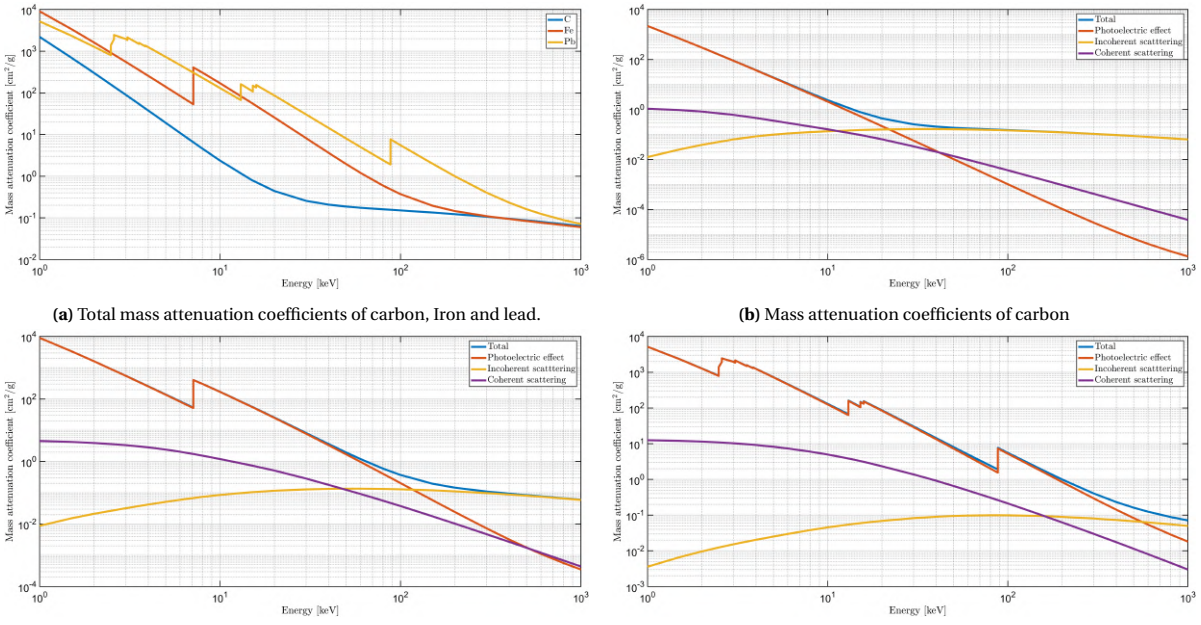

(a) Total mass attenuation coefficients of carbon, Iron and lead.

(b) Mass attenuation coefficients of carbon

(c) Mass attenuation coefficients of iron

(d) Mass attenuation coefficients of lead

Figure 2.12: Mass attenuation coefficients. Data retrieved from the XCOM database [32] which is run by the National Institute of Standards and Technology (NIST).

Photoelectric effect

In the photoelectric effect a photon interacts with the entire atom, resulting in the photon being absorbed and an electron being emitted, often called photoelectrons. The entire energy of the photon is absorbed by the atom, after which almost all of it is transferred to an electron which is ejected as a result with an kinetic energy equal to the photon energy minus the binding energy of the electron. In theory due to the laws of conservation of momentum the residual atom has to retain some of the photon energy, but as the mass of the atom is approximately four orders of magnitude larger than that of the electron this can be neglected. Similarly to the ionization of atoms due to electron-electron interactions explained in section 2.1.1 the ejection of a photoelectron is followed by an outer-orbital electron falling down and the emission of a characteristic X-ray or Auger electron.

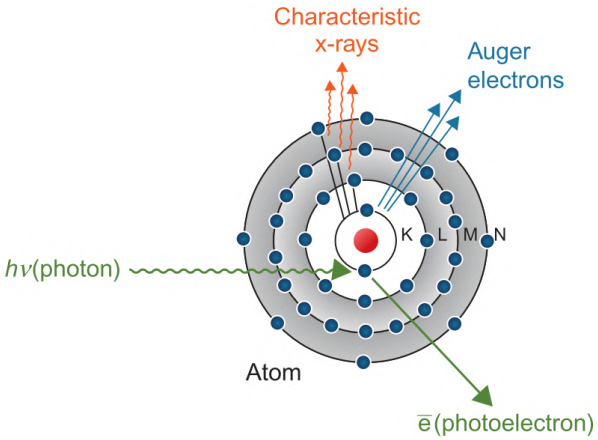

Figure 2.13: Illustration of the photoelectric effect. [26]. A photon with an energy larger than the K-shell binding energy is absorbed by an atom and a photoelectron is ejected. Following this an outer-shell electron falls down to fill the vacancy and either a characteristic X-ray or an Auger electron is emitted.

The probability of a photon being absorbed is dependent on both its energy and the material it is traveling through. The mass photoelectric coefficient $\mu_{\rho,pe}$ is plotted in figures 2.12(b), 2.12(c) and 2.12(d). Starting at low energy, as the energy increases $\mu_{\rho,pe}$ decreases. For carbon $\mu_{\rho,pe}$ is seen to be decreasing monotonically, but for iron and lead in particular discontinuous jumps can be seen at certain energies. These are called absorption edges and are related to the binding energies of the electron shells. These jumps can be understood as resonance effects between the incoming X-ray and the electrons in the shells. Just below an absorption edge an X-ray does not have enough energy to eject an electron from the corresponding shell and only electrons from higher shells are available. As the energy increases to equal that of the absorption edge resonance occurs and an additional shell becomes available for photoelectric absorption, resulting in a jump in $\mu_{\rho,pe}$. After this, $\mu_{\rho,pe}$ decreases again with increasing energy until the next absorption edge is crossed, continuing until finally the energy is higher than the K-shell edge after which it also decreases monotonically. For elements with atomic number Z ≤ 10 there are no absorption edges above 1 keV, which is why no jump can be seen for carbon. Besides energy $\mu_{\rho,pe}$ is also strongly dependent on the atomic number of the absorbing material. It can be shown that it adheres to the following relationship:

$$\mu_{\rho,pe} \propto Z^n \tag{2.11}$$

where n varies between 3 and 5 depending on the energy. This dependence allows images to be made even if the materials in the object are similar in density and amplifies the contrast in other cases.

Coherent scattering

Coherent scattered X-rays are scattered without losing energy and continue with only their direction changed. It can be understood by viewing photons as waves rather than particles. Coherent scattering can subdivided into two types of scattering: Thomson scattering and Rayleigh scattering. In Thomson scattering the incoming photon interacts with a single loosely bound electron which can be considered free, meaning the photon energy is much higher than the binding energy. The incoming electromagnetic wave causes the electron to start oscillating and emitting dipole radiation with the same frequency as the incident wave. The X-ray frequency is larger than the resonance frequency of the electron which therefore radiates in antiphase with

the incoming wave. This type is named after J.J. Thomson who first explained it using classical physics and calculated the famous Thomson differential cross section (DCS:

$$\frac{d\sigma_{Th}}{d\Omega} = \frac{r_e^2}{2}(1+\cos^2\theta) \tag{2.12}$$

where r_e is the classical electron radius and θ the scattering angle. The second type of coherent scattering is Rayleigh scattering. Contrary to Thomson scattering, Rayleigh scattering describes interaction of photons not with a single, loosely bound electron but with the collective of tightly bound electrons and as such with the atom as a whole. This form of scattering is not completely coherent as the atom absorbs a fraction of the photon energy, but again due to its heavy mass and conservation of momentum this fraction is negligible. As the scattering is of the atom as a whole the charge distribution of all electrons has to be taken into account. This is done by modifying the Thomson DCS with the atomic form factor $F(q,Z)$, dependent on the momentum transfer to the atom q and the atomic number of the atom Z. For unpolarized photons the resulting Rayleigh DCS is given by

$$\frac{d\sigma_{Ra}}{d\Omega} = \frac{r_e^2}{2}(1+\cos^2\theta)[F(q,Z)]^2 = \frac{d\sigma_{Th}}{d\Omega}[F(q,Z)]^2 \tag{2.13}$$

Values for the form factors have been calculated and tabulated in the past, for example by Hubbell et al. [33]. This model of coherent scattering is called the form-factor (FF) approximation and is the most widely used one in photon transport simulation [34]. The coherent mass attenuation coefficient can be calculated by integrating $\frac{d\sigma_{Ra}}{d\Omega}$ over the full solid angle and multiplying it with the atom density.

Incoherent scattering

Incoherent scattering for X-rays is dominated by the Compton effect. Similar to Thomson scattering, in the Compton effect a photon interacts with a (nearly) free electron. This time, however, the scattered photon has lost energy which is transferred to the electron it interacted with. This effect is depicted in figure 2.14. Observed by A.H. Compton, after which the effect is named, the effect showed that light can not be viewed as just waves, but also shows particle-like behaviour. The amount of energy absorbed by the electron depends on the angle the photon is scattered with, while according to classical electrodynamics the energy of the scattered X-rays should be the same as that of the incoming X-rays. Compton derived an equation relating the energy of the scattered X-ray to the scattering angle:

$$E' = \frac{E}{1+(E/m_ec^2)(1-\cos\theta)} \tag{2.14}$$

Here E is the energy of the incoming X-ray, E' the energy of the scattered X-ray, m_ec^2 the electron rest mass and θ the scattering angle. For unpolarized X-rays the differential cross section is given by

$$\frac{d\sigma_{KN}}{d\Omega} = \frac{r_e^2}{2}\left(\frac{E'}{E}\right)^2\left(\frac{E'}{E}+\frac{E}{E'}-\sin^2\theta\right) \tag{2.15}$$

This differential cross section, one of the first results of quantum electrodynamics, was derived by Oskar Klein and Yoshio Nishina and subsequently named after them. In the limit of low photon energy E' becomes almost equal to E and the Klein-Nishina (KN) DCS reduces to the Thomson DCS. It turns out that Thomson scattering is just the classical form of Compton scattering. The KN cross section is based on the assumption that the electron that is interacted with is at rest and free. This is valid for X-rays with an energy much higher than the binding energy, but as the energy of the X-ray becomes more comparable to the binding energy this method breaks down. In order to take into account the effect of binding energies the KN cross section has to be corrected. Similar to the Rayleigh DCS this is done using a correction factor $S(q,Z)$, called the incoherent scattering function. After correction of equation 2.15 the Compton DCS is described as

$$\frac{d\sigma_{Co}}{d\Omega} = \frac{r_e^2}{2}\left(\frac{E'}{E}\right)^2\left(\frac{E'}{E}+\frac{E}{E'}-\sin^2\theta\right)S(q,Z) = \frac{d\sigma_{KN}}{d\Omega}S(q,Z) \tag{2.16}$$

Values for $S(q,Z)$ have also been calculated by Hubbell et al. [33]. Similarly to the FF approximation this model is called the incoherent scattering function (ISF) approximation. Because the Compton effect primarily involves free electrons at high energy it only depends weakly on the atomic number Z of the material and depends mainly on the electron density (electrons per gram). Although electron density decreases with increasing Z, this decrease is very slow and with the exception of hydrogen electron densities of all elements are

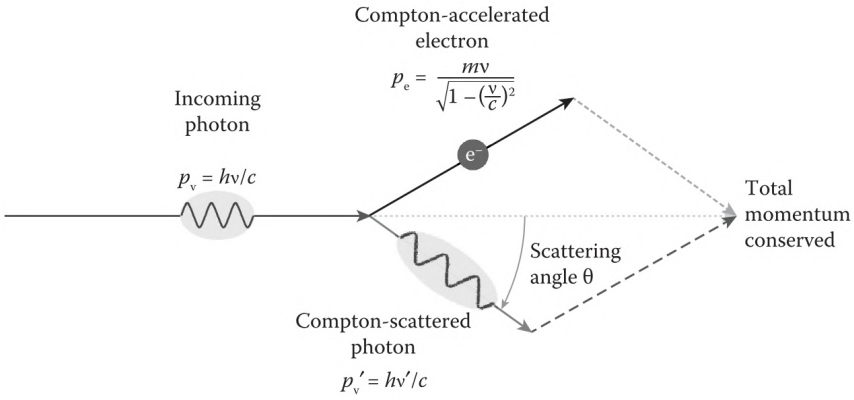

Figure 2.14: Illustration of the Compton effect. [24]. A photon interacts with a loosely bound electron, scattering at an angle θ, emerging with a reduced energy.

very close to each other, ranging from $3.01 \cdot 10^{23}$ for carbon to $2.38 \cdot 10^{23}$ for lead [26]. Consequently, $\mu_{\rho,inc}$ is approximately the same for all elements at high energy. Looking at figures 2.12(b), 2.12(c) and 2.12(d) it can indeed be seen that the values for $\mu_{\rho,inc}$ are very similar for all three elements.

Pair production
Pair production is the production of an electron and positron pair due to a photon interacting with the strong electromagnetic field of the nucleus of an atom. In this process loses all its energy and ceases to exist. Both the electron and the positron have a rest mass of roughly 511 keV, which means that because of conservation of energy the photon needs at least an energy of 1022 keV for this process to be possible. Any remaining energy is divided between the particles. Because of this threshold energy $\mu_{\rho,pp}$ is not visible in figures 2.12(b), 2.12(c) or 2.12(d). Pair production is also not relevant for diagnostic imaging as the maximum energy used is around 150 keV, making it impossible.

2.1.3. X-ray detection

There are many different types of radiation detectors. Some are specialized for detecting a specific kind of radiation, while others are more general in use. One of the more famous detectors is the Geiger-Muller tube, better known as the Geiger Counter. It is a widely used detector and is often shown in media where its characteristic ticking noise is an easy tool to create tense situations. In general radiation detectors can be divided into two types of detectors: ionisation detectors and scintillation detectors. They can then be further classified as either gaseous, liquid or solid state detectors. Needless to say the working principle behind ionisation detectors is the creation of ion and electron pairs by ionizing radiation. In ionization detectors the target for these ionisations has a positive electrode on one side and a negative on the other. The resulting electric field causes the ion to migrate towards the negatively charged electrode and the electron to the positive one. As a result a pulse of electric current is measured which is proportional to the number of electron-ion pairs. The number of pairs itself is proportional to the energy deposited by the incoming radiation. By increasing the voltage between the electrodes the primary electrons gain enough energy to cause secondary ionisations on their own as they are accelerated towards the positive electrode. This results in many more electron-ion pairs moving to the electrodes and therefore a higher pulse. As longs as the voltage is not too high the measured pulse is still proportional to the deposited energy. If the voltage is even higher than so many secondary ions are formed that their charge can locally cancel the electric field. This prohibits new secondary ionisations and thus no pulse can be measured. As a result all interactions at these high voltages lead to the same pulse which has a large amplitude and is easy to measure, but does not result in information about the energy of the measured radiation. The Geiger Counter is an example of such a detector.

Scintillation detectors are also (partially) dependent on the ionising capabilities of the incoming radiation, but use a different mechanism for detection. The radiation either excites or ionises molecules in the target material. After a certain period the molecules fall back to their ground state, emitting a photon. This process is similar to the one describing the production of characteristic X-rays in section 2.1.1, although scintillation photons are usually of much lower energy, roughly between 1 to 10 eV. To produce a measurable signal these photons have to be converted to an electrical pulse. In order to do so they are guided towards a light

detector. One such a detector is a photomultiplier tube (PMT). Here scintillation photons are absorbed in the photoelectric effect, ejecting an electron. These electrons then strike multiple electrodes in succession, freeing more electrons at each electrode. The resulting electron avalanche amplifies the current produced by the incoming light by multiple orders of magnitude which results in an easily measurable electrical pulse. As the number of scintillation photons produced and thus the number of electrons freed in the PMT is proportional to the energy deposited by the radiation spectral measurement is also theoretically possible using scintillation detectors. Besides PMTs scintillation photons can be converted to an electrical signal using photodiodes. Again the scintillation photons are converted to electrons by the photoelectric effect, producing a photocurrent. Both PMTs and photodiodes have advantages and disadvantages and which one is preferable depends on the circumstances.

For many years since the discovery of X-rays photographic film or phosphorescent screens have been used for diagnostic imaging. An example of such an image is figure 2.1. Imaging using film was a state-of-the-art technique for many years, but had a major disadvantage: the film was very thin and low in mass which reduced its sensitivity to X-rays, necessitating long exposure times. This problem was mitigated by placing scintillating screens on both side of the film, exposing it to visible light produced by the screens. These screens were much better at absorbing X-rays so the exposure time could me reduced. However, ever since digital equipment has become widely available for X-ray imaging film is rarely being used anymore. Modern medical imaging now mostly uses flat panel detectors.

Flat-panel detectors (FPDs) are relatively large and thin detectors resembling television or computers screens. Like these screens they are made up of a very large number of pixels, but for FPDs these pixels are actually individual radiation detectors. Both ionisation (direct) or scintillation (indirect) detectors can be used, but they are always solid state. In both cases the resulting electrical signal is read out using a MOSFET, usually a TFT or a CMOS. One advantage direct detectors have over indirect detectors is that in general their images suffer from less blur. The reason for this is that in indirect detectors the scintillation photons are emitted in all directions. As a result photons can end up in a light detector that is not in line with the incoming radiation particle. This phenomenon where a photon ends up in the wrong detector is called crosstalk. In the direct detector the created electron-hole pair is accelerated by an electric field perpendicular to the pixel array, limiting electron drift in this plane. This effect is illustrated in figure 2.15. Due to the isotropic emission of scintillation photons the line spread function of the indirect detector is more spread out compared to that of the direct detector with lower spatial resolution as a result.

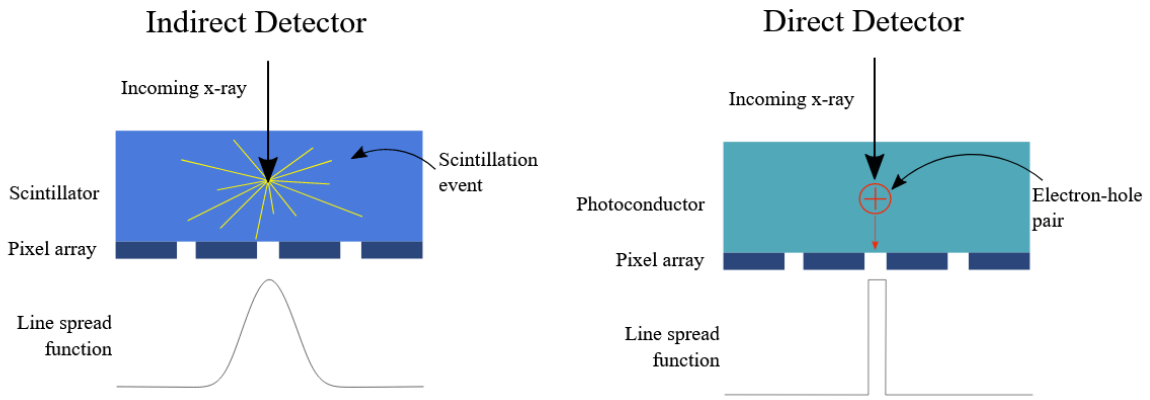

(a) Schematic illustration of an indirect flat panel detector.

(b) Schematic illustration of a direct flat panel detector.

Figure 2.15: Light spreading in the scintillator material leads to loss of resolution in indirect detectors which direct detectors do not experience [35].

In order to reduce crosstalk modern flat panel detectors do not use a single large scintillator in front of the pixel array but many small column-like scintillators parallel next to each other, one for each pixel. These columns act as optical fiber cables, making it harder for a scintillation photon to crossover into a different column and thus to be detected in the wrong pixel. While it is possible to design a FPD that can count individual X-rays and measure their energy this information is in most cases not relevant for imaging purposes. They are therefore generally charge-integrating; the charge generated by the incoming X-rays is collected and the total charge is read out after a certain period. The output is a quantity dependent on the

collected charge, often expressed in analog-to-digital units (ADU). Compared to particle-counting pixel detectors charge-integrating pixel detectors have generally better spatial resolution and a zero dead time [36]. On the other hand they suffer from dark current and other forms of noise and have a limited dynamic range. Generally charge-integrating detectors are preferred for measurements with high radiation intensity which is often true when X-rays tubes are used.

2.2. Supercritical fluids

In day-to-day life, one observes matter in one of its four fundamental states: gas, liquid, solid or plasma. Besides these states that can be observed under normal conditions there are many (intermediate) states that require more extreme conditions. An example of such a state are supercritical (SC) fluids. Supercritical fluids are substances that have been brought above their critical point. This can be contextualized by looking at figure 2.16, which shows the phase diagram of a certain substance. Here the areas where the substance exists as a single phase and the triple point were these phases are in equilibrium are indicated. If the liquid-gas equilibrium curve is followed at a certain pressure and temperature the critical point is reached. The temperature and pressure at this point are referred to as the critical temperature T_c and critical pressure P_c. At this point the densities of the gas and liquid phase become equal and the substance can now no longer be described as either a gas or a liquid. It is instead referred to as a supercritical fluid provided both its temperature and pressure are higher than T_c and P_c. The hatched area in figure 2.16 represents the supercritical region.

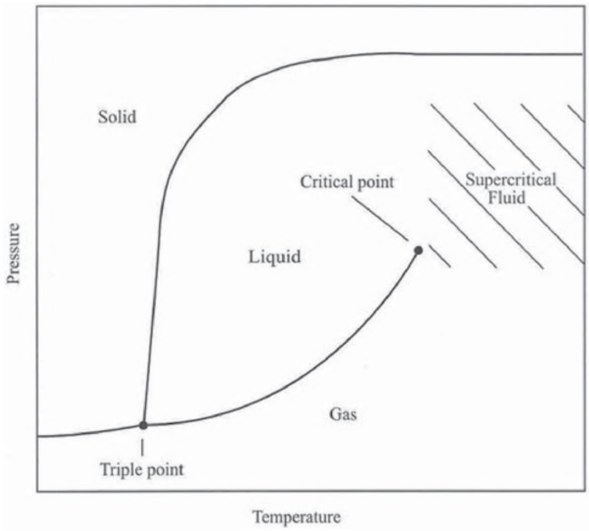

Figure 2.16: Generalized phase diagram of a substance [37]. The pressure axis is non-linear with the solid state at high temperatures occurring at very high pressures.

Supercritical fluids are interesting because they can have properties that are intermediate between those of liquids and gases. Compared to gases they have for example a superior ability to dissolve other substances and are more like liquids in that regard. Comparing them to liquids they show lower densities and viscosities, while their diffusivity is much greater, allowing them to effuse through porous materials like a gas. Furthermore these properties can be altered by either changing the pressure or temperature. Compared to a liquid this gives an extra degree of freedom allowing more than one property to be optimized. Although in the supercritical region there are no distinct sub-phases it is still possible to make some distinction between the fluid in different conditions. At the bottom of the hatched area the SC fluid is more gas-like. As pressure increases the fluid becomes more and more liquid-like. This change is continuous and no phase transition can be directly observed to distinguish the gas-like state from the liquid-like state. It is however possible to make a distinction based on other properties. In the supercritical phase many properties such as the thermal expansion coefficient and the constant-pressure heat capacity show maxima at certain temperature-pressure conditions. An example of this can be seen in figure 2.17 where the isobaric specific heat of R23 is shown at 5.5 MPa. If one would plot the locations of these maxima for various pressures in the phase diagram a line would form emanating from the critical point. This can be seen in figure 2.18 showing the phase diagram of water. If the line shows the locus of isobaric heat capacity maxima it is referred to as the Widom line. Above

this line the fluid is liquid-like, while below it is gas-like, but this was not proven until 2010 by Simeoni et al. [38], using incoherent X-ray scattering and molecular dynamics simulations.

While the Widom line can be seen as the supercritical version of the coexistence line in subcritical conditions there are some major differences. In subcritical conditions the liquid and gas phases can only be mixed during the boiling process taking place along the coexistence line and are strictly separated when the system has returned to equilibrium. In contrast Ha et al. [39] showed that in a supercritical fluid both gas-like and liquid-like particles coexist as an inhomogeneous mixture, forming distinct microstates. The region in which this phenomenon occurs extends from the critical point and encloses the Widom line and is named the Widom delta due to its shape. The transition from liquid-like to gas-like then corresponds to the number fraction of these microstates changing with them being even at the Widom line. An example of this delta can be seen in figure 2.19. Here it can also be seen how the gas-like particle fraction changes as the fluid goes from one state to the other. Furthermore, Banuti [40] explains the transition from the liquid-like state to the gas-like state using the pseudo-boiling concept. Pseudo-boiling is a supercritical analog to 'normal' boiling at subcritical conditions, however this transition does not take place at phase equilibrium but over a finite temperature interval. It is currently accepted that gas-like and liquid-like supercritical fluids are two separate phases that can be distinguished at molecular level, but no experimental evidence has yet been provided that shows that these states are distinguishable at mm scale [20].

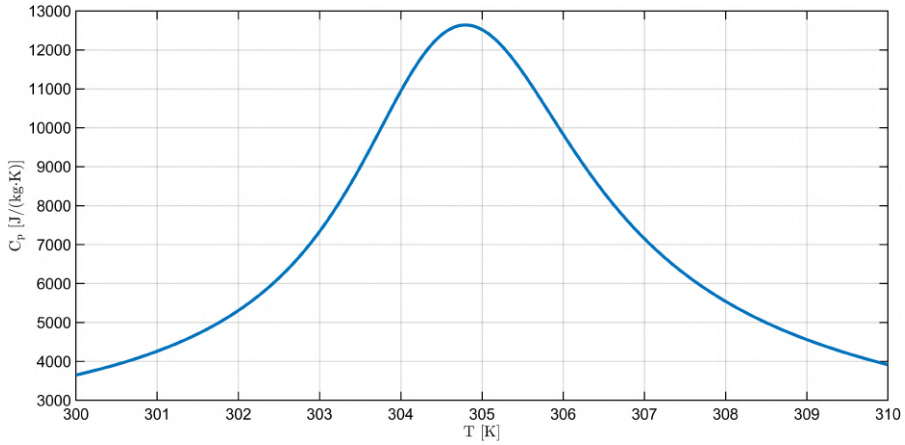

Figure 2.17: Isobaric heat capacity of R23 at 5.5 MPa. Values retrieved from the CoolProp database [14].

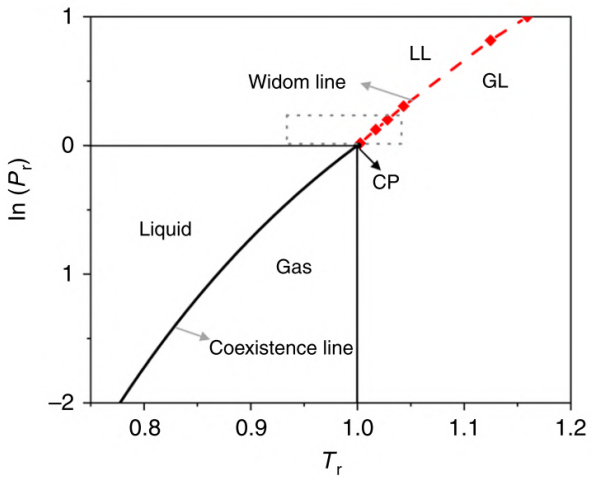

Figure 2.18: Phase diagram of water [20]. Below the critical point the coexistence line separates liquid from gas, while above the Widom line separates liquid-like from gas-like. The x- ans y-axis show the reduced temperature and pressure ($T_r = T/T_c$ and $P_r = P/P_c$.

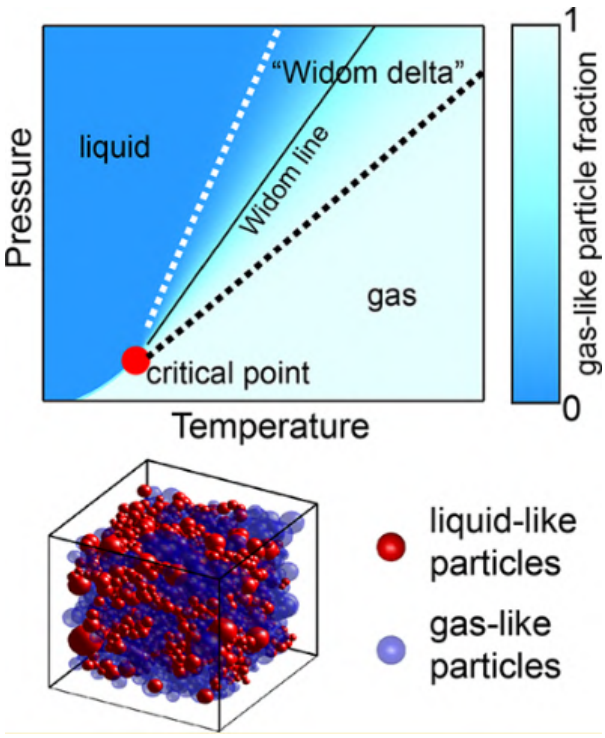

Figure 2.19: Widom delta in a PT phase diagram [39]. The colour scale indicates the fraction of gas-like particles.

3

Experimental approach

In this chapter the experimental setup will be detailed, which includes the RB cell and the X-ray facility that was to be used for the projectional radiography. Furthermore the measurements that were done before the lockdown described along with a quick overview of the planned measurements. Finally an attempt to do some additional measurements using a radioactive source is discussed.

3.1. Experimental setup

3.1.1. Rayleigh-Bénard cell

In order to study Rayleigh-Bénard convection in a supercritical fluid using PIV measurements a specialized setup was designed by Valori et al. [16]. This setup can be seen in figure 3.1(b). In this section a brief description will be given of this setup along with some relevant information. For a more detailed description and design criteria see chapter 4 of Valori [41]. The internal part of the cell can be seen in figure 3.1(a) and is composed of two horizontal copper plates and two vertical glass walls. In each copper plate a conduct for water is present. These conducts provide heat exchange to the cell and allow the user to change the temperature of the top and bottom copper plate. The minimum achievable temperature is 20 °C and the maximum 70 °C. The glass trapezoid in contact with one of the vertical walls is a light guide used to guide the laser sheet into the cell during PIV measurements. The internal dimension of this cube is 70 mm.

As mentioned in section 1.2 the critical pressure of R-23 is 4.8 MPa. The cell therefore needs to be able to withstand high pressures. To accomplish this the cell is inserted into a high-pressure facility as shown in figure 3.1(b). This facility is composed of a stainless-steel cylinder with three flanges. The flanges have a center made of a special borosilicate glass for high-pressure applications and allow optical access to the fluid. The smaller flange is connected to the light guide as an access port for the laser. The two larger flanges are connected to the sides of the cylinder and allow the camera to capture the fluid flow. These flanges have a thickness of 32 mm and an internal diameter of 80 mm. When properly assembled the facility has a working pressure up to 7 MPa, considerably higher than the critical pressure of R-23. A pipe allows R-23 to be fed into the cell and to be removed and recaptured after the experiment is finished.

3.1.2. X-ray facility

The X-ray scanner facility is located in the basement of the 'North' wing of the Reactor Institute Delft (RID) where it is shielded by thick concrete walls. A sketch is shown in figure 3.2(a). It consists of three identical X-ray tube-detector pairs angled at 120° with respect to each other. Both the tubes and detectors are attached to a hexagonal support structure. In the middle of the structure a lifting table is located. The table can be used to change the vertical position of the object that is studied to align it with the center of the detectors/tubes. A top view of an object, in this case a fluidized bed, being studied can be seen in figure 3.2(b). It should be noted that this image is based on a older configuration of the setup using much simpler detectors.

The X-ray tubes used in the facility are Y.TU 160-D06 end grounded metal-ceramic X-ray tubes, manufactured by YXLON. These tubes have a maximum tube voltage of 160 kV, although they are limited to 150 kV for historical reasons. The focal spot size of the electron beam striking the tungsten target can be set to either 0.4

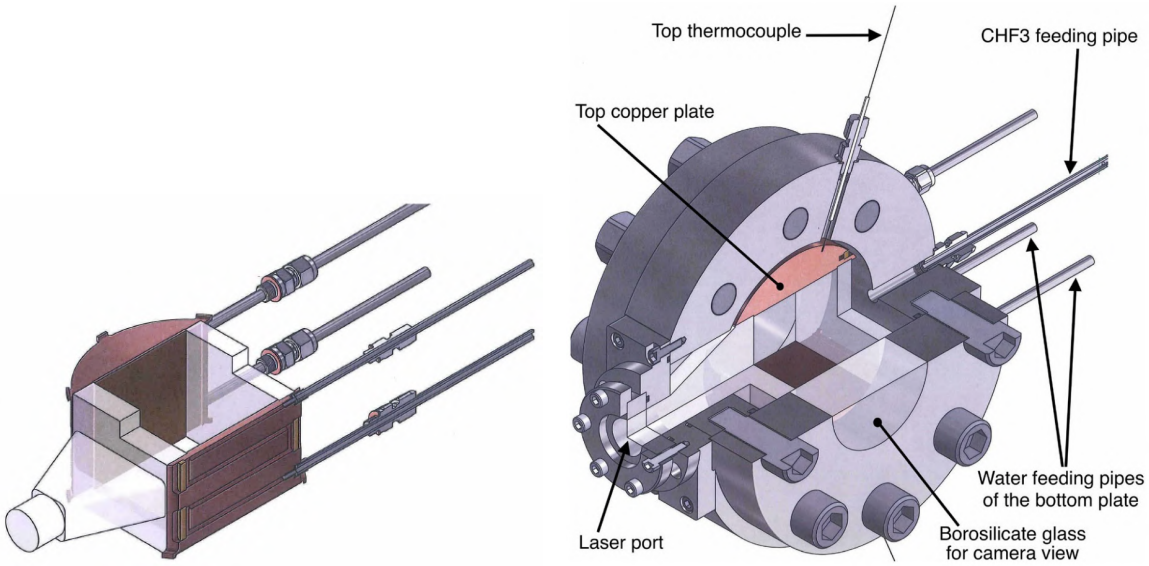

(a) Internal part of the Rayleigh-Bénard cell [16].

(b) Drawing of the Rayleigh–Bénard high-pressure convection cell [41].

Figure 3.1: External view and internal view of the RB cell.

or 1.0 mm. The maximum allowed power is lower for the smaller focal spot size due to the heat generation in the target being more localized. For 0.4 mm the maximum power is 0.8 kW, restricting the maximum tube current at 160 kV to 5 mA. With a 1.0 mm focal spot the maximum power is 1.8 kW which corresponds to a current of 12 mA at 150 kV. Lowering the tube voltage allows a higher tube current to be used. The target itself is angled at 11°. The aperture of the tubes causes the X-rays to be emitted in a cone with a horizontal angle of 40°and a vertical angle of 30°. Furthermore the tubes have an inherent filtration to remove unwanted low-energy X-rays. This filter consists of 0.8 mm Be and 3.0 mm Al.

The detectors used for imaging are Xineos-3131 CMOS X-ray flat panel detectors. These are scintillation detectors with caesium-iodide (CsI) as scintillator. Their pixel array consists of 1548 by 1524 pixels, each pixel having a surface area of 198 x 198 μm^2. The effective energy range is 40 to 120 keV. In normal operation it is possible to take images at a frequency of 30 Hz. The region of interest (ROI) can be decreased in one dimension to increase the frame rate to 200 Hz or higher. They have a 14 bit dynamic range, restricting the maximum output value to 16383. This limits the maximum radiation intensity level that can be discerned. All radiation intensity levels above this point will result in the same output signal. The X-ray tube settings should therefore be chosen such that the highest measured intensity lies below this level.

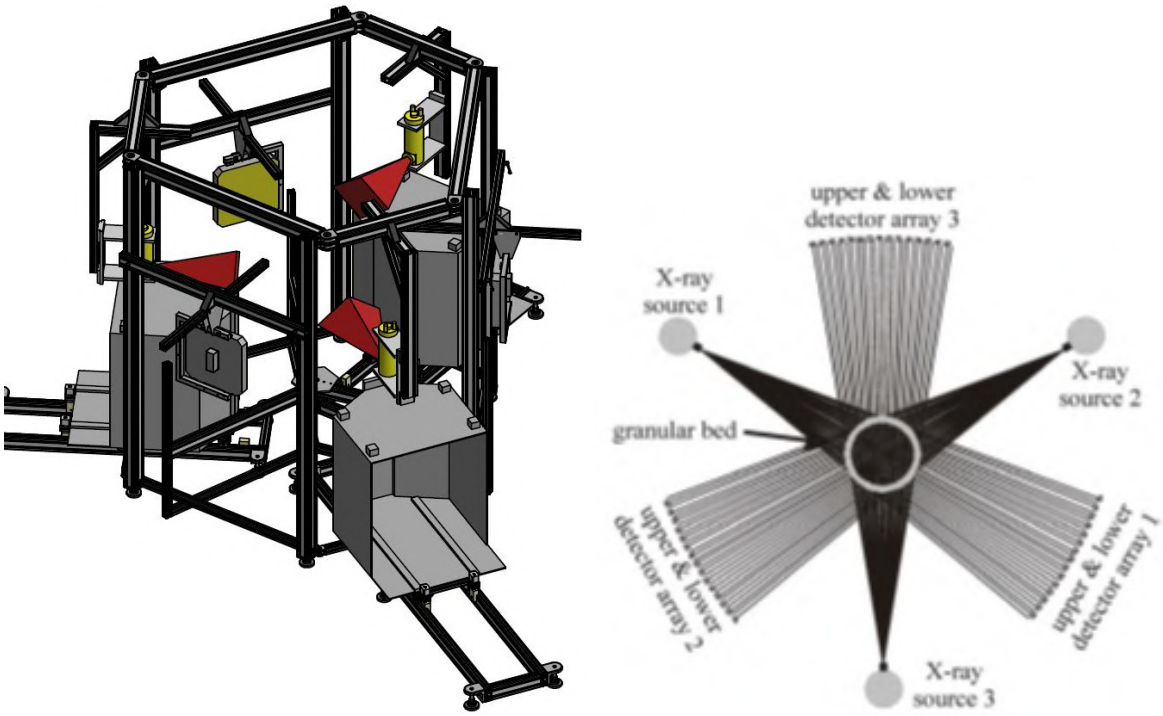

(a) View of the X-ray scanner setup, showing X-ray tubes and X-ray detectors [42].

(b) Top view of complete setup [43].

Figure 3.2: Sketch of the X-ray facility (left) and top view of an object being irradiated (right).

3.2. Measurements

As mentioned in the introduction Valori et al. [16] investigated the feasibility of using PIV in a supercritical fluid. To do so a flow resulting from Rayleigh-Bénard convection in a supercritical fluid (R-23) was studied. RB convection is a type of natural convection in which a fluid is heated from below. Three different experimental conditions were studied and were labeled SC_{liquid}, $SC_{max\Delta\rho}$ and SC_{gas}. These names were chosen due to SC_{liquid} being closer to the liquid phase of the SC fluid, $SC_{max\Delta\rho}$ having the largest difference in density between the top and bottom of the cell and SC_{gas} being closer to the gas phase. The experimental parameters for these experiments can be found in table 3.1 while figures 3.3(a) and 3.3(b) show the density and isobaric thermal expansion coefficient in these experiments as a function of temperature respectively. In all three cases the mean velocity field showed a large-scale circulation (LSC) roll which is a flow structure typical of RB convection. Comparing the velocities of this roll in the different conditions showed that the LSC velocity near the gas phase is smaller than near the liquid phase even though the Rayleigh and Prandtl numbers were approximately the same in these conditions. One explanation offered is that this is due to the temperature dependency of certain fluid properties that are part of the Rayleigh number, more specifically the ratio of the isobaric thermal expansion coefficient (α), the kinematic viscosity (ν) and the thermal diffusivity (κ): $\frac{\alpha}{\nu\kappa}$. Plotting this ratio as a function of temperature results in a line with approximately the same shape as α in figure 3.3(b). Near the liquid phase the ratio is larger at the bottom of the cell, possibly enhancing thermal convection. On the other hand near the gas phase the ratio is smaller at the bottom, reducing thermal convection.

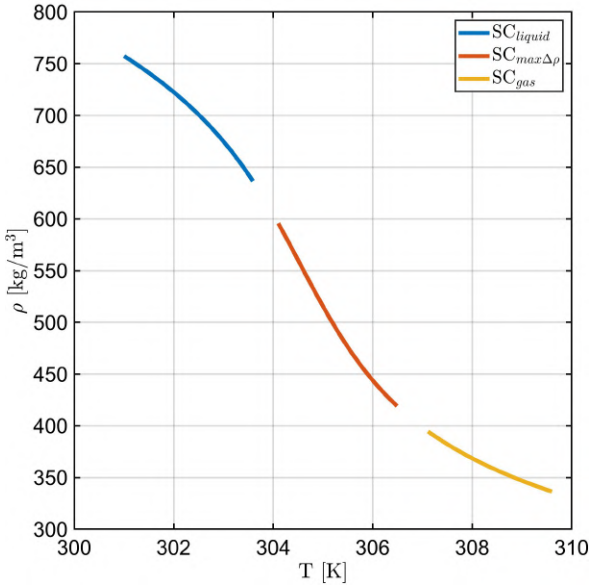

(a) Density of R-23 in the intervals studied by Valori [41].

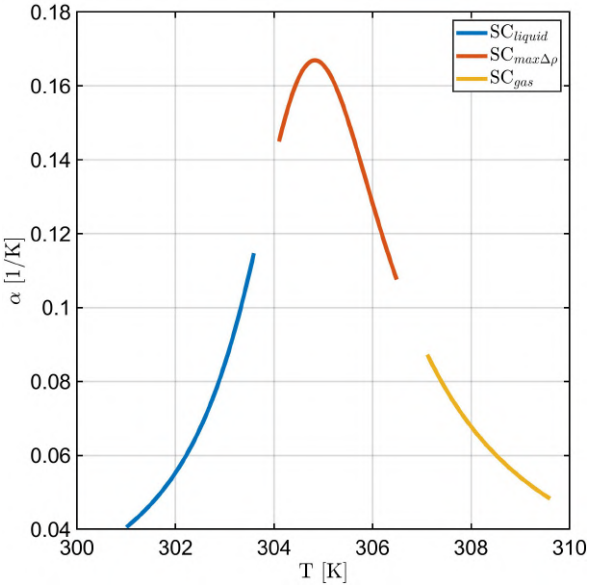

(b) Thermal expansion of R-23 in the intervals studied by Valori [41].

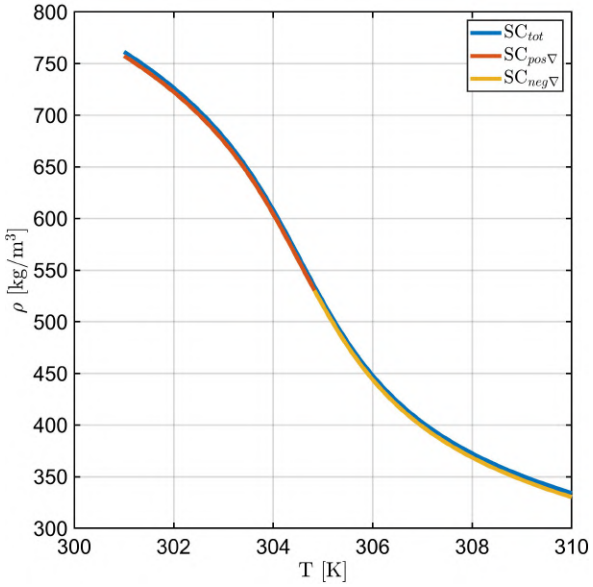

(c) Density of R-23 in the additional intervals

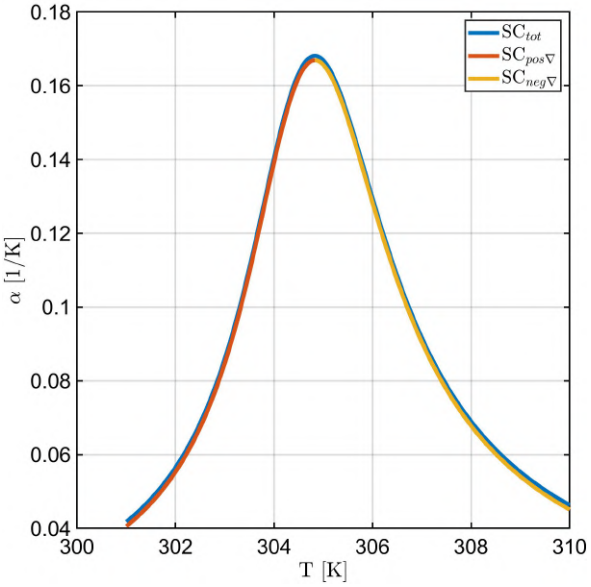

(d) Thermal expansion in the additional intervals.

Figure 3.3: Density and thermal expansion coefficient of R-23 in the intervals studied by Valori [41] and the additional proposed intervals. The values were retrieved from the CoolProp database [14].

Table 3.1: Data matrix of the experimental conditions studied by Valori [41], taken from their thesis. The subscript t and b refer to the top and bottom plate respectively and σ is the standard deviation of the measured quantities during the measurements.

	p [kPa]	**σ(p) [kPa]**	**T_t [K]**	**$\sigma(T_t)$ [K]**	**T_b [K]**	**$\sigma(T_b)$ [K]**	**ρ_t [kg/m^3]**	**ρ_b [kg/m^3]**
SC$_{liquid}$	5519	6.10	301.0	0.07	303.6	0.07	759.57	645.65
SC$_{max\Delta\rho}$	5516	4.25	304.1	0.08	306.5	0.08	608.91	426.72
SC$_{gas}$	5512	4.94	307.1	0.08	309.6	0.08	401.48	338.54

3.2.1. Projectional radiography

Although the X-ray facility can be used for computed tomography which allows the internal structure of objects to be visualized the geometry of the RB cell prohibits use of this technique. As this project would in spirit be a continuation of the research done by [16] it was self-evident to at minimum study the SC fluid in

the same experimental conditions. The time-averaged images were acquired by measuring over an one-hour period with a sampling frequency of 3 Hz which corresponds to 10800 images. As the X-ray tubes are actively cooled they can be turned on for an hour long period or even longer, but this does not necessarily mean X-ray measurements can be done over such a period. First of all, the measurement time is typically limited by the memory space on the computer. Each image taken is almost 5 Mb in size and at a 22 Hz sampling frequency this can quickly ad up. Furthermore, according to the ALARA principle the measuring time should be kept as short as possible meaning that if additional measuring time only results in marginally better results it should not be done.

Besides these experimental conditions the proposition was made to study additional conditions in order to cover parts not studied in the previous three. The subscripts of these conditions indicate the total region between 300 and 310 K, the region where the gradient of the thermal expansion coefficient is positive and the region where it is negative. The settings accessory to these conditions are shown in table 3.2 while the density and isobaric thermal expansion coefficient in these regions are shown in figures 3.3(c) and 3.3(d).

Table 3.2: Data matrix for the proposed additional experimental conditions to be studied. The values for ρ were taken from the CoolProp database [14]. The subscript t and b refer to the top and bottom plate respectively.

	p [kPa]	**T_t [K]**	**T_b [K]**	**ρ_t [kg/m^3]**	**ρ_b [kg/m^3]**
$SC_{pos\nabla}$	5515	301.0	304.8	757.4	533.0
$SC_{neg\nabla}$	5515	304.8	310.0	533.0	330.3
SC_{tot}	5515	301.0	310.0	757.4	330.3

In addition to studying R-23 in its supercritical state the project had a secondary objective: studying the feasibility of using projectional radiography/CT to study density structures in supercritical fluids in future projects. To do so the limit of current setup to produce images in which details could still be resolved should be investigated. Unfortunately, due to the X-ray facility being in high demand for other projects the available time for measurements would be limited and they would have to be done in quick succession over a short period. This meant that there would be no time for detailed data processing in between measurements, but it would however be possible to create a simple image to get an indication of the results. If these images gave the impression that density differences throughout the cell could be imaged at the studied conditions additional measurements could be done at smaller and smaller temperature difference between the top and bottom to see when this would no longer be true. For these measurements it would also be an option to reverse the temperature difference between the top and bottom plate, setting the temperature at the top to be higher. This would result in a steady state situation which might prove useful for studying the limit of resolving density differences.

Another option would be to rotate the cell so the X-ray beam would no longer be perpendicular to the front of the cell. As the flow structure in the cell is three-dimensional this might provide additional information. A drawback of rotating the cell is that more and more of the inside is shielded by the steel cage as the angle between beam and cell increases. This effect is illustrated in figure 3.4 for four angles. The black arrows show the propagation direction of the X-rays while the yellow lines indicate the central axis and the boundaries between the glass windows and the central part of the cell. As it is assumed that no X-rays pass through the steel, less and less of the cell is projected as the angle increases until it is completely shielded when the angle is slightly larger than 25°. Since the added value of these measurements was questionable, these would not be done unless enough time was left after the previous mentioned measurements were finished.

As mentioned in the introduction the emergence of COVID-19 and the lockdown that followed threw a wrench in the works and the planned measurements had to be cancelled. Up until this point two sets of preliminary measurements had been done. The first set was done in order to get familiar with the facility and the data-processing software. In these measurements a fluidized bed of 0.5 mm polystyrene particles inside a plastic cylinder was imaged. This included among others images where the X-ray source turned was off, with only air between the source and detector and with no particles in the cylinder.

The second set of measurements was done with the cell placed in between the X-ray tube and the detector. The first objective was to find out if enough X-rays would be transmitted through the cell to form an useful image as rough calculations showed that a large fraction of the incoming X-rays would be scattered or absorbed even if the cell was empty. The second objective was to find the optimal settings of the X-ray tube for the actual measurements. To do so multiple measurements were done at different voltage and current

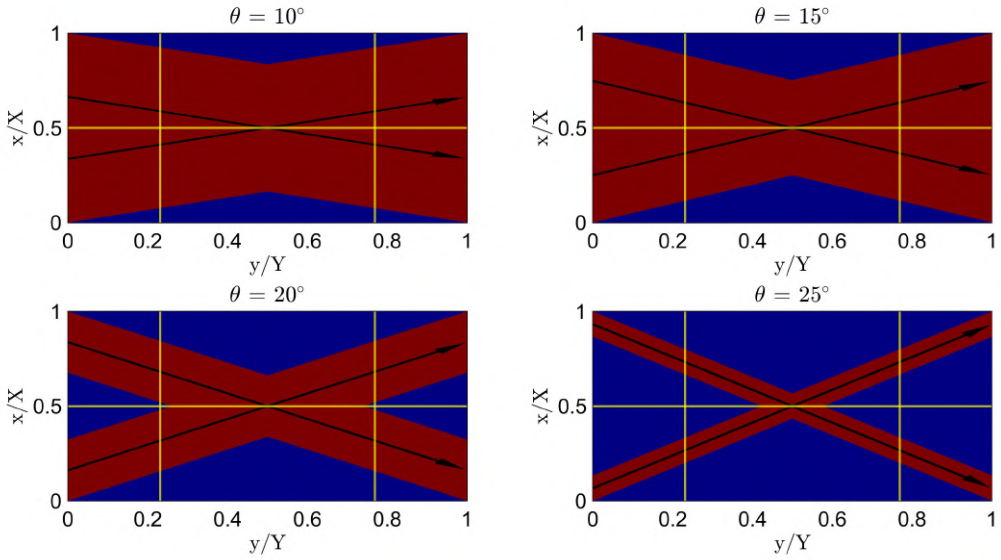

Figure 3.4: Coverage of the cell at different angles with respect to central axis.

levels. For the final measurement the cell was partially filled with 0.5 mm polystyrene particles. The results of the calculations done prior to the measurements can be seen in figure 3.5 together with the results for the particle-filled cell which were done afterwards. They were obtained using equation 2.5. Moving I_0 to the left side allows the relative intensity to be calculated. This ratio can be interpreted as the probability of an X-ray passing through the cell without interacting with the material or the percentage of X-rays with a certain energy emitted from the source transmitted through the cell.

For a cell filled with R-23 two extreme situations were assumed: one in which the density of the fluid was approximately equal to the highest possible density realized during the measurements and one in which it was equal to the lowest. For the particle-filled cell an average packing factor of 0.74 was assumed to compensate for empty space between the particles. It can be seen that almost X-rays with an energy up to 50 keV have at least one interaction in the cell. At these energies it is most likely that this interaction is absorption rather than scattering. Furthermore, the dependence of the transmission on the contents of the cell is relatively low in this region. Looking at the two bottom lines the transmission of the particle-filled cell is very similar to the transmission of the cell with the high-density R-23. A safe assumption is then that the intensity measured during the actual measurements will lie between the intensity measured with an empty cell and the intensity of the filled cell. If these two values are very close to each other it is very likely that the imaging of density structures will be very difficult.

3.2.2. Gamma transmission probing

In addition to projectional radiography using an X-ray tube another type of measurement was planned. This method would be simpler, consisting of a radioactive source and a gamma detector. Using this setup a pencil beam could be projected through the cell to probe the density field at different positions. The radioactive source selected for these measurements contained Am-241. This element decays mainly by alpha decay, emitting a gamma ray as byproduct. The energy of these gammas is primarily 59.54 keV, with lower energy gammas emitted now and then. Looking back at the results from the transmission calculations in figure 3.5, it is clear that at 60 keV a large part of the gammas interacts with either the glass or the R-23 in the cell. This can be seen even clearer in figure 3.6. Although most of the gammas would be either absorbed or scattered, it was expected that the high activity of the source, 10.5 GBq at the moment of its activation, would be able to compensate for this.

Although these measurements also had to be cancelled a couple of months into the lockdown permission was given to perform these experiments. This was possible due to this experiment belonging to a lower risk level compared to experiments with the X-ray facility which still could not be used. There were three objectives for doing these experiments. The first one was to study the density field in the cell by using the pencil beam

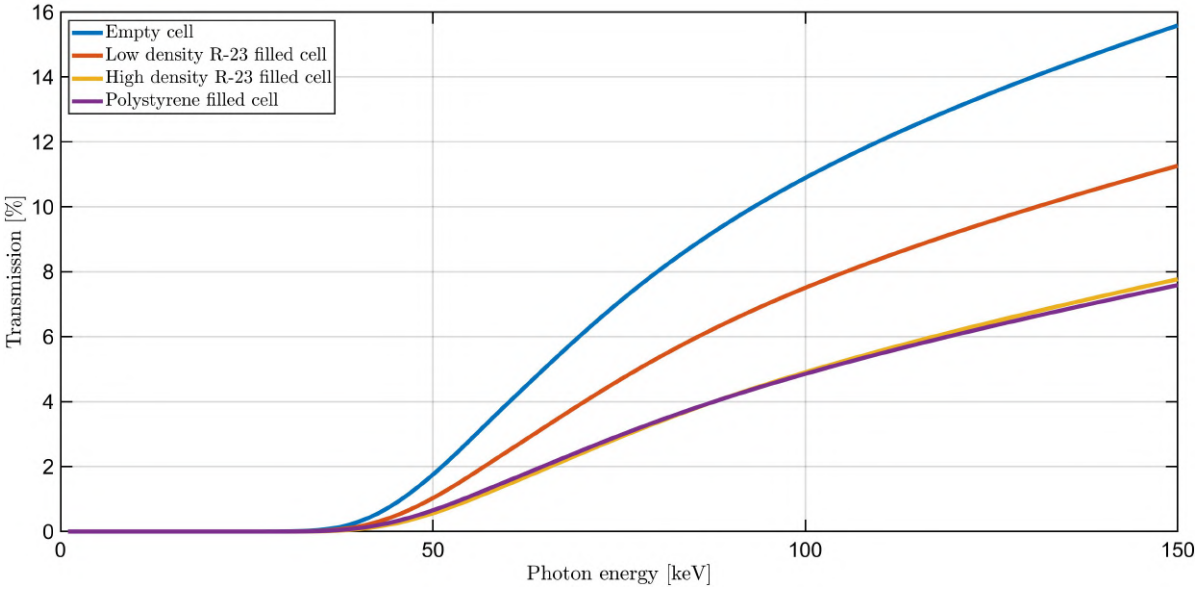

Figure 3.5: Calculation of transmission through cell filled with different materials. For the polystyrene particles the average packing factor of 0.74 was assumed.

to probe the cell at different locations. The second objective was to see how the measured intensity changed in time to get an indication of how long the measurements with the X-ray facility should be. The third was to calculate μ_ρ for R-23 and compare it to the values that had been used in calculations so far as these were calculated using the values of the individual atoms normalized by weight fraction. Although this could only be done for one energy it might still give an impression of the accuracy of this method. Unfortunately the material available for these experiments proved to be quite old and had not been used for a very long time. A lot of effort had to be put into it before a signal could be measured and the results were nonphysical at worst and unreliable at best. In the end it became clear that continuing these experiments would not lead to accomplishing any of the objectives and that time could better be spent on continuing the numerical approach.

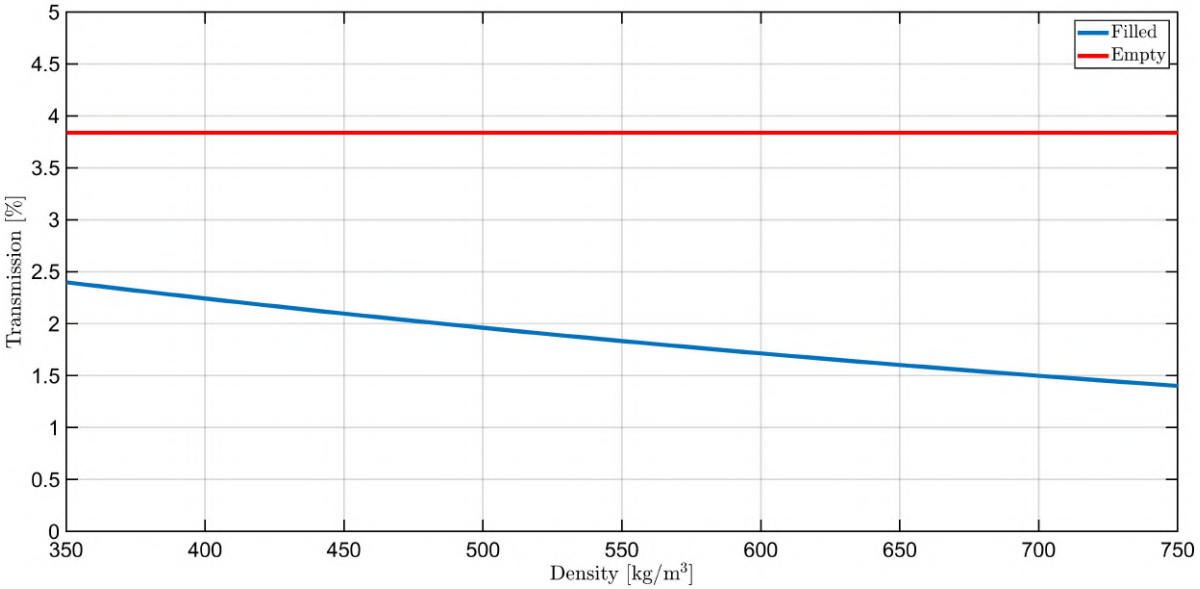

Figure 3.6: Probability of gammas propagating through the cell without interacting as function of density of the R-23..

4

Numerical approach

As the experiments in the X-ray facility had to be cancelled the decision was made to attempt to simulate them. If done correctly the results of these simulations might be used to check if the original objectives are even achievable and which steps should be undertaken to obtain the best results if this is true. Although there are already existing algorithms that can be used to simulate X-ray imaging they are often outdated, locked behind a paywall or not available for use at all. Furthermore, these programs were developed for studying objects in which different materials are largely homogeneous in density. Since supercritical fluids can exhibit relatively large density differences over small length scales a program is needed that can accurately model this. The choice was therefore made to write new code from scratch to simulate the X-ray imaging of SC fluids. The first choice that had to be made was to use either a primarily deterministic or probabilistic method. For probabilistic methods Monte Carlo simulations are often used. These simulations are based on repeated random sampling to obtain numerical results. MC simulations are considered cutting edge in the field of simulation and their results very reliable. As their method is based on random sampling they are an excellent tool to simulate the path an individual X-ray follows through matter as the possible interactions can be converted to a probability distribution to draw from. This also makes the simulation of scatter much easier compared to a deterministic method. There are nonetheless some major disadvantages. The first one is that in order to reduce the statistical error to an acceptable level generally a very large number of simulation has to be performed. This requires a lot of computation power and time. Secondly the toolkits that are available to use for these kind of simulation such as PENELOPE or Geant are often not very user-friendly and can take some time to master. Finally it was unclear if these toolkits could be effectively used to construct a supercritical density structure to study.

Looking at the deterministic method it has the advantage that it does not suffer from statistical errors. As a result deterministic simulations are in general completed much faster. Furthermore it is also not necessary to simulate individual X-rays. The code required for deterministic calculations is also in most cases less complicated, making it easier to implement. The main drawback is that it is not very suitable for simulating scattering. Scattering is essentially a stochastic phenomenon and in theory there are infinite possibilities for a scattered X-ray to still reach the detector. After comparing the advantages and disadvantages of both methods the deterministic method was selected as the best option. An option would be to add a scattering effect during data processing or use a deterministic approximation. The process of computing the virtual X-ray images can be divided into three parts: modelling the X-ray source and the emitted X-ray spectrum, assembling a virtual object representing the cell filled with SC R-23 and calculating the interactions of the X-rays with said object, and finally modelling the X-ray detection in the detector and computation of the image.

4.1. X-ray source

There are three main methods that are used in X-ray imaging simulation to calculate the X-ray spectrum produced by the X-ray tube. The first one is taking spectra that have been obtained experimentally and interpolating the data to fit the required parameters. An advantage of this method is that it is certain that the spectra have a physical basis. There are some disadvantages however. The first one is that these spectra

usually only have been measured for a low number of different parameters such as tube voltage or emission angle. As a result interpolation or extrapolation if data sets are especially limited might result in spectra that are widely divergent from reality. In addition these spectra are usually averaged over time and only show the relative intensity of the X-rays in the spectrum. This makes it difficult to accurately calculate the absolute X-ray intensity of the source. Finally the measured spectra are strictly speaking only valid for calculating spectra produced by the same model of X-ray tube.

The second method is using an analytical model to calculate the spectra. A major advantage is that this allows a much greater freedom in choosing the parameters to model the situation that is to be studied, provided the model has the option to do so. The main disadvantage is that it is difficult to check if the produced spectra are accurate. The results of such models are often validated by comparing them to the results of Monte Carlo simulations, but these have limitations of their own, or by comparing them to measured spectra. As mentioned earlier these often only provide the relative intensity and can thus not be used to validate other characteristics of the calculated spectrum. Although it is theoretically possible to very precisely model the design of the X-ray tube it is often kept very generic. This makes modeling less complicated and the results applicable in more situations. This leads to an opposite problem compared to using measured spectra where the calculations are in good agreement for a single type of tube, but might show large deviations for other types. The results from an analytical model deviate for all types of tubes, but these deviations are probably smaller than those of the measured spectra. In the end X-ray tubes have a relatively simple working principle and almost all X-ray tubes follow roughly the same design and use the same materials. It is therefore assumed that both methods produce results that are accurate enough for further calculations.

The final method is using Monte Carlo (MC) simulations of coupled electron-photon transport. As discussed in the beginning of this chapter these simulations are quite computationally intensive en require a lot of computation time, but the results are considered reliable.

4.1.1. Analytical model

In the end the decision was made to use an analytical model as its flexibility would make simulating different experimental conditions easier. Developing such a model would likely be a multiyear research program on its own and would lie outside of the scope of the project. Luckily these kind of models have already been developed with some of them freely available for use. One that has been made publicly available somewhat recently is a MATLAB implemented model developed by Omar et al. [44]. This model is a combination of two earlier developed models. The first model [45] provides a analytical description of characteristic X-ray emission with the second one [46] providing an analytical description of bremsstrahlung emission. In the paper accompanying the final model [47] an overview of previous developed models is given along with their restrictions and flaws. One major flaw that all other models share is that while they have been shown to be sufficient for certain applications the validity of their off-axis emission has been called into question. In all these models the assumption is made that the angular distribution of bremsstrahlung is isotropic. This assumption is based on the belief that electrons striking the X-ray target quickly diffuse due to multiple scattering. This has however been proven to be an inadequate approximation of the underlying physics [48]. For that reason the analytical bremsstrahlung model takes the angular distributions into account. In addition to an overview of older models the paper by Omar et al. [47] presents a summary of the methods used to develop both the bremsstrahlung and characteristic X-ray emission models. A brief explanation will also be given here, for the specifics of the used methods see Omar et al. [45] and Omar et al. [46].

The calculation of characteristic X-ray emission is based on precalculated depth distributions of X-ray fluorescence generated by excited target atoms returning to ground state. These distributions were calculated by simulations using the PENELOPE system which performs MC simulation of coupled electron-photon transport. The results from these simulations were then parameterized for use in analytical calculations. These calculations use radiative transition probabilities to calculate the characteristic X-ray fluence differential in energy, assuming isotropic emission which is in contrast to bremsstrahlung valid in this situation.

The bremsstrahlung model also combines precalculated results with an analytical description of the X-ray emission. The PENELOPE system was used to perform simulations determining the depth, directional and kinetic energy distribution of electrons impinging on a X-ray tube target. The results of these simulations were then formulated as probability and number density functions. These were then combined with NIST cross sections and attenuation coefficients from the PENELOPE materials database to calculate the bremsstrahlung energy, while the angular distribution was determined by combining them with cross sections derived from

relativistic partial-wave calculations. It should be noted that in both models the MC simulations have been performed with the electron beam normally incident on the target. This is not true in actual X-ray tubes as can be seen in figure 2.4. The justification for this assumption is that the trajectories of electrons entering the target follow the electric field lines in the interelectrode space. For conductors it is known that these are perpendicular to the surface, causing the electrons to enter the target (near) normally. Omar et al. [46] emphasize that this assumption is common in previously published models.

In the final part of the paper the results of the combined model are validated by comparing them to MC-calculated and measured spectra. The comparison shows that the models closely agrees with results from both methods for beam energies from 20 to 300 keV and take-off angles from 3 to 21°. Furthermore it performs especially well at lower energetic electron beams compared to older models. Looking at the first and second half-value layer (HVL) of aluminium, which is often used to determine beam quality, the model produces spectra that agree within 0.5% and 2% for MC-calculated and measured spectra respectively. In addition, the difference in photon energy absorption in air between the model and MC predictions is less than 0.5% while previous models can show differences larger than 10%. It should be noted that the validation was primarily done for narrow-beam geometry. For broad-beam geometry scattered X-rays also contribute to the spectrum, increasing the intensity but lowering the mean energy.

4.1.2. Model input & output

As mentioned earlier, the combined model is implemented in MATLAB and is very user-friendly with only a basic understanding of MATLAB needed to use it. A spectrum is calculated by calling a function that accepts input arguments that have been defined precedingly of which the first seven are mandatory. The first of these input arguments is the atomic number of the target material. The model accepts two values, those of tungsten and molybdenum which are the most common target materials in X-ray tubes. The second and third input argument are the incident electron energy in keV for which valid values range from 20 to 300 keV and the photon energy bin width, also in keV. The following two input arguments are used to define the take-off and out-of-plane angle. Following this the distance from the X-ray source to the detection point and the thickness of the air gap are defined. The first one is to take the inverse-square law into account while the air gap is used to calculate the attenuation of the X-rays by the air in between the source and detector. This approach ignores the fact that scattered X-rays can still reach the detector which introduces an error in broad-beam geometry spectra. The final input arguments are optional and can be used to define extrinsic filters. This is done by supplying pairs of atomic number and filter thickness. An example of the input is as follows:

```
out = XrayModel(74, 100, 1, 12, 0, 100, 100, [4,0.1], [13,0.25], [29,0.01]);
```

Here a spectrum is calculated produced by 100 keV electrons incident on a tungsten target using a 1 keV energy bin width, emitted with an 12° take-off angle and 0° out-of-plane angle. The distance between the source and detection point is 100 cm with an equally sized air gap. The source itself contains three filters: 0.1 cm beryllium, 0.25 of aluminium and 0.01 cm copper.

The output of the model is a matrix consisting of three columns, the length of which depends on the electron energy on bin width size. The first column contains the photon energy, while the second and third contain a X-ray fluence differential in energy $\Phi_E(E)$ per incoming electron, defined in equation 2.7. The difference between the two is that the fluence in the second column is of all emitted X-rays with the third only giving the fluence of characteristic X-rays. An example of a spectrum calculated by the model can be seen in figure 4.1(a). The input arguments are chosen to match the properties of the X-ray tube used in the facility. The spectrum here is essentially a probability density function, which means that to obtain the X-ray fluence it should be integrated. The easiest method is to multiply the calculated values with the energy bin width ΔE. The result of this is shown in figure 4.1(b). Each bar represents the X-ray fluence of X-rays with an energy ranging from $E-\Delta E$ to $E+\Delta E$. By choosing ΔE small enough it is justifiable to assume that all X-rays lying in that range have the same energy E. Furthermore if ΔE is chosen to large the characteristic peaks are also not calculated correctly, although this has a limited effect on the total fluence due to their contribution being relatively low, as mentioned in section 2.1.1.

Calculating the spectrum with almost 300 energy bins takes between 1 to 2 s on the hardware used. Decreasing the number of bins to 30 results in a calculation time of roughly 0.3 s. Even with the reduced bin number it is self-evident that if spectra need to be calculated for a large number of emission directions the computation time can become quite considerable. To see if this would be a necessary step the spectra for multiple

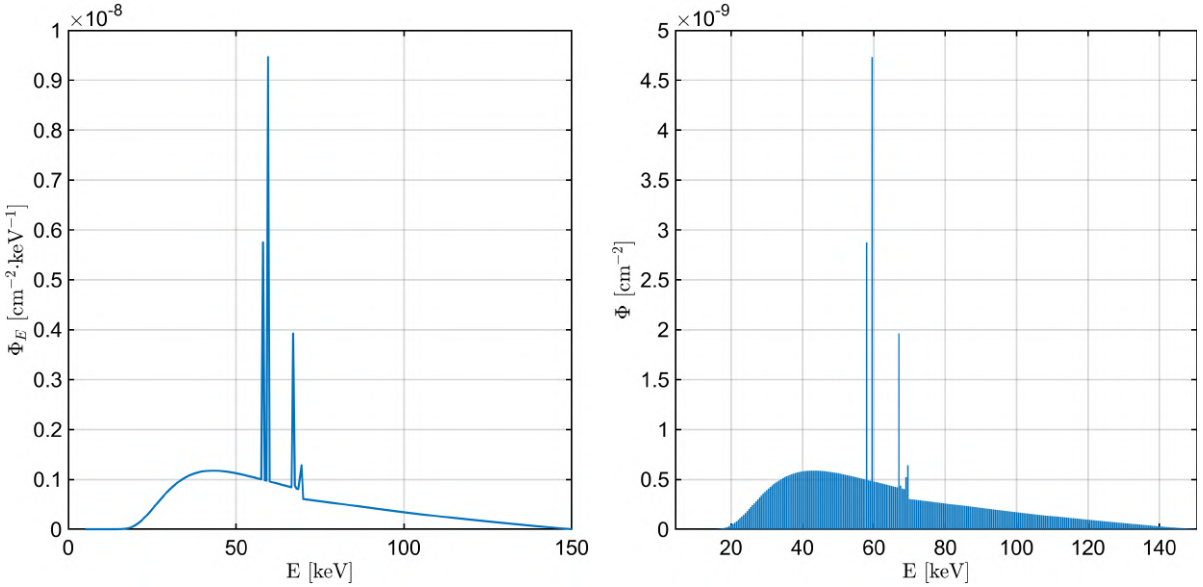

(a) X-ray fluence differential in energy per incoming electron.

(b) X-ray fluence per incoming electron.

Figure 4.1: X-ray fluence differential in energy and X-ray fluence. The spectra were generated using a tungsten target with an electron energy of 150 keV and 0.5 keV bin width. The take-off angle was set to 11° and the out-of-plane angle to 0°. The detection point distance and air gap were set to 100 cm. Two filters were added: 0.08 cm beryllium and 0.3 cm aluminium.

take-off and out-of-plane angles relevant to the geometry of the facility were calculated. In section 3.1.2 it was specified that the X-ray target in the source has an angle of 11°. This means that the central beam axis lies at a take-off angle of 11° and out-of-plane angle of 0°. In perfect conditions this axis passes through the exact middle of the cell and the detector. At the studied angles the X-rays pass through the glass windows and central cube of the cell, but not through the steel part of the flanges or the cylinder surrounding the center. In order get an overview of the influence of the emission angles on the X-ray emission the total energy fluence Ψ_T at various angle combinations was calculated by integrating the energy fluence spectra at said angles. The results are shown in figure 4.2. All other input arguments were kept equal to those used to calculate the spectra in figure 4.1(b). Due to symmetry only positive values of θ are used. From the figure it is clear that the take-off angle has a much larger influence on the total energy fluence than the out-of-plane angle. This is in agreement with the information presented in section 2.1.1 where it was explained that the heel effect has a greater effect on the emitted spectra than the relativistic effects. Looking at the values of Ψ_T for $\theta = 0$ the energy fluence is approximately 2.5% larger near the top than the fluence along the central beam axis, while it is almost 3% smaller at the bottom.

As figure 4.2 only provides insight into how the total energy fluence changes with emission angle and not into how the emitted spectrum changes multiple spectra for various take-off angles at a 0° out-of-plane angle are compared in figure 4.3. The difference between the spectra is more pronounced in the low-energy region between 30 and 50 keV. This makes sense as the intrinsic filtering in the X-ray target which lies at the root of the heel effect is stronger at lower energies. Furthermore ignoring the characteristic peaks the differential fluence is the largest here resulting in the largest absolute differences. Besides the differences in total energy fluence being relatively small it was assumed that the beam hardening as a result of the X-rays passing through the cell would decrease these differences even further. A quick calculation with the X-rays now passing through the glass windows confirmed this with the differences between top and middle and bottom and middle being reduced to 0.67% and 1.14% respectively. At this point it was decided that these differences were too small to justify the increase in computation time by calculating the spectrum for each emission direction. A better option would be to compensate for this error during the data processing phase in the case that it could have noticeable effect on the final results.

An aspect of the X-ray tube that should be taken into account is that the electron beam incident on the target is not a perfect pencil beam and has a finite focal spot size. This means the X-ray source likewise has a focal spot size and is not a point source contrary to what the model assumes. This finite size can in certain situations introduce blur to images. There are two methods that are commonly used to correct for this. The

first option which is used by among others Duvauchelle et al. [49] is to use multiple point sources which have a spatial distribution and resembling the shape and size of the focal spot. The emission intensity of these sources is then set in such a way that their total output is equal to that of the X-ray source that is modelled. If even higher precision is needed these sources can weighted with an intensity coefficient as in reality the emission intensity in the middle of the focal spot is higher than at the edges. A major disadvantage of using this method is that the number of times the overall simulation has to be executed increases with the number of point sources. This can quickly result in unfeasible long computation times.

The second option is much simpler and time efficient. After an image is computed blur is introduced by filtering it with a certain function, usually a Gaussian. Examples of this are Zhou et al. [50] who used a Gaussian function with a standard deviation equal to the focal spot size and Cao et al. [51] who modeled the modulation transfer function (MTF) of the source with a Gaussian function dependent on the focal spot size and system magnification.

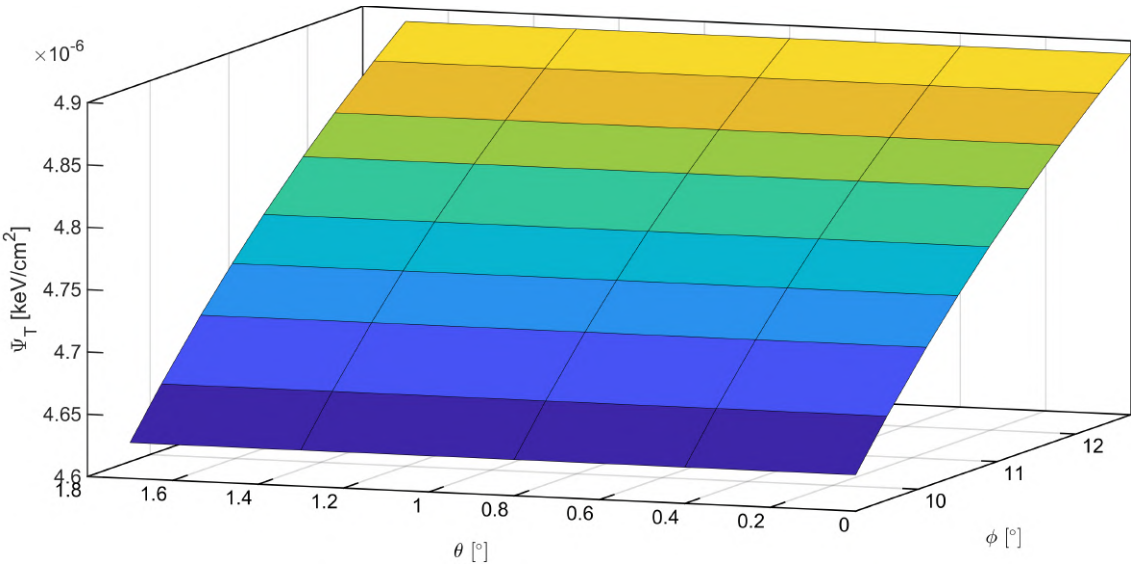

Figure 4.2: The total energy fluence as a function of the take-off angle ϕ and the out-of-plane angle θ.

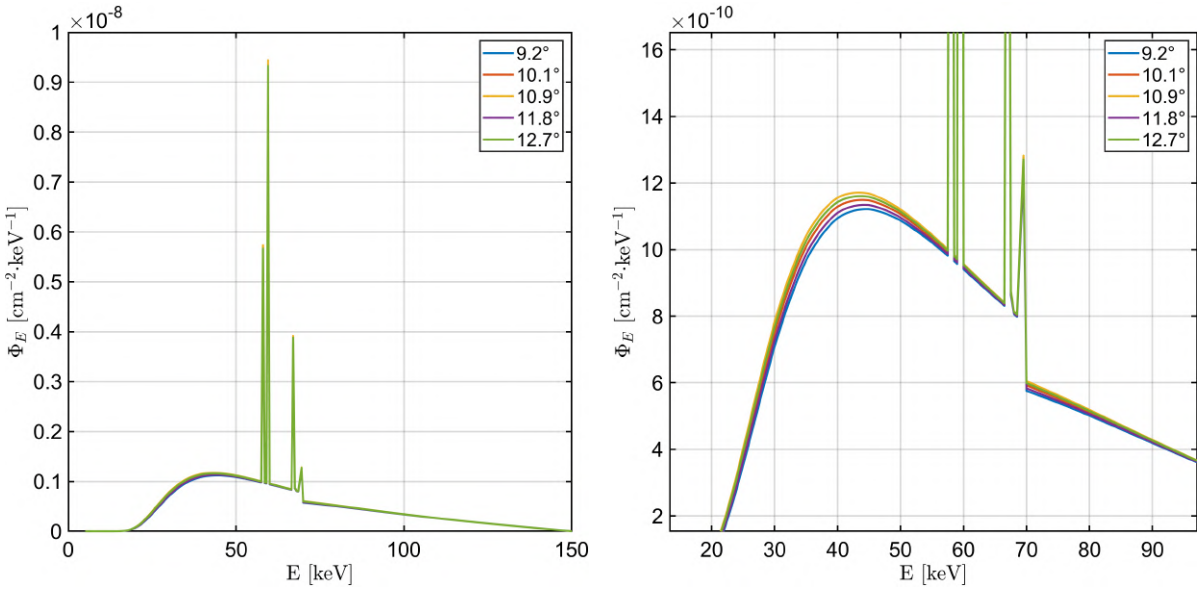

(a) X-ray fluence differential in energy per incoming electron for various take-off angles.

(b) Close-up of the X-ray fluence differential in energy for various take-off angles.

Figure 4.3: X-ray fluence differential in energy spectra for various take-off angles and a 0° out-of-plane angle.

4.2. X-ray transport & Interaction

AFTER the X-rays are emitted from the X-ray tube they travel towards the object where they are attenuated. In order to accurately model the attenuation in the cell the cell itself has to be converted to a digital version, a phantom that can be used to represent the SC R-23 has to be found and placed in the digital cell and the interactions of the X-rays throughout the cell have to be calculated.

4.2.1. Cell geometry

In X-ray radiography simulations there are two methods that are commonly used to describe the sample geometry. The first one uses polygon meshes which are generally triangular, while the second one uses voxels which are the 3D representation of pixels. Polygon meshes are represented by the coordinates of their vertices and can be efficiently used to represent simple 3D structures. If a sample consists of different parts made of different materials these can be handled independently. Examples of models using this method are the models developed by Duvauchelle et al. [49] and Freud et al. [52]. Using meshes has two main advantages. The first one is that objects with non-rectangular surfaces can be accurately represented if the mesh size is chosen small enough. The second advantage is that if the sample or the parts it is made of are homogeneous only a relative small number of polygons is needed to describe the sample, as only the surfaces and not the insides have to be modelled. This advantage becomes a disadvantage however if the object contains parts with large inhomogeneities as now a very large number of small volumes has to be modelled.

Voxels (coming from the words "volume" and "element") represent values on a regular 3D grid and can be viewed as cuboid LEGO bricks used to build structures. It is easy to imagine that to construct for example a three-dimensional homogeneous pyramid many very small voxels are needed in order to get a structure that closely resembles a pyramid. Using triangular meshes would on the other hand require only five data points to construct a pyramid. On the other hand if the content of the pyramid is not homogeneous but contains many small elements of different material or density the situation changes. Such an element can be modelled using a single voxel, but requires at minimum four mesh points since this is the minimum number of triangular surfaces needed to form a closed volume. In this case using voxels is much more efficient.

Since the motivation behind the planned experiments was the fact that SC fluids can exhibit large density differences over small length scales the need to use of small volume elements to model the fluid is self-evident. The choice to make use of a voxel-based geometry was therefore an easy one as this would very likely be more efficient. Furthermore using voxels to construct a sample in MATLAB is very intuitive as a simple three-dimensional matrix can be used which can be easily manipulated. This method does make it rather compli-

cated to create very detailed structures, but since the only X-rays of interest are those that pass through the cube in the middle of the cell and the steel cage surrounding it absorbs essentially all incoming X-rays it was deemed acceptable to use a very simplified representation of the cell. The geometry used in the simulations was a solid stainless steel cylinder with circular glass windows in the front and back and a cube in the middle which could be filled with a material of choice, representing a very simplified version of the cell seen in figure 3.1(b). This approach ignores essentially all internal components of the cell such as the copper plates at the top and bottom of the internal cube and the lateral glass walls. Since these components do not directly influence the imaging of the SC fluid and those that are located behind the steel part of the flanges are shielded regardless it was expected that leaving them out would not decrease the validity of the results. The voxelated cell with an empty core is shown in figure 4.4 with 1 mm cubic voxels. The blue voxels represent the glass windows and the gray voxels the stainless steel.

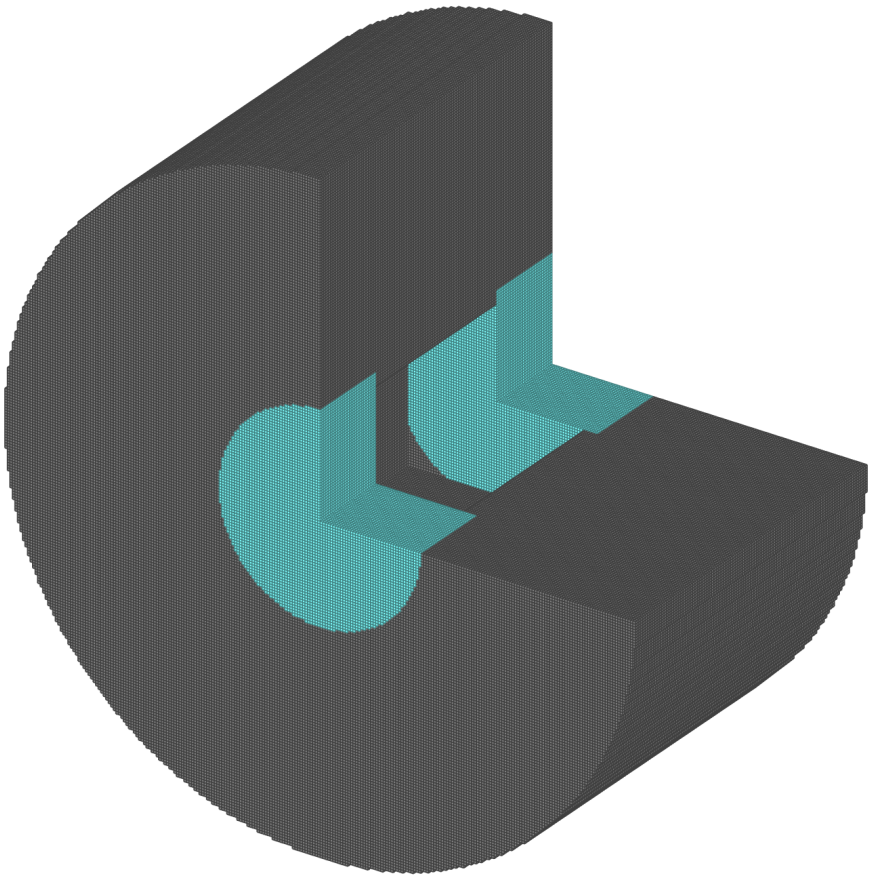

Figure 4.4: Voxelated representation of the empty RB-cell. The blue voxels represent the glass windows and the gray ones the stainless steel. 1 mm cubic voxels were used.

The next step was to find a phantom representing the density structure of SC R-23 that could be placed in the cell. The best-case scenario would be to use to results of simulations of R-23 in the RB cell in different experimental conditions. Unfortunately these results did not exist and doing them would be its own separate project. Furthermore as discussed in the introduction numerical models are still unable to accurately predict SC behaviour. A second option would be to create such a phantom manually, but it would likely show artificial density structures not representative of those in a real fluid. Fortunately there appeared to be a better option. Besides R-23 Valori [41] also studied water and methanol in a RB cell in which the central cube was very similar to the one depicted in figure 3.1(a). These experiments are described in chapter 2. Complementary to these experiments numerical simulations of the materials in the same experimental conditions were performed by Peeters [53], who was willing to provide some of the results for use in the radiography model. These simulations were performed non-dimensionally and with a constant temperature difference of 9.6 K between the top and bottom copper plate. A cross section of an instantaneous temperature field is shown in figure 4.5(a). From the colorbar it can be seen that the lowest value is almost 0 and the highest approximately

1. In order to get a density field the dimensionless values were converted to temperature by equating the 0 value to the temperature of the top plate and the 1 value to the temperature of the bottom plate and subsequent linear interpolation of the values in between. This temperature field could then converted to a density field [14] using the experimental conditions in tables 3.1 and 3.2 and the CoolProp database [14]. An example can be seen in figure 4.5(b) which shows a cross section of a density field calculated using the experimental conditions corresponding to max$\Delta\rho$ in table 3.1. Although this method produces artificial density fields for SC R-23 and it is very likely they look very different in reality they do contain realistic structures that can be effectively used to study how much detail is preserved in the final image.

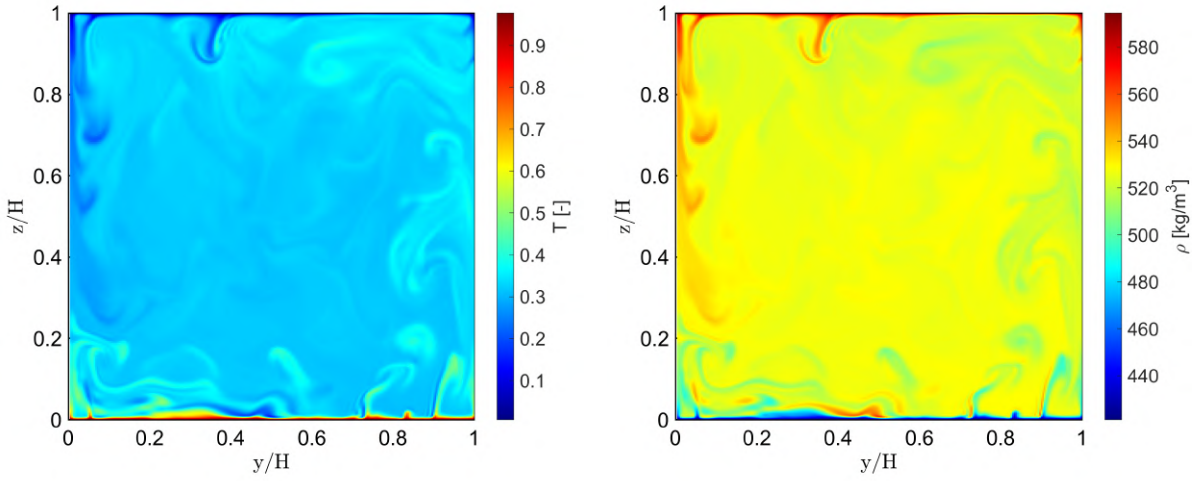

(a) Cross section of the dimensionless temperature field.

(b) Cross section of the calculated density field.

Figure 4.5: Cross sections of the dimensionless temperature field and the density field calculated using the dimensionless temperature field calculated by Peeters [53] and the experimental conditions corresponding to max$\Delta\rho$ in table 3.1.

4.2.2. Ray tracing

Since a deterministic method was chosen the particle nature of photons can be ignored and the refractive index for X-ray radiation is very close to unity [23] unattenuated X-rays reaching a detector pixel can be modelled as a pencil beam originating from the X-ray tube. In order to calculate the attenuation of such a beam the radiological path of the beam in the object is needed. The radiological path is defined as the product of the density of a material and the path length of the beam through it, usually expressed in g/cm^2. In equation 2.5 the radiological path is equal to ρx. For a ray passing through an object made out of voxels the radiological path of said ray can be written as:

$$d = \sum_i \sum_j \sum_k l(i,j,k)\,\rho(i,j,k) \tag{4.1}$$

where $\rho(i,j,k)$ is a particular voxel density and $l(i,j,k)$ the path length contained by that voxel. This is a problem for which ray tracing is a convenient method to solve it. Ray tracing is a technique used in 3D computer graphics to render light. A very simplified explanation is that a ray is cast from an imaginary eye through a virtual screen onto an object visible trough it. By calculating how many rays are reflected from the object towards the light source the apparent colour of the object and its shadow can be visualized. In this method the path of a light ray is traced in reverse compared to reality, where light is obviously emitted from a source and is reflected from an object into an "eye". The same method can be used to trace the path of an "X-ray" ray through an object, although there is clearly a big difference. Contrary to visible light which is either absorbed by or reflected from the surface of an object X-rays have the ability to pass through the object. If one is only interested in the unattenuated X-rays emerging from the other side this makes the problem easier compared to visible light ray tracing as reflection/scattering can be ignored. On the other hand, if scattered X-rays are a subject of interest it becomes much more complicated, as X-rays can scatter along the entire path through the object and can additionally undergo multiple scatter interactions inside it.

To find the radiological path of X-rays incident on a pixel a ray is cast between the X-ray point source and the middle of the pixel. After it is cast the path is followed from the origin to the endpoint. At a certain point the ray intersects with the surface of the object and enters a voxel after which the coordinates of entry are registered. The ray continues until it intersects with another plane, leaving the first voxel and either entering a second one or leaving the object entirely. The coordinates of the second intersection are also registered and can then be used in combination with the first set to calculate the path length $l(i,j,k)$ in the first voxel and to identify its indices. If the ray did not leave the object the process repeats until passes through the outer surface again, after which it reaches the pixel. Multiplying the path length of each voxel it passed through with its corresponding density and summing over all voxels gives the total radiological path of a ray. The ray tracing process can then be repeated for other pixels.

Finding the intersection points is the essence of the problem and also the most complicated part. The first attempt to find a method to do this made use of the fact that voxelated structure could be seen as sets of planes perpendicular to the x-, y- and z-axis. A ray cast from the source to a pixel crosses a number of these planes and the intersection points could be found be solving the equation describing the intersection of a line and a plane, which is a generally a trivial problem. While this method was proven to work it was very time inefficient and it was clear that using it to perform ray tracing for many pixels would take too much time. A modified approach that used the fact that the spacing between the planes is constant was being explored, but before this could be finished an already completed algorithm was discovered. Developed by Siddon [54] and commonly known as the Siddon algorithm, it also considers the voxels as orthogonal sets of equally spaced, parallel planes rather then independent elements, visualized in figure 4.6. As determining the intersections of a ray with equally spaced, parallel planes is a simple problem as the equal spacing makes only determining the first intersection necessary. All subsequent intersections can be found by recursion. The algorithm will be given a brief explanation here, see the paper by [54] for a more detailed discussion.

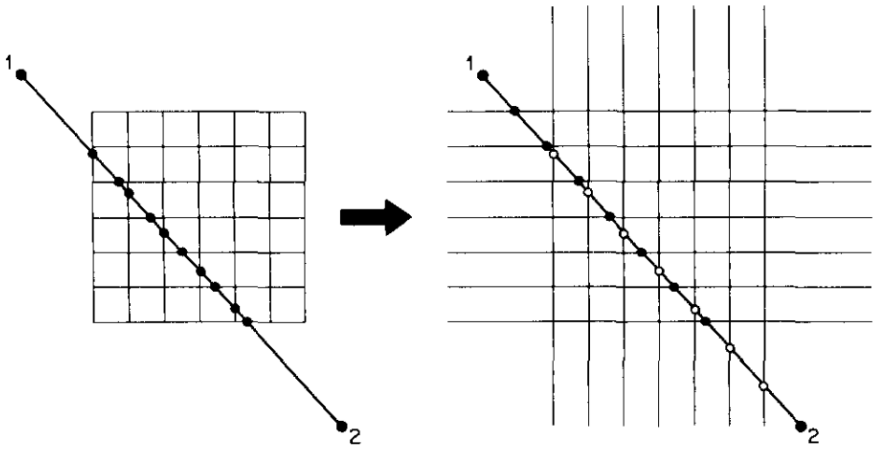

Figure 4.6: The pixels of the CT array (left) may be considered as the intersection areas of orthogonal sets of equally spaced, parallel lines (right). The intersections of the ray with the pixels are a subset of the intersections of the ray with the lines. The intersections of the ray with the lines are given by two equally spaced sets: one set for the horizontal lines (filled circles) and one set for the vertical lines (open circles). The generalization to a three-dimensional CT array is straightforward [54].

The first step is parameterizing the ray from point 1 to point 2:

$$X(\alpha) = X_1 + \alpha(X_2 - X_1) \tag{4.2a}$$

$$Y(\alpha) = Y_1 + \alpha(Y_2 - Y_1) \tag{4.2b}$$

$$Z(\alpha) = Z_1 + \alpha(Z_2 - Z_1) \tag{4.2c}$$

where the parameter α is zero at point 1 and unity at point 2. The parametric values corresponding to the intersections with the sides are given by α_{min} and α_{max}, describing the point of entry and exit respectively. If point 1 lies in the array α_{min} is equal to zero, while α_{max} is equal to one if point 2 lies in the array. The parametric values corresponding to the intersections of the ray with the planes must lie in the range [α_{min},α_{max}]. Merging the sets of parametric values corresponding to the sets of planes into one set of increasing parametric values allows the calculation of the path lengths in each voxel crossed, as it is simply the difference

between two adjacent values in the merged set. For each voxel path length the indices are determined which allows the total radiological path to be calculated. Determining the parametric values goes as follows. First the orthogonal sets of planes are calculated. For an array consisting of (N_x-1, N_y-1, N_z-1) voxels the sets can be written as

$$X_{plane}(i) = X_{plane}(1) + (i-1)d_x \quad (i = 1, ..., N_x) \tag{4.3a}$$
$$Y_{plane}(i) = Y_{plane}(1) + (i-1)d_y \quad (j = 1, ..., N_y) \tag{4.3b}$$
$$Z_{plane}(i) = Z_{plane}(1) + (i-1)d_z \quad (k = 1, ..., N_z) \tag{4.3c}$$

where d_x, d_y and d_z are the distances between the planes, which are equal to the length of the voxel sides. α_{min} and α_{max} can then be found by calculating the minimum and maximum values of α for each set of planes, corresponding the intersection with the sides of the array. If $X_2 - X_1 \neq 0$ then

$$\alpha_x(1) = \frac{X_{plane}(1) - X_1}{X_2 - X_1} \tag{4.4a}$$

$$\alpha_x(N_x) = \frac{X_{plane}(N_x) - X_1}{X_2 - X_1} \tag{4.4b}$$

with identical equations for the other sets of planes. In the case that the denominator is equal to zero the values of α are undefined and are simply excluded. The values of α_{min} and α_{max} are then given by

$$\alpha_{min} = \max\{0, \min[\alpha_x(1), \alpha_x(N_x)], min[\alpha_y(1), \alpha_y(N_y)], min[\alpha_z(1), \alpha_z(N_z)]\} \tag{4.5a}$$
$$\alpha_{max} = \min\{1, \max[\alpha_x(1), \alpha_x(N_x)], max[\alpha_y(1), \alpha_y(N_y)], max[\alpha_z(1), \alpha_z(N_z)]\} \tag{4.5b}$$

As only a subset of the intersected planes have parametric values that lie in the valid range the range of indices (i_{min}, i_{max}), (j_{min}, j_{max}) and (k_{min}, k_{max}) corresponding to these planes have to be determined.

If $(X_2 - X_1) \geq 0$

$$i_{min} = N_x - \frac{X_{plane}(N_x) - \alpha_{min}(X_2 - X_1) - X_1}{d_x} \tag{4.6a}$$

$$i_{max} = 1 + \frac{X_1 + \alpha_{max}(X_2 - X_1) - X_{plane}(1)}{d_x} \tag{4.6b}$$

If $(X_2 - X_1) \leq 0$

$$i_{min} = N_x - \frac{X_{plane}(N_x) - \alpha_{max}(X_2 - X_1) - X_1}{d_x} \tag{4.6c}$$

$$i_{max} = 1 + \frac{X_1 + \alpha_{min}(X_2 - X_1) - X_{plane}(1)}{d_x} \tag{4.6d}$$

with similar equations for j and k. These indices can then be used to calculate the valid sets of parametric values $\{\alpha_x\}$, $\{\alpha_y\}$ and $\{\alpha_z\}$ using the following equations:

If $(X_2 - X_1) \geq 0$

$$\{\alpha_x\} = \{\alpha_x(i_{min}), ..., \alpha_x(i_{max})\} \tag{4.7a}$$

If $(X_2 - X_1) \leq 0$

$$\{\alpha_x\} = \{\alpha_x(i_{max}), ..., \alpha_x(i_{min})\} \tag{4.7b}$$

where

$$\alpha_x(i) = \frac{X_{plane}(i) - X_1}{X_2 - X_1} = a_x(i-1) + \frac{d_x}{X_2 - X_1} \tag{4.7c}$$

These sets are merged into one set $\{\alpha\}$ with its values in ascending order. To include the case where one or both points 1 and 2 lie inside the array $\{\alpha\}$ is appended with α_{min} and α_{max}:

$$\begin{aligned}\{\alpha\} &= \big\{a_{min}, \text{merge}\big[\{\alpha_x\},\{\alpha_y\},\{\alpha_z\}\big], \alpha_{max}\big\} \\ &= \big\{\alpha(0),...,\alpha(n)\big\}\end{aligned} \tag{4.8a}$$

The index n in the last term is given by

$$n = (i_{max} - i_{min} + 1) + (j_{max} - j_{min} + 1) + (k_{max} - k_{min} + 1) + 1 \tag{4.9}$$

The path length $l(m)$ in a particular voxel defined by intersections m and $m-1$ is then given by

$$l(m) = d_{12}\big[\alpha(m) - \alpha(m-1)\big] \quad (m = 1,...,n) \tag{4.10}$$

where d_{12} is the distance between point 1 and 2:

$$d_{12} = \sqrt{(X_2 - X_1)^2 + (Y_2 - Y_1)^2 + (Z_2 - Z_1)^2} \tag{4.11}$$

The final part of the problem that needs to be solved is finding the indices $\big[i(m), j(m), k(m)\big]$ of the voxel. These are determined by finding the midpoint of the two intersections as this should lie in the voxel. Using this knowledge the indices can be calculated using

$$i(m) = 1 + \frac{X_1 + \alpha_{mid}\,(X_2 - X_1) - X_{plane}(1)}{d_x} \tag{4.12a}$$

$$j(m) = 1 + \frac{Y_1 + \alpha_{mid}\,(Y_2 - Y_1) - Y_{plane}(1)}{d_y} \tag{4.12b}$$

$$k(m) = 1 + \frac{Z_1 + \alpha_{mid}\,(Z_2 - Z_1) - Z_{plane}(1)}{d_z} \tag{4.12c}$$

where α_{mid} is given by

$$\alpha_{mid} = \frac{\alpha(m) - \alpha(m-1)}{2} \tag{4.12d}$$

Finally the radiological path in equation 4.1 of a ray going from point 1 to 2 can be written as

$$\begin{aligned} d &= \sum_{m=1}^{m=n} l(m)\rho\big(i(m), j(m), k(m)\big) \\ &= d_{12} \sum_{m=1}^{m=n} \big[\alpha(m) - \alpha(m-1)\big]\rho\big(i(m), j(m), k(m)\big)\end{aligned} \tag{4.13a}$$

Some adjustments to the algorithm had to be made as MATLAB uses a different form of indexing and the paper by Siddon [54] does not state that the results from equations 4.6 and 4.12 should be rounded down to get integer values, although this should be self-evident. Modifications were also made to make sure the algorithm also works for cases where a denominator is equal to zero, as these cases were ignored in the paper. This algorithm was much more time-efficient than the method previously used, but improvements could still be made. Jacobs et al. [55] studied Siddon's algorithm and found that the frequent use of equations 4.12 where floating points are converted to integers limits its speed. They developed an altered algorithm that is still based on Siddon's, but only uses these equations once per ray.

They follow the same method as Siddon up to and including equation 4.6. After this their method becomes different. They first calculate the number of planes N_p crossed by the ray passing through the array after it has entered it. They then only use equations 4.12 once to calculate the indices of the first intersected voxel. After the first intersected voxel is found the ray is followed until it crosses the next plane. Depending on which plane is crossed the parameter and index corresponding to that plane are updated, the path length in the voxel is calculated and used to increase the total radiological path. In order to illustrate this process the

case of crossing the x-plane is discussed.

$$l(i,j,k) = (\alpha_x - \alpha_c) d_{12} \tag{4.14a}$$
$$d = d + l(i,j,k)\rho(i,j,k) \tag{4.14b}$$
$$i = i + i_u \tag{4.14c}$$
$$\alpha_c = \alpha_x \tag{4.14d}$$
$$\alpha_x = \alpha_x + \alpha_{xu} \tag{4.14e}$$

where

$$\alpha_{xu} = \frac{d_x}{|X_2 - X_1|} \tag{4.14f}$$

and

$$i_u = \begin{cases} 1, & \text{if } X_1 < X_2 \\ -1, & \text{else} \end{cases} \tag{4.14g}$$

By running through this part N_p times the total radiological path is calculated. Determining which subsequent plane is crossed is done by comparing α_x, α_y and α_z, with the smallest parameter corresponding to said plane.

Although this algorithm required even more modifications to get it working it indeed proved to be faster than Siddon's. Although newer algorithms such as the one developed by Zhao and Reader [56] can be found that are even faster according to their own comparisons increasing the speed at which the path lengths are calculated would not noticeably reduce the total computation time at this point. This will be further explained in the next section. Figure 4.7 shows a visualization of the final algorithm casting a ray (red line) through a sample (blue cube) and selecting the voxels it passed through (green cubes).

4.2.3. Interaction

Now that the path length and density of each voxel crossed by a ray is known the final part that still needs to be completed to calculate the attenuation in the voxels is finding the correct value for μ_ρ in equation 2.5. Fortunately extensive databases already exist containing total and partial attenuation coefficients for almost all elements and selected materials of interest. One of the most used databases for radiological calculations is the XCOM database [32] which is maintained by the National Institute of Standards and Technology (NIST). This database can be used to calculate total and partial mass attenuation coefficients for any element, compound or mixture for Z ≤ 100 and energies ranging from 1 keV to 100 GeV. These coefficients are based on theoretical calculations and semi-empirical formulas for neutral, isolated atoms. Attenuation coefficients of compounds and mixtures are calculated with the use of Bragg's additive law:

$$\mu_\rho = \sum_i w_i \left(\mu_\rho\right)_i \tag{4.15a}$$

where

$$w_i = \frac{a_i A_i}{\sum_j a_j A_j}$$

Here μ_ρ is the mass attenuation coefficient of a compound or mixture, $\left(\mu_\rho\right)_i$ the mass attenuation coefficient of the ith element and w_i the corresponding weight fraction. Additionally a_i is the number of formula units in the compound or mixture and A_i the atomic weight. This approach assumes that the attenuation coefficient of an atom does not change when its part of a molecule and ignores the fact that the binding energies of electrons change when elements bond with each other. For example the electron binding energy for an isolated hydrogen atom is the famous 13.6 eV, but isolated hydrogen atoms are very rare in normal conditions. It is far more likely to found hydrogen atoms covalently bound to another hydrogen atom in the form of a hydrogen molecule, for which the electron binding energy is approximately 16.4 eV [57]. It is also possible for bonds between atoms to lower the binding energy, an example being F_2 which has a lower binding energy than F. In section 2.1.2 it was explained the electron binding energies have a considerable influence on the

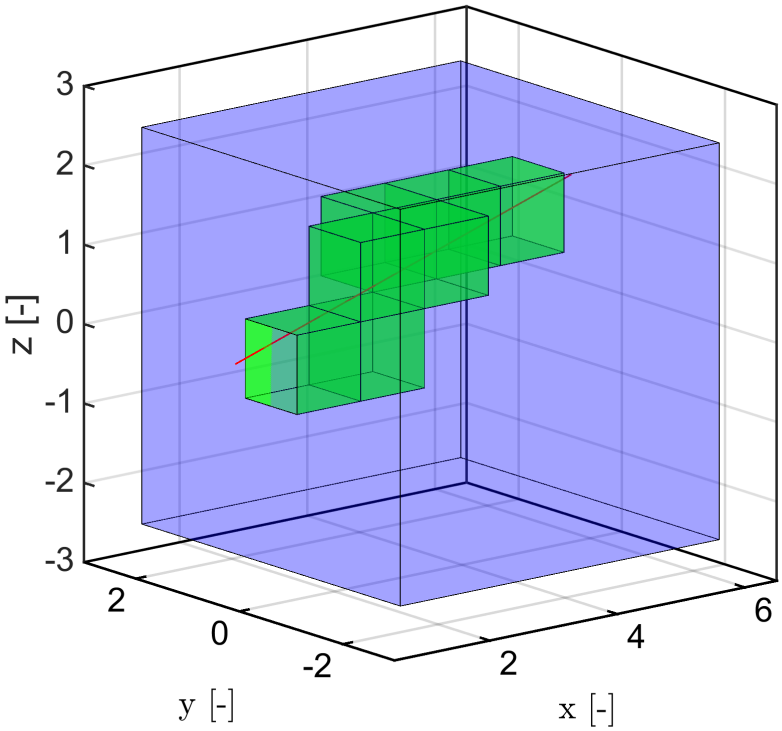

Figure 4.7: Visualization of the ray trace algorithm selecting the voxels the ray passed through. The blue cube resembles the total sample while the green cubes are voxels crossed by the ray.

attenuation coefficient of an element, mostly through the photoelectric effect. A change in the binding energies results in a change in position and possibly the amplitude of the absorption edges corresponding to the electron shells.

Looking at other cross section databases the same problem is encountered. In a perfect world the attenuation coefficients would be calculated for all possible molecules, but due to the sheer number of possible molecules and complexity of the required this is a herculean task and not feasible at the moment. The validity of Bragg's law has been studied in the past, among others by Kerur et al. [58], Kaginelli and Kerur [59] and Crewson [60]. By comparing experimental results with theoretical calculations they indeed show that the law breaks down near absorption edges, but is still a good approximation further away.

Although other databases suffer from the same problem with respect to calculation of attenuation coefficients of compounds and mixtures they still might be worth using if their coefficients for isolated atoms are more accurate compared to those in the XCOM database. Much of the database contents are based on calculations done as early as the 1960s, so it is not hard to imagine more accurate results have been obtained in the period between then and now. An other commonly used cross section database is the Evaluated Photon Data Library (EPDL) developed by the Lawrence Livermore National Laboratory (LLNL). In a study by Zaidi [61] four databases including XCOM were compared to the EPDL97 version of EPDL which has become a standard in the nuclear reactor industry. The authors notes that although EPDL and XCOM are treated as independent databases in their study they recognize that they are closely related since EPDL97 was produced as a result of collaboration between NIST and LLNL. Furthermore EPDL uses many of the same methods and calculations XCOM also uses [62]. The results from the study show that the differences in attenuation coefficients between the databases are very small, except for the coherent scattering attenuation at very low energies where significant discrepancies can be seen. Han et al. [63] also compared multiple cross section compilations focusing

on the photoelectric effect and found only small differences between XCOM and EPDL97, which they relate to the granularity of tabulations. As the XCOM database has been receiving updates up until 2010 it is worth investigating how the EPDL database has changed. In the paper by Han et al. [64] and the complementing paper by Basaglia et al. [65] the photoelectric cross sections of the latest EPDL version contained in the EPICS2017 collections were evaluated. They concluded that for existing Monte Carlo particles transport code there was no need to move to the newer version as there was no evidence the newer computational methods surpassed the compatibility of the EPDL97 version with experimental data. Finally the main author behind the EPDL database stated that he considers XCOM and EPDL equally valid; differences in results should be considered estimation of the uncertainty in the data and do not indicate if one is better than the other [66]. Furthermore he emphasizes that macroscopic quantities such as energy deposition are little affected by errors in the cross sections around absorption edges if far enough away from them.

Considering all above mentioned information and the fact that the web-based XCOM database has a user-friendly UI which made it very easy to extract attenuation coefficients for mixtures and compounds the decision was made to use the XCOM database as a source for the required coefficients. The total and partial mass attenuation coefficients of R-23 and the borosilicate glass used in the cell flanges are plotted in figures 4.8(a) and 4.8(b) respectively. For R-23 no absorption edges can be seen, which makes sense as none of the constituent atoms have absorption edges above 1 keV, minimizing the error that use of Bragg's law introduces. The glass however contains some heavier elements and as a result some edges can be seen. Fortunately only one is located above 20 keV at approximately 35 keV. Figure 4.3(a) gives an indication of the X-ray energy spectrum reaching the cell and it can be seen that virtually none of the X-rays have an energy lower than approximately 20 keV. As a result the inaccuracies in the absorption edges below this energy do not affect the results. Although the highest absorption edge does lie in the relevant part of the spectrum most of the X-rays will have an energy above it which will only increase due to beam hardening in the cell. It is therefore also assumed that this edge will not influence the accuracy of the results significantly. In order to get the values of the attenuation coefficients at the arbitrary energies interpolation is required as the XCOM values are only tabulated for a limited number of energies. This interpolation needs to be done using a LOG-LOG scale to avoid errors.

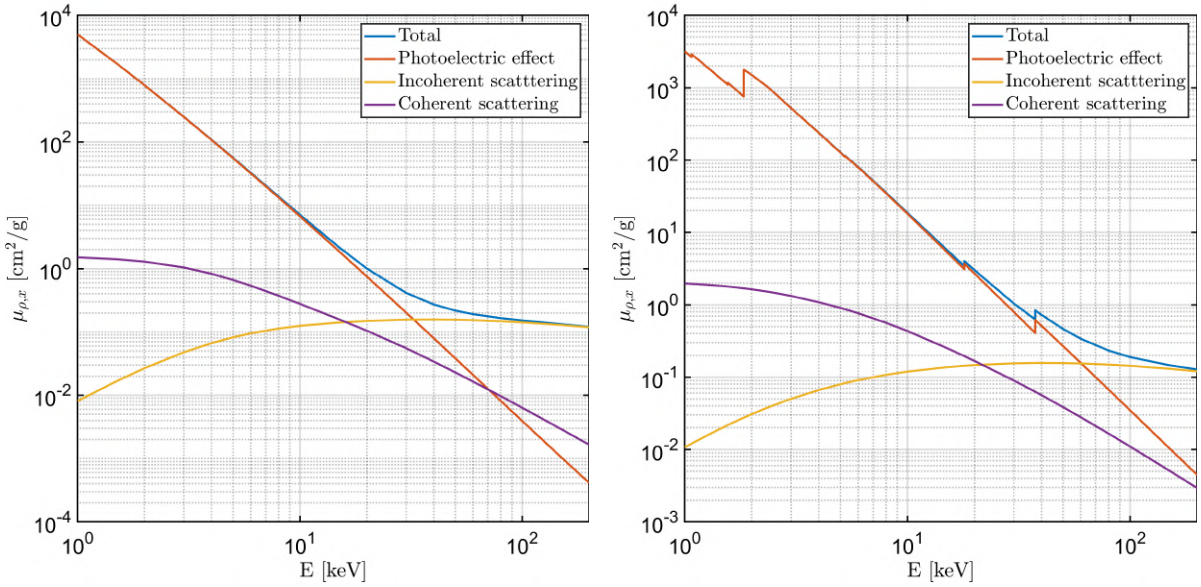

(a) Total and partial mass attenuation coefficients of R-23.

(b) Total and partial mass attenuation coefficients of borosilicate glass.

Figure 4.8: Total and mass attenuation coefficients of R-23 and the borosilicate glass used in the flanges. Values taken from the XCOM database [32].

Now that the mass attenuation coefficients are known the interactions of X-rays in the cell can be simulated. One thing that has not been addressed however is that both the algorithms by Siddon [54] and Jacobs et al. [55] assume the array only consists of a single material which means that a voxel only has to be characterized by its density. If an object consists of multiple materials this is no longer enough, as two voxels of different

material but with the same density will not attenuate an X-ray identically. The solution used for this problem was to construct a second sample identical to the one described in 4.2.1, but instead of density each voxel contains a code used to identify the material in the voxel. As the samples are identical the results of ray tracing for the first one are also valid for the second one. The interactions of the X-rays with the cell are split into two parts that are simulated separately: in the first one the transmission of X-rays is simulated. These are the X-rays that do not interact between the X-rays source and the detector and form the primary image signal. The second part treats the scattering of X-rays which form the secondary image signal and reduce detail visibility.

X-ray transmission

Calculation of the fraction of X-rays that is not attenuated is fairly simple. A discrete version of equation 2.5 is used:

$$(\Phi_E)_{det} = \Phi_E e^{-\sum_m^{m=n} \mu_{\rho,m}(E) l_m \rho(i_m, j_m, k_m)} \tag{4.16}$$

where $(\Phi_E)_{det}$ is the photon fluence spectrum reaching a detector pixel and Φ_E the photon fluence spectrum that would reach the pixel if no sample was placed in between the source and detector. This method requires calculation of Φ_E for each pixel which depending on the number of energy bins takes 1 to 2 s. Considering the detector has almost 2.4 million pixels the total computation time would be almost 28 days at best. Saying this is unfeasible is stating the obvious, so different approach had to be used. In section 4.1.2 it was shown that X-ray tube output model varies little with the out-of-plane angle and that the heel effect also becomes much less noticeable due to beam hardening. Considering this the decision was made to only calculate the spectrum once for a ray pointing at the middle of the detector with the distance between the source and the point of evaluating the spectrum set to unity. Using this equation 4.16 can be rewritten as

$$(\Phi_E)_{det} = \frac{(\Phi_E)_0}{d_{12}^2} e^{-\sum_m^{m=n} \mu_{\rho,m}(E) l_m \rho(i_m, j_m, k_m)} \tag{4.17}$$

where $(\Phi_E)_0$ is the base spectrum and d_{12} the distance between the source and detector pixel. To check if the code was working as intended some calculations were done for trivial situations that could easily checked by manual calculation. A perfect detector was assumed and the total energy deposited in a pixel was calculated using integration:

$$E_{dep} = A \int_{E=0}^{E_{max}} (\Phi_E)_{det} \, E dE = A \int_{E=0}^{E_{max}} (\Psi_E)_{det} \, dE \tag{4.18}$$

where A is the pixel surface. The good news was that after some corrections the algorithm was producing accurate results. The bad news was that the integration over all energies for took a considerable amount of time compared to the ray tracing. Some improvements could be made, but in the end it was clear that this part would be the most time intensive. This is also why further optimization of the ray tracing algorithm would not result in a significant decrease in computation time.

X-ray scattering

Until now the effect of scattering has been ignored, its only contribution being due to the fact part of the total attenuation is a result of X-rays undergoing scattering interactions. After they have interacted they have been assumed to disappear entirely. This results in an image in which details are much more visible as scattered X-rays generally reduce visibility due to them superimposing themselves on the direct image. This means that to get an accurate idea of the feasibility of radiography of SC fluids scattering has to be taken into account. This is however much more complicated and computationally intensive compared to transmission calculations. At the beginning of the chapter it was already mentioned that deterministic models are much less suitable for these kind of calculations. Theoretically there are an infinite number of paths an X-ray can take to reach the detector, although they become less and less probable as the number of interactions required and path length increases. These paths can be described as nth order scatterings. In a first-order scattering an X-ray scatters once after which it is either absorbed in a second interaction or reaches the detector, while in a second-order scattering it scatters at least twice. This can then be extended towards infinity. A complete deterministic model would have to calculate the contribution of all of these possibilities. It does not need saying that such an approach would be impractical. Fortunately most of these path have such a low probability that they can be ignored and only looking at low-order contributions provides results that are accurate enough, although in many cases even calculation of second-order scatter contribution is not achievable within reasonable time frames.

To calculate the contribution of scatter to the total measured intensity inspiration was taken from Freud et al. [34] who developed a deterministic method to simulate first-order scattering in voxelated samples. To do so they made use of the FF and ISF approximations discussed in section 2.1.2 which will be repeated here:

$$\frac{d\sigma_{Ra}}{d\Omega} = \frac{r_e^2}{2}(1+\cos^2\theta)[F(q,Z)]^2 = \frac{d\sigma_{Th}}{d\Omega}[F(q,Z)]^2 \tag{4.19}$$

and

$$\frac{d\sigma_{Co}}{d\Omega} = \frac{r_e^2}{2}\left(\frac{E'}{E}\right)^2\left(\frac{E'}{E}+\frac{E}{E'}-\sin^2\theta\right)S(q,Z) = \frac{d\sigma_{KN}}{d\Omega}S(q,Z) \tag{4.20}$$

The magnitude of momentum transfer q can be calculated using

$$q = \frac{2E}{c}\sin\left(\frac{\theta}{2}\right) \tag{4.21}$$

although in literature such as [33] the variable x is often used instead. Its relation to q is given by

$$x = \frac{q}{2h} = \frac{\sin\left(\frac{\theta}{2}\right)}{\lambda} \tag{4.22}$$

where h is the Planck constant and λ the photon wavelength. They also discuss the validity of these approximations, discussing the situations in which they are less accurate or break down all together, but the final conclusion is that these approximations still produce accurate results. See the paper for a more detailed discussion of the approximations and their validity.

In their model scattering is simulated by considering each voxel in the sample as a new X-ray source. This source then re-emits incoming X-rays with a certain angular distribution. This is visualized in figure 4.9 where 4.9(a) gives a complete view and 4.9(b) zooms in on the individual voxel. X-rays emitted from point S are incident on the center of mass of the voxel, point A. The size of the voxel is assumed to be much smaller than the distance between SA so the beam arriving at A can be assumed to consist of quasi-parallel rays. In the voxel centered around A the X-rays scatter in all directions, with a fraction in the direction of the pixel centered around point P, corresponding to the infinitesimal solid angle $d\Omega$. The total number of X-rays scattered towards pixel P is the product of the number of X-rays incident on voxel A $dN_i(E)$ and the probability of scattering into $d\Omega\, dp$:

$$d^2N_s = dN_i\, dp \tag{4.23}$$

with

$$dp = \frac{dN_{at}d\sigma_{at}}{dSd\Omega}d\Omega \tag{4.24}$$

Here dN_{at} is the number of atoms in the voxel, $\frac{d\sigma_{at}}{d\Omega}$ the atomic DCS corresponding to scattering into $d\Omega$ and dS the cross section area of the incoming beam. Since dp is equal to the total area of the target atoms divided by the cross section area of the beam the equation can be rewritten as

$$d_s^2\left(E'\right) = \Phi(E)\, dN_{at}\frac{d\sigma_{at}}{d\Omega}d\Omega \tag{4.25}$$

where E' is the energy of the scattered X-ray. Provided the voxel dimensions remain small this calculation does not depend on the voxel shape but only on the number of atoms within.
Using this approach the total number of X-rays scattered of a voxel towards a pixel can be calculated by carrying out the following calculations

1 The number of X-rays incident on the voxel is calculated by ray casting between point S and A and using equation 4.17:

$$(\Phi_E)_A = \frac{(\Phi_E)_0}{SA^2}e^{-\sum_m^{m=n}\mu_{\rho,m}(E)l_m\rho(i_m,j_m,k_m)} \tag{4.26}$$

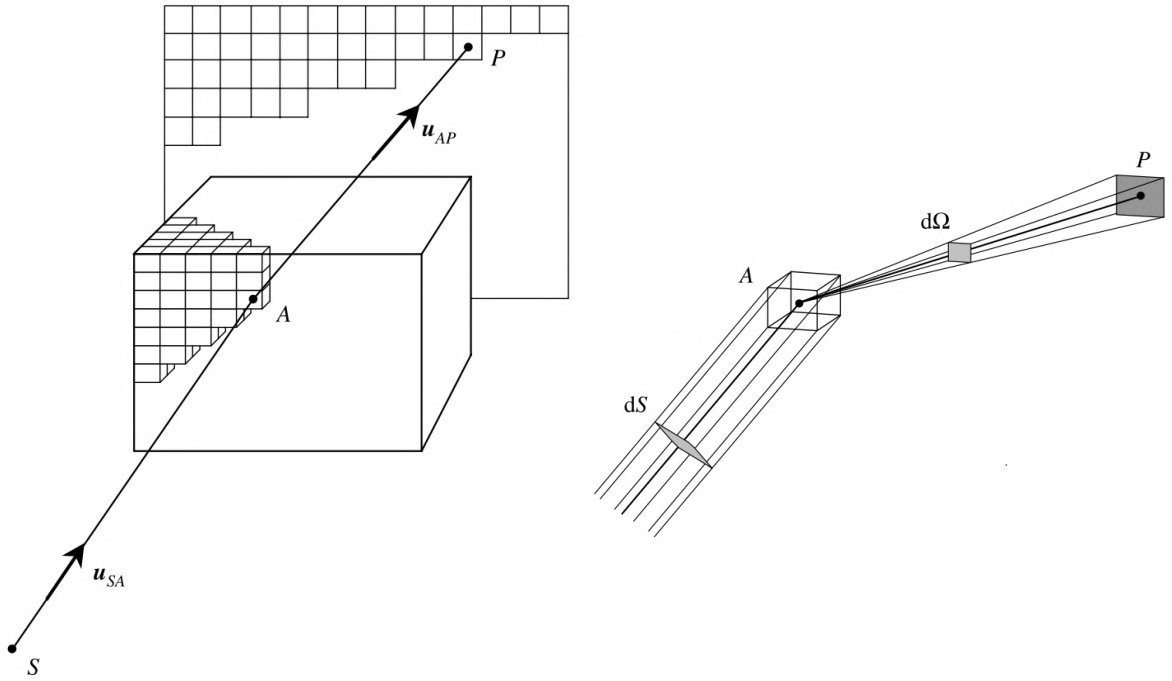

(a) Simulation of first-order scattering. Rays are cast from the source point towards each voxel of the object, then from each active voxel towards every pixel of the detector [34].

(b) Photon scattering off a volume element [34].

Figure 4.9: Visualization of X-rays scattering from a voxel towards a pixel element.

2 The cosine of the scattering angle is equal to

$$\cos(\theta) = \mathbf{u}_{SA} \cdot \mathbf{u}_{AP} = \frac{\mathbf{SA} \cdot \mathbf{AP}}{|\mathbf{SA}||\mathbf{PA}|} \tag{4.27}$$

Here $\mathbf{u}_{SA}$ and $\mathbf{u}_{AP}$ are the unit vectors of the incident and scattered rays as seen as in figure 4.9(a).

3 The solid angle corresponding to the pixel with center P as seen from the voxel is given by

$$d\Omega_p = \frac{dS_p}{AP^2} \cos(\mathbf{PA}, \mathbf{n}) \tag{4.28}$$

where dS_p is the pixel area and $\mathbf{n}$ the surface normal vector.

4 The momentum transfer is calculated using equation 4.22.

5 The coherent and incoherent scattering DCSs are calculated using equations 4.19 and 4.20. The FF and ISF values are obtained by interpolation of the tabulations of Hubbell et al. [33]. For compounds and mixtures the additivity rule is uses:

$$[F(x)]^2 = \sum_i \alpha_i [F(x, Z_i)]^2 \tag{4.29}$$

$$S(x) = \sum_i \alpha_i S(x, Z_i) \tag{4.30}$$

where α_i is the percentage of atoms with atomic number Z_i in the voxel.

6 The number of X-rays that scatter coherently towards P is then given by

$$d^2 N_{Ra}(E) = (\Phi_E)_A \, dN_{at} \frac{d\sigma_{Ra}}{d\Omega} e^{-\sum_m^{m=n} \mu_{\rho,m}(E) l_m \rho(i_m, j_m, k_m)} d\Omega_P \tag{4.31}$$

The exponent here is the result of ray tracing from point A to P. dN_{at}, the number of atoms in the voxel, is calculated using

$$dN_{at} = \frac{\rho dV}{\sum_i \alpha_i M_i} N_A \tag{4.32}$$

with dV the voxel volume, M_i the atomic molar mass of the ith element in the voxel and N_A Avogadro's constant.

7 The number of incoherent scattered X-rays is calculated similarly:

$$d^2N_{Co}(E_{Co}) = (\Phi_E)_A \, dN_{at} \frac{d\sigma_{Co}}{d\Omega} e^{-\sum_m^{m=n} \mu_{\rho,m}(E_{Co}) l_m \rho(i_m,j_m,k_m)} d\Omega_P \tag{4.33}$$

where E_{Co} is the energy of the X-rays after scattering, calculated using equation 2.14.

8 Finally the total energy incident on pixel P can be calculated using

$$E_P = \int_E d^2N_{Ra}(E)\, E dE + \int_{E_{Co}} d^2N_{Co}(E_{Co})\, E_{Co} dE_{Co} \tag{4.34}$$

Freud et al. [34] compared the results of their simulation of scatter from a single voxel with theoretical models of scattering and found that the spatial distribution and number of scattered X-rays were in good agreement with those models. They further investigated the effect of the voxel size on the results by simulating scatter of a iron plate close to a detector. They found that voxels with size 1 mm or smaller in combination with a detector with a 200 µm pixel pitch produce near identical results. They also studied the effect of pixel pitch size as the angular step from pixel to pixel should be small enough to correctly sample the DCSs. Pixel pitches of 200 µm were compared to pitches of 2 mm. From the results they concluded that the condition that pixel pitch should be small enough to ensure correct sampling of the DCSs presents some tolerance, but it is still advised to check the stability of the results. The final test was performed using a step wedge as scattering object with 1, 2 and 5 mm cubic voxels. These results showed that increasing the size from 1 to 2 mm did not result in significant loss of accuracy, but with 5 mm visible artifacts started to appear. The results did remain satisfactory however. Finally they compared their results with results calculated with the Geant4 Monte Carlo code and found them to be in excellent accordance. Based on their findings they established three criteria that should be followed to ensure accurate results:

- In order to justify considering each voxel as a scattering point incoming X-rays should be weakly attenuated in the voxel. As a result the voxel size can not be too large.
- The voxel size should not be much larger than the pixel size as this could introduce artificial artifacts in the final image.
- The size of the pixel should be small enough to ensure correct sampling of the DCSs, although results showed that this is not a very stringent condition.

Calculating the scatter from a single voxel is in essence doing two transmission calculations with some additional calculations in between. For a sample consisting of N voxels these calculations then have to be repeated N times for each pixel element in the detector. Since voxel dimension need to be small in order for the results to be accurate the total number of voxels in a sample is generally high, which means the total number of calculations necessary to determine the scatter contribution is much higher than that of the transmission. Furthermore, this is only for the first-order scattered X-rays. Determining the contribution of second-order X-rays would require calculation of the scatter from a voxel A to a voxel B and then to pixel P. The total number of calculations required for each pixel element would as a result increase to N^2. As an example the total number of calculations required for a sample consisting of 100 by 100 by 100 voxels and a detector with the same number of pixels as the Xineos-3131 would be almost equal to 2.4 trillion (10^{12}) for first-order scattering. For second-order scattering this increases to approximately 2.4 quintillion (10^{18}). It is clear that without exceptionally heavy computing power these kinds of calculations are impossible and even then it is likely that higher than first-order scattering will take too much time. Like Freud et al. [34] the decision was therefore made to limit scattering to a first-order approximation.

4.3. Detector

In section 3.1.2 the detectors used in the X-ray facility along with some of their specifications were discussed. In modelling a detector the most important part is the conversion from incoming X-rays to the output signal. In a ideal situation the manufacturer of the detector is able to provide a response function R that can be used for this purpose. In section 2.1.3 it was explained that the output of a scintillation detector

is proportional to the energy of the detected X-ray. In its simplest form R would be an energy-dependent function that is used to integrate the energy fluence incident on a pixel to calculate the output signal:

$$I = \int \Psi_E(E) R(E) A dE \tag{4.35}$$

where I is the output signal in ADUs and A the pixel surface. Unfortunately such functions generally do not exist or are not made available. This means that if a response function of a detector is required one needs to model this themselves. In order to do this all steps from X-ray interaction in the scintillation crystal to the final conversion to ADU need to be taken into account. In section 2.1.3 a brief explanation of this process was given. It will now be discussed in more detail with an emphasis on CsI scintillator detectors.

4.3.1. Detection process

The first step is the attenuation of X-rays in the detector. CsI is very susceptible to moisture damage, so the detector is encased in a protective layer. This layer is generally thin and made of low density material and only a small fraction of the incoming X-rays are attenuated here. After passing through the protective layer the X-rays enter the scintillation crystal. In ideal circumstances all X-rays would be absorbed here. In the crystal the X-rays interact with the material, transferring energy to the atoms and exciting or ionising them. A photoelectron that is elevated to the conduction band migrates through the crystal lattice until its finds a site where it can de-excite and return to the valence band by emission of a scintillation photon. In pure crystals this process is inefficient and slow due to the existence of the band gap between the conduction band and valence band. Furthermore, the scintillation photons that are produced are usually too high in energy. To increase the efficiency and speed of this process the crystals are commonly doped with small amounts of impurities. These impurities are called activators and create sites in the crystal lattice where the band structure is modified. As a result energy states that lie within the band gap become available for electrons to de-excite through back to the valence band. The energy difference between the activator conduction and valence band is less than that full band gap size resulting in scintillation photons with a lower energy. An illustration of this process is shown in figure 4.10. A common activator for CsI is thallium and the resulting scintillators are referred to as CsI:Tl scintillators. CsI:Tl has two characteristic decay times, which is defined as the time between excitation and de-excitation. These are 0.68 µs and 3.34 µs and are responsible for 64% and 36% of photon production respectively [67].

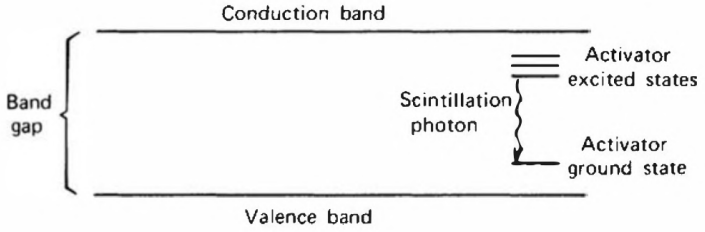

Figure 4.10: Energy band structure of an activated crystalline scintillator [67].

In the activated crystal interaction with an X-rays results in the creation of a electron-hole pair. Because the ionisation energy of the activator sites is less than that of the regular sites the hole will swiftly drift to the activator and ionise it. In the mean time the electron migrates through the crystal until it comes across such an ionised activator after which they together form a neutral, excited configuration. If the kinetic energy of the photoelectron is high enough it can create secondary electron-hole pairs while migrating through the crystal, which then can cause further ionisations. As a result the total number of scintillation photons produced per X-ray is dependent on its energy. Although for X-ray imaging this dependence is not of great importance, for spectral measurements it would ideally be proportional to the deposited energy. Unfortunately all scintillators show a certain degree of non-proportionality, with some being nearly proportional and others showing large deviations. For CsI:Tl some authors such as Knoll [67] assume proportionality, estimating the light yield to be 65 photons/keV. In a review by Dorenbos et al. [68], in which the absolute photon yield of various scintillators is presented, a scintillation response curve of CsI:Tl is shown, normalized at 662 keV. This curve shows that the photon yield at energies between 10 and 100 keV can be between 10 to 15% higher than the yield at

662 keV, which is stated to be 65 photons/keV. A study by Syntfeld-Każuch et al. [69] found comparable numbers. The deviation from proportionality can be partially explained by the fluorescence escape phenomenon. If the energy of incoming X-rays exceeds the energy required to excite electrons from their shell it is possible for the resulting characteristic X-ray that is emitted during de-excitation to escape the detector. The energy of these X-rays lies just below the absorption edge of the shell the electron from which they were emitted de-excited to, explaining the relatively high probability of escaping from the scintillator. The main contributors to this effect are the K- and L-shell, resulting in drops in light yield near the corresponding absorption edges.

In order to increase output quality as many scintillation photons as possible need to be detected. As the photons are emitted isotropically they need to be guided towards the detector. A method that is commonly used to increase the absolute light output is the placement of a thin reflector on top of the scintillator. Almost all photons that are emitted towards the top are reflected and directed back into the crystal, while X-rays can still easily pass through this thin layer. A major drawback is that this will increase the spatial spread of the photons which is already present due to the isotropic emission, resulting in increased blur in the image. A significant advantage of CsI which was also mentioned in section 2.1.3 is that in can be grown in columns. These columns act as fiber-optic light guides where total internal reflection keeps most of the photons in the column where they originated. This significantly reduces blur in the image.

The scintillation photons are detected by the active matrix array, consisting of a large number of pixels. These pixels consist of a sensing element and a switching device to register the signal. For the detector in question the sensing elements are photodiodes made of monolithic crystalline silicon, which is a semiconducting material. Incoming photons eject electrons from their shells due to the photoelectric effect. A current is created leading to the electrons being stored on the sides of the photodiode, which acts as a capacitor. After a certain period the CMOS is used to connect the photodiode to the surrounding circuitry resulting in the collected charge being transferred to a charge amplifier which produces an output voltage that is converted to ADUs.

4.3.2. Detector model

Attempts to characterize flat panel detectors have been made in the past with some examples being studies by Cao et al. [51], Endrizzi et al. [70], Jain et al. [71], Kördel [72]. Although these models differ in complexity, method and objective they share some characteristics: they require empirical data to fit the models to in order to find the parameters used in the analytical models and/or use estimations for certain properties. The reason for this is twofold. Firstly, manufacturers are generally restrictive in releasing technical data concerning their detectors, for example the thickness of the scintillator crystal. This means that these properties have to be estimated or determined experimentally. Examples of this are the absorption of X-rays in the scintillator and the point spread function (PSF) which is the response of the detector to a point source and introduces blur in the image. Secondly there are effects that are very hard or impossible to model due to them varying between detector to detector and even between pixel to pixel. These effects mostly themselves as noise in the final image. They can be divided into two categories: fixed-pattern noise (FPN) and temporal noise (TN).

FPN is a spatial noise and is the result of non-uniformity of the pixel response which means that two pixels produce a different output with the same input. This effect may stem from inhomogeneities in the photon conversion yield, losses in charge transport, charge trapping or variations in the performance of the readout, but can also be caused by damage, impurities in materials or small manufacturing errors. This noise has two components: dark signal non-uniformity (DSNU) and photo response non-uniformity (PRNU). DSNU is a form of dark signal noise. This type of noise is due to the fact that even when there are no photons impinging on the detector there is a non-zero signal output. It can be further subdivided into thermal noise and dark current noise [73]. Thermal noise is the result of random thermal excitations of electrons in electrical conductors. Dark current noise is caused by the current that is present even when there is no light incident on a photodiode. This current, known as dark current or reverse saturation current, is the result of minority carriers diffusing to the depletion region in the photodiode. These carriers are produced by thermally generated electron-hole pairs which means the dark current and therefore the dark current noise are strongly dependent on temperature. This leads to the overall dark signal noise also having a strong temperature dependence.

PRNU describes the non-uniform output of the detector when it is uniformly illuminated. Pixels that show this behaviour and produce anomalous values are called bad pixels. Celestre et al. [74] group these pixels based on their behaviour into one of four categories:

- **Linear pixels with false bias**: the output of these pixels is linear with respect to illumination intensity

or exposure time, but show a very low or high bias compared to their neighbours.

- **Nonlinear pixels**: the output of these pixels changes non-linearly with illumination intensity or exposure time.
- **Dead pixels**: these pixels show a very low or zero sensitivity to illumination, resulting in very low output values.
- **Hot pixels**: in contrast to dead pixels these are overly sensitive to illumination and result in very high or oversaturated output values.

These pixels occur either isolated, in clusters or as rows/columns. Fortunately FPN can be suppressed by flat-field correction (FFC). In its simplest form FFC uses two images made with uniform exposure: one with no illumination (dark field) and one that is uniformly illuminated such that it is close to saturation (flat field). By subtracting the dark image from the actual image and then dividing it by the normalized difference between the flat field and dark field the FPN can be effectively suppressed.

In contrast to fixed-pattern noise which causes the output of pixels to be non-uniform, temporal noise causes the output of a pixel to be non-constant in time. This noise is random and is the result of several underlying phenomena. The first contributor to TN is photon shot noise, which is the result of the particle nature of light and that photon measurement obeys Poisson statistics, and is largely independent of the detector. Effectively this means that the number of photons detected varies in time with a standard deviation equal to the root of the mean number of photons detected. Besides spatial noise the earlier mentioned dark signal noise also contributes to the TN. This contribution is called dark shot noise and fluctuates in time due to both the excitation of electrons and generation of minority carriers being random events. Another contributor to temporal noise is the readout noise. As mentioned earlier the incoming scintillation photons are converted to a voltage which is then converted to ADUs. Fluctuations in this voltage cause deviations in the final number of ADUs. The conversion from voltage to ADUs also introduces noise due to quantization errors. The total effective temporal noise can be calculated from the quadrature sum of each of the noise sources:

$$\sigma_{eff}^2 = \sqrt{\sum_i \sigma_i^2} \tag{4.36}$$

Unfortunately due to its stochastic nature TN can not be easily corrected for after an image has been made unlike FPN. The primary method of reducing the influence of TN is to increase exposure time and/or illumination intensity. This is because the noise sources either are independent of the output signal or increase as its square root which means the SNR increases with output intensity. Another way to decrease noise is by taking the average of multiple images. In medical imaging the main problem with these methods is that it increases the absorbed dose in a patient. While absorbed dose is generally not a problem in non-medical applications longer exposure or averaging can be problematic when studying a dynamic system with short timescales as this can cause details and information to be lost.

In the end three aspects of the detector response that were estimated to have the largest influence on the output were identified. These were the energy response function, the point spread function and the total image noise.

Energy response function

The first step in modeling the energy response function is to calculate the energy that is deposited in the scintillator by incoming X-rays. As detector characterization is a subject that has been extensively studied in the past multiple methods have been developed. After study of the relevant literature three models were selected that could be used to calculate the response. The first model was used by Kördel [72]. Although their objective was to develop an analytical model of the point spread function of a CsI detector rather than the energy response function their approach is still valid. According to their model describing the PSF the energy response function is:

$$I = \int_E \chi(E)\,dE \int_0^\tau E\mu_{PE}(E)e^{-\frac{\mu_{tot}(E)z}{\cos\theta}}\,(a_0 + a_1 E)\,dz \tag{4.37}$$

Here I is the pixel output in ADUs, $\chi(E)$ the energy spectrum of the X-rays incident on a pixel, τ the scintillator thickness, E the energy of said X-rays, $\mu_{PE}(E)e^{-\frac{\mu_{tot}(E)z}{\cos\theta}}$ the probability of photoelectric interaction at depth z in the scintillator for X-rays incident with an angle θ with respect to the pixel surface normal and $(a_0 + a_1 E)$

the energy dependent gain of the system. This model makes use of three assumptions regarding the X-ray energy transfer and creation of scintillation photons. The first assumption is that scintillation photons are only created by the photoelectric effect, in other words energy transfer due to scattering is neglected. The motivation given for this approximation is that at the energies relevant to X-ray imaging the photoelectric effect dominates over the other interactions. Looking at figure 4.11(a) it is easy to see that this is a reasonable assumption as up to 100 keV $\mu_{\rho,PE}$ is essentially equal to $\mu_{\rho,tot}$. The second assumption made is that all energy transferred to the detector is used to produce scintillation photons and no energy is lost due to fluorescence escape or other mechanisms. Up until 30 keV this can be reasonably be assumed, but at higher energies the energy loss can become quite considerable. The final assumption is the proportionality of the scintillation yield with respect to energy, an assumption adopted from Knoll [67]. Although this is not true the deviation from proportionality in the relevant energy range is small enough the be disregarded. Finally they assume that the depth at which scintillation photons are created has no influence on the output signal. This is true if there is no or little absorption of scintillation photons in the scintillator. They state that this is not an unreasonable assumption since scintillator materials are selected based on their absolute light output and transparency is therefore an important property of scintillator materials.

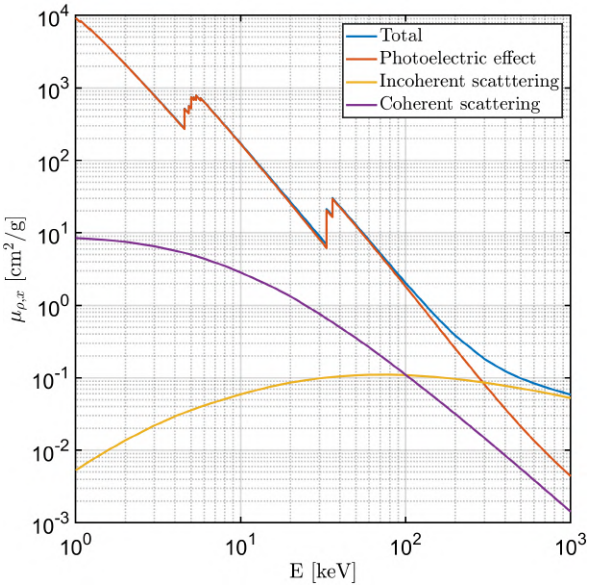

(a) Total and partial mass attenuation coefficients. Values taken from the XCOM database [32].

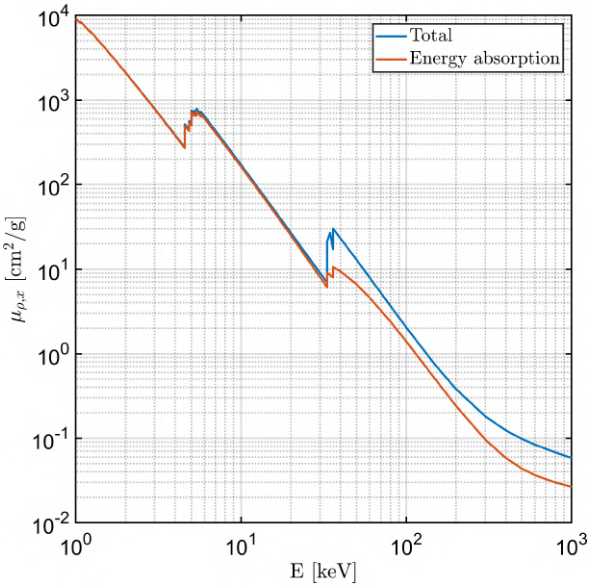

(b) The total mass attenuation and energy-absorption coefficient. Values taken from the XAAMDI database [75].

Figure 4.11: Mass attenuation and energy-absorption coefficients of CsI.

The second model was developed by Endrizzi et al. [70] and is fairly similar to the function given in equation 4.37:

$$I = a \int_0^\infty \chi(E)\, e^{-\mu_{PL}(E)\Delta} \left(\frac{\mu_{en}(E)}{\mu(E)}\right) E\left(1 - e^{-\mu(E)\tau}\right) dE \tag{4.38}$$

Here a is a coefficient that is used to convert energy to ADUs, $\mu_{PL}(E)$ the linear attenuation coefficient of the protective layer with thickness Δ, $(1 - e^{-\mu(E)\tau})$ the probability of interacting in the scintillator with thickness τ and $\mu_{en}(E)$ the energy-absorption coefficient of the scintillator. Similarly to Kördel [72] they assume a proportional relationship between the X-ray energy and the number of produced scintillation photons and the depth-independence of the output signal on the interaction depth. The first difference between the models is that Endrizzi et al. [70] assume that all other processes aside from the creation of scintillation photons such as photon transport, quantum efficiency and the signal shaping are independent from the X-ray energy. The effect of these processes can thus be modelled using the coefficient a in equation 4.38. Another difference is that they take the protective layer on top of the scintillator into account. The additional attenuation of this layer is likely to have little effect on the output since these layers are designed to be as transparent as possible to X-rays and in most cases is negligible compared to the attenuation due to an object between the X-ray source and the detector. In addition it is assumed the X-rays have a normal incidence on the pixels.

The final difference is the method used to calculate the energy transferred to the scintillator through interactions. As mentioned above Kördel [72] assume all interactions in the scintillator are through the photoelectric effect and that no energy is lost. Endrizzi et al. [70] instead use the energy-absorption coefficient to calculate the transfer of energy. The mass energy-absorption coefficient for CsI is plotted in figure 4.11(b) together with the mass attenuation coefficient. These values were taken from the XAAMDI database which is also provided by NIST. Although technically a separate database from XCOM it is based on the same theoretical calculations and in practice is also referred to as the XCOM database. The mass-absorption coefficient is a measure of the average fractional amount of incident X-ray energy transferred to kinetic energy of charged particles as a result of interactions in a medium [76]. Furthermore it takes into account that kinetic energy is lost due to the production of bremsstrahlung as the charged particles slow down in the medium and due to fluorescence escape. Looking at figure 4.11(b) it can be seen that up to 30 keV $\mu_{\rho,en}$ is almost equal to μ_ρ and indeed almost all X-ray energy is transferred to the scintillator during an interaction. As the energy increases however there is a sharp increase in the value of the coefficients, but the increase of $\mu_{\rho,en}$ is noticeably smaller. This is a result of the X-ray energy becoming higher than the binding energy of the K-shells in Cs (35.99 keV) and I (33.17 keV) [72], making excitation of electrons in these shells and the subsequent escape of characteristic X-rays due to k-fluorescence escape possible.

To see the impact of this energy loss different parts of equation 4.38 are plotted in figure 4.12. Figure 4.12(a) shows the ratio $\frac{\mu_{en}(E)}{\mu(E)}$ which is the fraction of X-ray energy absorbed by the scintillator per interaction. At energies just above the K-shell absorption edges the fraction of absorbed energy is very low compared to other energies. In figure 4.12(b) the quantum detection efficiency (QDE) of a CsI scintillator of various thicknesses is plotted. The QDE is equal to $(1 - e^{-\mu(E)\tau})$ and is the fraction of incoming X-rays that are attenuated in the scintillator [77]. At very low energies essentially all X-rays are attenuated after which there is a sharp drop in efficiency. The moment the X-ray energy becomes larger than the K absorption energy edge the efficiency increases again, after which it only decreases with increasing energy. As the detector is not a photon counter but an energy integrator it is more useful to look at the energy absorption efficiency (EAE). This quantity can be calculated by multiplying the QDE with the energy absorption fraction and can be considered the average fraction of energy that an X-ray transfers to the scintillator it is incident on. It can be seen in figure 4.12(c). At low energies aside from the thinnest scintillator the EAE follows the absorption fraction reasonably well, but as the energy increases the QDE drops rapidly, causing the EAE to drop as well. Multiplying the EAE with the X-ray energy then gives the average absorbed energy (AAE) of an incoming X-ray with energy E and is presented in figure 4.12(d). Even though X-rays in the high energy part of the spectrum can transfer more energy to the detector during an interaction the low efficiency at these energies results in them being only minor contributors to the total absorbed energy compared to X-rays in the middle of the spectrum. Looking at these figures it is clear that depending on the X-ray spectrum used the assumption that all X-ray energy of attenuated X-rays is absorbed by the scintillator can introduce a significant error in the results.

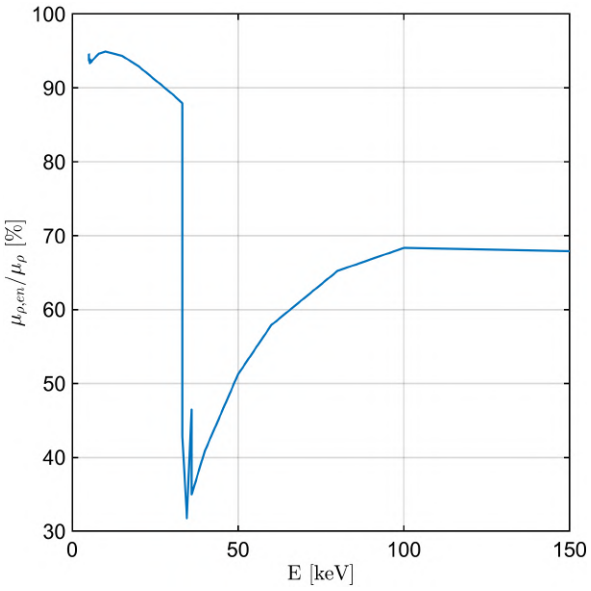

(a) Fraction of energy absorbed by a CsI scintillator per interaction as function of X-ray energy.

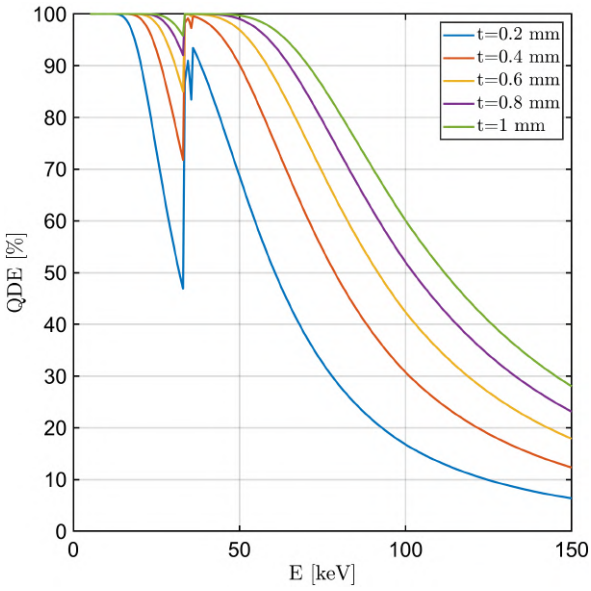

(b) QDE of a CsI scintillator as function of X-ray energy for various scintillator thicknesses.

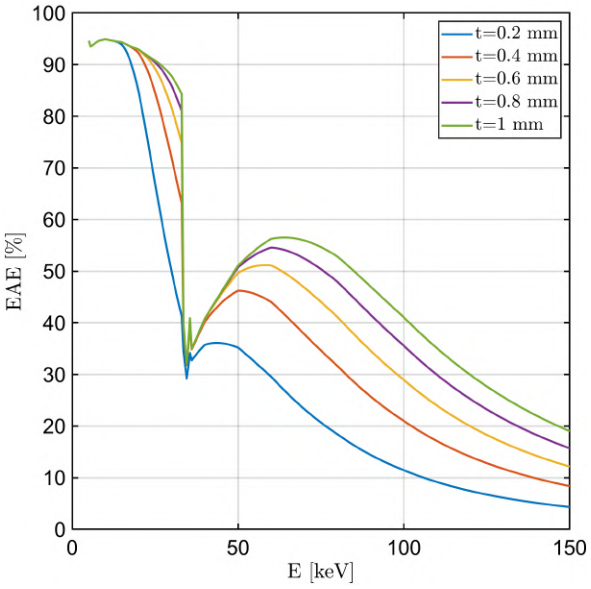

(c) EAE of a CsI scintillator as function of X-ray energy for various scintillator thicknesses.

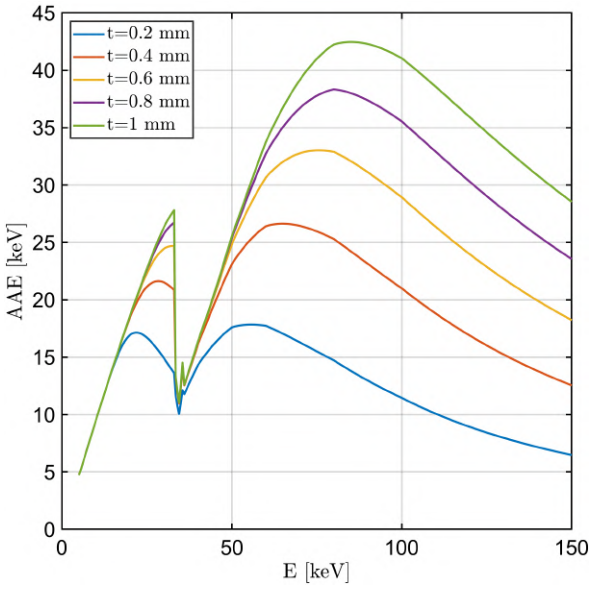

(d) AAE of a CsI scintillator as function of X-ray energy for various scintillator thicknesses.

Figure 4.12: Absorption efficiencies and averages of CsI scintillators with varying thicknesses.

While it is clear that the energy absorption is more accurately modelled by Endrizzi et al. [70] it there is still an aspect missing. With their model they assume that all characteristic X-rays escape the scintillator and none are re-absorbed. While they are relatively likely to escape looking at the QDE in figure 4.12(b) they still have a high probability of interacting in the scintillator. Studies regarding this phenomenon [78–80] indeed came to the conclusion the re-absorption these X-rays can have a considerable influence on the output signal. The third method is the one used by Cao et al. [51],which they used in their study to model and evaluate a CMOS detector, and does take the re-absorption into account. To this purpose they developed a cascaded systems model using parallel cascades, a method first proposed by Yao and Cunningham [80]. The parallel part of this system refers to the procedure of calculating the quantum gain; the number of scintillation photons created per incoming X-ray. Three pathways are considered: A, B and C. Path A (4.39a) describes the creation of scintillation photons without the emission of a K X-ray, while in path B (4.39b) scintillation photons are created alongside the emission of an K X-ray which then might be re-absorbed at another location. This is what happens in path C (4.39c), where scintillation photons are created as the result of K X-ray re-absorption. Equation 4.39 shows how the mean quantum gain of each path is calculated.

$$\overline{g_{2A}}(t_{CsI}) = \frac{\int_0^{E_{\max}} q_{det}(E) \int_0^{t_{CsI}} g_1(E,z)\eta_{esc}(t_{CsI},z)(1-\xi\omega)EWdzdE}{\int_0^{E_{\max}} q_{det}(E) g_1(E,t_{CsI})(1-\xi\omega)dE} \tag{4.39a}$$

$$\overline{g_{2B}}(t_{CsI}) = \frac{\int_0^{E_{\max}} q_{det}(E) \int_0^{t_{CsI}} g_1(E,z)\eta_{esc}(t_{CsI},z)\xi\omega(E-E_K)Wdzd E}{\int_0^{E_{\max}} q_{det}(E) g_1(E,t_{CsI})\xi\omega dE} \tag{4.39b}$$

$$\overline{g_{2C}}(t_{CsI}) = \frac{\int_0^{E_{\max}} q_{det}(E) \int_0^{t_{CsI}} g_1(E,z)\eta_{esc}(t_{CsI},z)\xi\omega f_K(t_{CsI})E_K Wdzd E}{\int_0^{E_{\max}} q_{det}(E) g_1(E,t_{CsI})\xi\omega dE} \tag{4.39c}$$

Here $qdet$ is the X-ray spectrum at the detector surface, t_{CsI} the scintillator thickness and $g1(E,z)$ the QDE. $\eta_{esc}(t_{CsI},z)$ is the fraction of scintillation photons that reaches the photodiode which depends on both the scintillator thickness and the depth at which they are produced. This fraction and its dependence on scintillator design was studied by Howansky et al. [81] for CsI scintillators. Cao et al. [51] then used a linear fit to these results to calculate $\eta_{esc}(t_{CsI},z)$:

$$\eta_{esc}(t_{CsI},z) = 0.312 + 1.85(z - t_{CsI}) \tag{4.40}$$

with z and t_{CsI} in cm. $\xi\omega$ is the probability of a K X-ray being generated during an interaction and is the product of the probability of K-shell interaction ξ and fluorescent yield ω with f_K the K-fluorescence re-absorption factor which was calculated using an analytical model developed by Chan and Doi [78]. Finally W is the scintillation photon yield and E_K the energy of an K X-ray. The mean quantum gains of each path are then combined to construct the mean total gain:

$$\overline{g_2}(t_{CsI}) = (1-\xi\omega)\overline{g_{2A}}(t_{CsI}) + \xi\omega\overline{g_{2B}}(t_{CsI}) + \xi\omega f_K\overline{g_{2C}}(t_{CsI}) \tag{4.41}$$

Multiplying the total mean gain with optical coupling efficiency $\overline{g_4}$, which is the conversion efficiency of scintillation photons the electrons, gives the mean number of electrons produced per incoming X-ray. Multiplication with the conversion gain factor k then gives the number of ADUs per incoming X-ray.

This approach requires the knowledge of many parameters which are as mentioned earlier very difficult to ascertain. This would mean that using this model might not be a smart decision if not for the fact the detectors used by Cao et al. [51] are a different model (Xineos-3030HR) from the same manufacturer as the detectors in the X-ray facility. Using the same values for the parameters might therefore not be a bad approximation. Furthermore, one of the detectors used was a specially developed custom detector so it can be safely assumed the authors were in close contact with the manufacturer and thus the values used in their model to be accurate.

In the end the decision was made to combine elements from the models into a new model. Like Cao et al. [51] a parallel system is used, but instead of three paths two are implemented. Path 1 describes the absorption of energy in the scintillator taking into account energy loss due to fluorescence escape and uses the approach of Endrizzi et al. [70]. This path is in effect a combination of paths A and B from Cao et al. [51]. Path 2 then describes the re-absorption of K X-rays and is essentially identical to equation 4.39c. Like Kördel [72] the effect of the protective layer on top of the scintillator is neglected. The primary reason for this is that the important properties such as thickness and material composition are unknown. It is however expected that

the influence on the final results will be minimal as the layer would only affect low energy X-rays which are almost completely attenuated by the object. The resulting equations for the two paths then take the following shape:

$$I_1 = \gamma g_c k A_{eff} \int_0^{E_{max}} \Phi_{E,pix}(E) \int_0^{t_{CsI}} \mu_{en}(E) e^{-\mu(E)z} \left(0.312 + 1.85\left(z - t_{CsI}\right)\right) E dz dE \tag{4.42a}$$

$$I_2 = \gamma g_c k A_{eff} \int_0^{E_{\max}} \Phi_{E,pix}(E) \int_0^{t_{CsI}} \mu(E) e^{-\mu(E)z} \left(0.312 + 1.85\left(z - t_{CsI}\right)\right) \xi \omega f_K\left(t_{CsI}\right) E_K dz dE \tag{4.42b}$$

where I is the intensity in ADUs, γ the scintillation photon yield per absorbed energy unit, g_c the optical coupling efficiency, k the conversion factor from electrons to ADUs and A_{eff} the effective surface area of a pixel. $\mu(E)$ is the linear attenuation coefficient of CsI and can be rewritten as $\mu_\rho(E)\rho f_{CsI}$ where f is the packing fraction. Kördel [72] and Endrizzi et al. [70] both assume this fraction to be 1, while Cao et al. [51] use a packing fraction of 0.7 which was chosen empirically to yield better agreement with measurements. The total intensity is then calculated by summation of the two paths.

In theory these functions would allow the calculation of the output intensity without the need for calibration measurements to determine parameters. The results from these calculations are however only accurate if the values used in equation 4.42 are valid for the detector used. The detectors used in the study by Cao et al. [51], which is the main source for these values, are made by the same manufacturer but have different specifications from the model studied. For example their pixel pitch is 99 µm compared to the 198 µm of the 3131 model. If all constants in equation 4.42 would be the same for both models the intensity output of the 3131 model would be approximately four times higher under the same measurement conditions due to the larger pixel surface. Since both are expected to operate in similar conditions and both have a bit depth of 14 bits this would mean that the 3030HR model would only use a small portion of its possible resolution in most cases. One could make the assumption that to compensate for the smaller pixel surface the conversion factor k is four times higher for the 3030HR model compared to the 3131 model. A check to see if this assumption has any base in reality is to look at the saturation dose per frame, which is the dose measured at the surface of the detector at which the pixels are just saturated. As the absorbed dose has units J/kg or Gy the increase in surface area is compensated by the increase in volume. This means that if k is the same for both detectors the saturation dose of the 3131 model should be approximately four times smaller than that of the 3030HR model.

In normal operation the saturation dose is 23 µGy for the 3030HR model. The saturation dose for the 3131 detector is not specified in Gy but in roentgen (R). Luckily conversion from exposure to absorbed dose is simple as exposure is specifically a measure of air ionisation. According to the datasheet the saturation dose of the 3131 detector is 1 mR, which is approximately 9 µGy, just over 2.5 times smaller than that of the 3030HR detector. As a result k for the 3131 detector should be roughly 1.6 times smaller instead of four times. While it is possible to divide the value of k provided by Cao et al. [51] by 1.6 this seems rather arbitrary and could be seen as a step taken just to make sure the equations in 4.42 can still be used even though they might not be valid. It should be kept in mind that it is possible the two detectors are not intended to produce the same output in identical situations and that the 3131 model is designed to be more sensitive to lower intensities with both detectors having the same value for k. An option that might be more accurate is to match the saturation dose of the detector to the maximum pixel value of 2^{14}. The specifications provided by the manufacturer state that non-linearity is less than 1.5%, so it is a reasonable approximation to have the pixel intensity increase linearly with absorbed energy until the saturation dose has been reached. The first step is to calculate the saturation dose in the CsI itself. Unfortunately the conversion from R to Gy is much more complicated for materials other than air. This conversion requires the use of the f factor or the roentgen-to-rad conversion factor. In chapter 8.3 from the book by Khan and Gibbons [26] the f factor is calculated using the following equation:

$$f_{med} = 0.876 \frac{\left(\overline{\mu}_{\rho,en}\right)_{med}}{\left(\overline{\mu}_{\rho,en}\right)_{air}} \tag{4.43}$$

Here f_{med} is the f factor of a medium and $\overline{\mu}_{\rho,en}$ the mass energy-absorption coefficient averaged over the energy fluence spectrum. As calculation of the f factor requires averaging over the energy fluence spectrum the spectrum that was used to measure the saturation dose has to be used to get an accurate conversion factor.

Luckily there are international standards set by the International Electrotechnical Commission (IEC) regarding the beam quality of X-ray tubes which make reproduction of studies or investigating the performance of detectors possible. The specifications list of the 3131 model states that the values were determined using a RQA5 spectrum. Beams of this series represent simulations of the radiation field behind a patient. The parameters determining the quality are the X-ray tube voltage and added filtration, which for RQA5 are 70 kV and 21 mm Al respectively. The normalized energy fluence spectrum that is produced with these settings is shown in figure 4.13. The saturation dose in the CsI can then by calculated using:

$$D_{med} = f_{med} \cdot X \cdot A = f_{med} = 0.876 \frac{\left(\overline{\mu}_{\rho,en}\right)_{med}}{\left(\overline{\mu}_{\rho,en}\right)_{air}} \cdot X \cdot \frac{\Psi_{med}}{\Psi_{air}} \tag{4.44}$$

where D_{med} is the saturation dose, X the exposure and A the transmission factor that is the ratio between the total energy fluence in the medium Ψ_{med} and total energy fluence in the air Ψ_{air}

In order to find $\left(\overline{\mu}_{\rho,en}\right)_{med}$ and Ψ_{med} the average fluence spectrum in the CsI is needed. This is calculated by averaging over the attenuation through the CsI:

$$\left(\overline{\Psi}_E\right)_{CsI} = \frac{1}{t_{CsI}} \int_0^{t_{CsI}} (\Psi_E)_{air}\, e^{-\mu_\rho \rho z} dz = \frac{1}{\mu_\rho \rho\, t_{CsI}} (\Psi_E)_{air} \left(1 - e^{-\mu_\rho \rho\, t_{CsI}}\right) \tag{4.45}$$

The saturation dose in the CsI can then finally be calculated using

$$D_{CsI} = 0.876 \frac{\int \left(\mu_{\rho,en}\right)_{CsI} \left(\overline{\Psi}_E\right)_{CsI} dE}{\int \left(\mu_{\rho,en}\right)_{air} (\Psi_E)_{air}\, dE} \cdot X \tag{4.46}$$

Using the RQA5 beam quality parameters and equation 4.46 the saturation dose in CsI is found to be approximately 330 µGy. In the article by Cao et al. [51] it is mentioned that 700 µm scintillator thickness was the standard at the moment of writing, so it is likely the 3131 model has the same thickness. Using this thickness, a pixel surface of 198 µm^2 and assuming a packing fraction of 1 a pixel has to absorb just over 250 MeV of X-ray energy to saturate. Besides this method being possibly more accurate it has the secondary advantage that only the absorbed energy has to be calculated and the factors regarding the production, transport and conversion of scintillation photons can be neglected. The equations in 4.42 then simplify to

$$I_1 = \Gamma A_{eff} \int_0^{E_{max}} \Phi_{E,pix}(E) E \int_0^{t_{CsI}} \mu_{en}(E) e^{-\mu(E) z} dz dE \tag{4.47a}$$

$$= \Gamma A_{pix} \int_0^{E_{max}} \Phi_{E,pix}(E) E \left(\frac{\mu_{en}(E)}{\mu(E)}\right) \left(1 - e^{-\mu(E)\, t_{CsI}}\right) dE$$

$$I_2 = \Gamma A_{eff} \int_0^{E_{\max}} \Phi_{E,pix}(E) E_K \int_0^{t_{CsI}} \mu(E) e^{-\mu(E) z} \xi \omega f_K(t_{CsI})\, dz dE \tag{4.47b}$$

$$= \Gamma A_{pix} \int_0^{E_{\max}} \Phi_{E,pix}(E) E_K \left(1 - e^{-\mu(E)\, t_{CsI}}\right) \xi \omega f_K(t_{CsI})\, dE$$

where Γ is a conversion factor that converts absorbed energy to ADUs. Matching the saturation energy to the maximum pixel value gives $\Gamma = 6.47 \cdot 10^{-5}$ ADU/eV. This approach is similar to the method of Endrizzi et al. [70] who use a similar conversion factor, but in their case they determine this constant experimentally. The accuracy of this method can be checked by simulating one of the measurements mentioned in 3.2.1 and comparing the results. If no good agreement can be found between the calculated intensities and the measured ones a final option can be to follow the approach of Endrizzi et al. and find the conversion factor by matching the calculated absorbed energy with the measured intensities.

Spatial resolution

The spatial resolution of a detector determines how well small details are visualized in an image with low resolution introducing blur, leading to loss of details. The spatial resolution of a system is usually specified with its modulation transfer function (MTF) which is a function of spatial frequency, often expressed as line

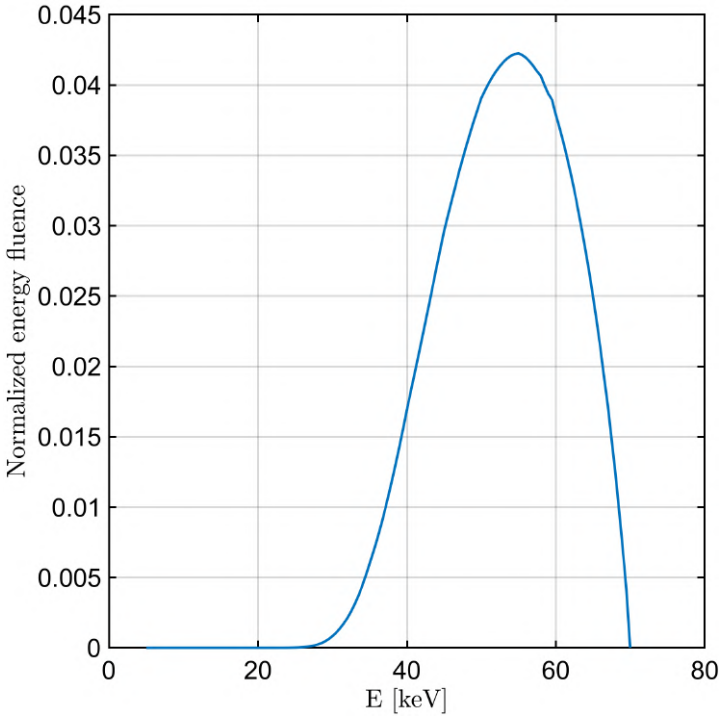

Figure 4.13: Normalized energy fluence spectrum produced with the parameters corresponding to RQA5 beam quality.

pairs per millimeter (lp/mm). Its value indicates the how much of the contrast of an object is captured in an image and usually decreases from 1 to 0 as spatial frequency increases. It is the Fourier transform of the line spread function (1D) or the point spread function (2D). Generally in detector modeling the MTF is a detector property that is not determined purely analytically, but determined either by measuring it experimentally and fitting a function to the results or by developing a parameterized model and finding the parameters empirically. The most common method is to measure the ESF (edge spread function) which can be differentiated to find the LSF (line spread function). If needed the MTF can then be calculated by Fourier transforming the LSF and taking the modulus.

Due to experimental work in the X-ray facility not being possible the MTF of the detector could not measured, with the need to do so also being invalidated if experiments could be done. As a result an estimation of the MTF has to be made. Unfortunately for the detector used in the X-ray facility the MTF is only specified at one spatial frequency number; 60% at 1 lp/mm using a RQA5 beam. This is insufficient information to derive a PSF from. Luckily for three other models (3030HR, 3030HS and 1511) more complete curves are provided by the manufacturer in their respective datasheets. Values of the MTF at multiple spatial frequencies were extracted from the figures in the datasheets and the resulting curves can be seen in figure 4.14(a). The MTF for both the 3030HR and 1511 model extend to 5 lp/mm, while it only extends to 3.3 lp/mm for the 3030HS model. This can be easily explained by looking at the pixel size of the detectors. The 3030HR and 1511 have a pixel pitch of 99 µm and the 3030 HS has a pixel pitch of 151.8 µm. Since the smallest line pair that can still be imaged is the size of two pixels the pixel size also places a limit on the spatial frequency. Taking twice the pixel pitch and converting it to spatial frequency indeed gives approximately 5 lp/mm for 99 µm and 3.3 lp/mm for 151.8 µm.

At low spatial frequencies the MTFs for the detectors are very similar up to 1 lp/mm and only at higher frequencies do the 99 µm pixel detectors start to deviate from the 151.8 µm pixel detector. The datasheets for other model detectors which only provide the MTF at 1 lp/mm all provide a similar value; approximately 60%. It is therefore likely that up to 1 lp/mm all detectors have the same MTF after which pixel size starts to become an influence. Out of the three detectors that have a complete MTF profile the 3030HS is the closest in pixel pitch size compared to the 3131: 151.8 µm versus 198 µm. It is therefore obvious that the corresponding MTF will be the most similar to MTF of the 3131 detector and it was decided to approximate the MTF of the 3131 detector with this curve. It should be kept in mind that due to the pixel size the MTF of the 3131 detector

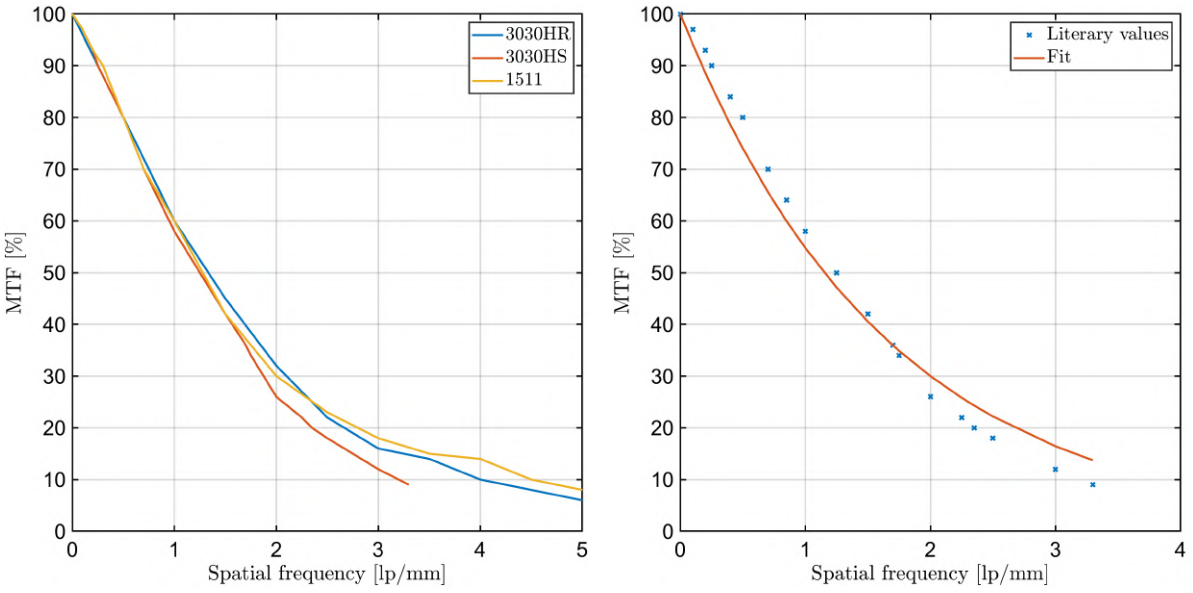

(a) MTFs of three Xineos flat panel detectors.

(b) MTF of the Xineos 3030HS flat panel detector and fit to the data.

Figure 4.14: MTFs of Xineos flat panel detectors and fit to one of the MTFs. The fit function has the form $T(u) = e^{-b \cdot u}$ with u the spatial frequency and b the fitting parameter, in this case equal to 0.6019.

can only extend to 2.5 lp/mm and is likely lower in value from 1 lp/mm and higher than the 3030HS. As a consequence using the 3030HS MTF results in a underestimation of the PSF.

The first step in finding the PSF of the detector is calculating the LSF. In order to do so a function has to be found describing the MTF which can then be Fourier transformed. A convenient function to fit to the curve is an exponential of the form $T(u) = e^{-b \cdot u}$ where b is a fitting parameter and u the spatial frequency. The results of the fit are plotted in figure 4.14(b) with $b = 0.6019$. Although other forms such as a Gaussian function result in better matching fits the choice to use a simple exponential function is one made out of convenience. The reason for this is that after the LSF is found by Fourier transformation of the MTF is still has to be converted to a PSF. The method to do so is described by among others Marchand [82] and Jones [83] assuming the PSF is point-symmetrical and even then requires complicated mathematics. Luckily MTFs described by an exponential function have been widely studied, including the conversion from MTF to PSF [83, 84]. Fourier transforming the MTF results in the following LSF:

$$L(x) = \mathscr{F}\{e^{-b \cdot u}\} = \frac{1}{\pi} \frac{b}{b^2 + x^2} \tag{4.48}$$

which is a Lorentzian function. This 1D function is then converted to a 2D PSF:

$$P(x, y) = \frac{b}{2\pi \left(b^2 + x^2 + y^2\right)^{\frac{3}{2}}} \tag{4.49}$$

As mentioned in section 4.1 a more time efficient method of modeling the image blur due to the finite source size is applying a filter that is dependent on the source focal spot size to the image. In order to find the total blur in the image the blur of the focal spot has to be combined with the blur introduced by the detector itself. This is done by multiplying the MTF of the focal spot T_{spot} with the MTF of the detector T_{det} to find the system MTF T_{sys}. This function is then used to find the LSF and the PSF. Cao et al. [51] use a simplified Gaussian model to describe the focal spot MTF:

$$T_{spot}(u, v) = e^{-\pi (M-1)^2 a_{spot}^2 (u^2 + v^2)} = e^{-2\pi \sigma_{spot}^2 (u^2 + v^2)} \tag{4.50}$$

where M is the system magnification, a_{spot}^2 the focal spot size and σ_{spot}^2 a replacement constant. A quick guess of the 2D detector MTF would be of the following form:

$$T_{det}(u, v) = e^{-\sigma_{det}^2 (u+v)} \tag{4.51}$$

where σ^2_{det} is equal to b in equation 4.48. Finding the system PSF is much more complicated compared to the detector PSF as the function describing $T_{sys} = T_{spot} \cdot T_{det}$ is not a standard function of which the PSF can easily be found. A better option might then be to make use of the convolution theorem, which states that taking the inverse Fourier transform of two point-wise multiplied functions is equal to convolution of the individually transformed functions. In one dimension this is described as:

$$h(x) = \{f * g\}(x) = \mathscr{F}^{-1}\{F \cdot G\} \tag{4.52}$$

Furthermore, the 2D convolution of two radially symmetric functions yields another radially symmetric function [85] Using this theorem the system PSF P_{sys} can be calculated by convolution of the detector PSF P_{det}, which is given in equation 4.49, with the focal spot PSF P_{spot}. P_{spot} is found by Fourier transformation of equation 4.50:

$$P_{spot}(x,y) = \mathscr{F}\{T_{spot}(u,v)\} = \frac{1}{2\pi\sigma^2_{spot}} e^{-\frac{x^2+y^2}{2\sigma^2_{spot}}} \tag{4.53}$$

Convolution of P_{spot} with P_{det} and subsequent normalization then gives P_{sys} of which a cross section along the x-axis is shown in figure 4.15(a) for $M = 1.24$ and $a_{spot} = 1$ mm. The full width at half maximum (FWHM) is 0.976 mm, approximately 5 pixels. Applying the system blur to an image would be easier if P_{sys} could be described with an analytical function. Since the shape of the PSF looks Gaussian two fits with Gaussian functions were made along the diagonal between the x- and y-axis. Due to radial symmetry this one-dimensional fit can be used to accurately recreate the two-dimensional total PSF. The first fit was made using a single Gaussian of the form $P_{fit}(r) = ae^{-\frac{r^2}{2\sigma^2}}$. A accurate fit using a single Gaussian would be very convenient as it would allow the use of MATLAB's built-in image filtering functions. Unfortunately, looking at figure 4.15(b) a fit using only a single term only matches the central part of the peak with a peak value that is slightly too low. The second fit was made using a double Gaussian of the form $P_{fit}(r) = a_1 e^{-\frac{r^2}{2\sigma_1^2}} + a_2 e^{-\frac{r^2}{2\sigma_2^2}}$. A fit using this form is much better at reproducing the total curve as is clear from looking at figure 4.15(b). This is similar to the results of Endrizzi et al. [70] who also found a double Gaussian function to best reproduce the LSF they measured. The values of the fitted parameters are shown in table 4.1. Unfortunately MATLAB has no predefined functions to apply a filter of this form to an image, so this has to be done manually. An option is to change the dependence of the PSF on the distance in mm to pixel numbers and then convolution of the image with this function.

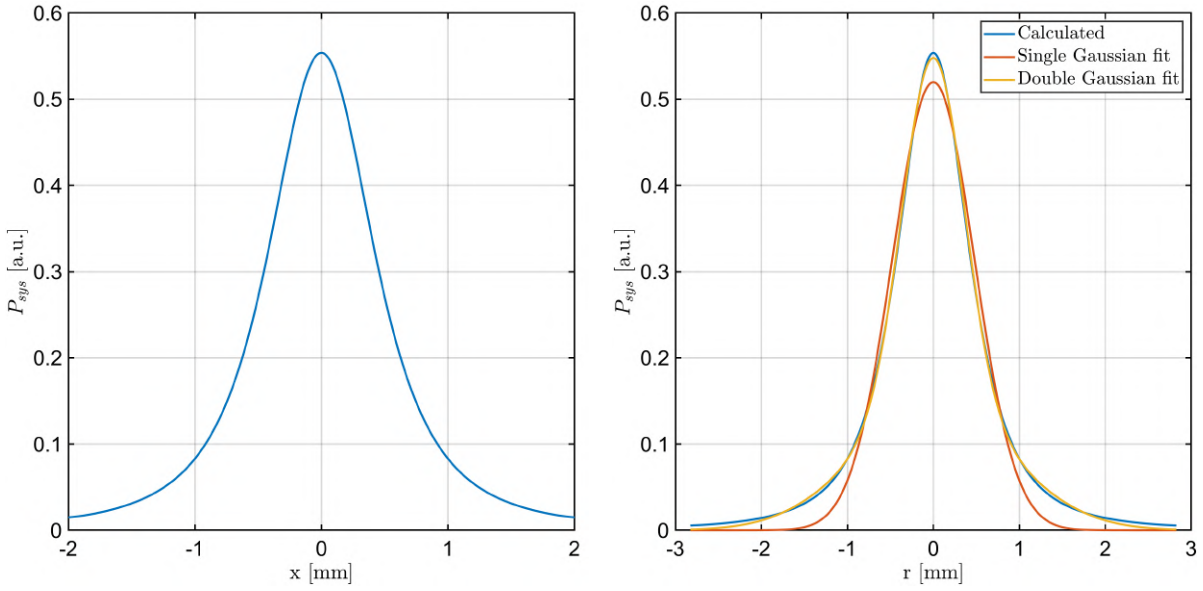

(a) Cross section of the PSF along the x-axis.

(b) Single and double Gaussian fits to the PSF.

Figure 4.15: Combined PSF of the X-ray source and the detector with a magnification factor of 1.24 and focal spot size of 1 mm. Fit attempts to the 1D cross section of the PSF were made using a single and double Gaussian function.

Table 4.1: Fitted parameters of the double Gaussian for the PSF of the system.

Parameter	Value
a_1	0.1397 ± 0.0031
a_2	0.4082 ± 0.0030
σ_1^2 [mm^2]	0.8024 ± 0.0162
σ_2^2 [mm^2]	0.1268 ± 0.0014

Noise

In section 4.3.2 different sources of noise in X-ray images were discussed which could be categorized into two main groups: fixed-pattern noise (FPN) and temporal noise (TN). Although it is theoretically possible to introduce artificial FPN to an image this does not provide much added value to the results as FPN is much easier to correct for in the final image compared to TN or the effect of scattering. It is therefore assumed the detector that is modelled does not show spatial inhomogeneities and the only noise is temporal.

In most cases photon shot noise is the main contributor to the overall noise. As mentioned earlier in most cases photon counting measurements follow Poisson statistics. The photon noise is then easily calculated as the variance is equal to the expectation value, so the standard deviation is found by taking the square root of it. The detector in question is not a photon counter however, but a charge integrator. Unfortunately this means that taking the square root of the calculated intensity is not equal to the standard deviation anymore as the output now also depends on the photon energy besides the number of incident photons. Hsieh et al. [86] developed a analytical model that makes use of a compound-Poisson distribution to calculate the photon noise in a CsI FPD. In this model they make three assumptions. The first one is that the light produced in the scintillator is proportional to the deposited energy with the relation between the light production P and the energy deposition D is given by the following equation:

$$P \propto D = \sum_{E=0}^{E_{max}} E \cdot \Phi_E \cdot \left(\frac{\mu_{ab}}{\mu}\right)_E \cdot \left(1 - e^{-\mu_\rho \cdot \rho_0 \cdot d}\right) \tag{4.54}$$

This equation is very similar to equation 4.38 with the main difference being that it is a discrete function. The second assumption they make is that the image pixel value response is a linear function given by

$$\overline{PV} = p_1 \cdot S + p_2 \tag{4.55}$$

where $\overline{PV}$ is the average pixel value, p_1 the slope of the pixel response, S the photocurrent and p_2 the dark current background. The final assumption is that the photocurrent is directly proportional to the light production and subsequently on the deposited energy:

$$S \propto P \propto D \tag{4.56}$$

The image noise is then directly related to the production of scintillation photons which is in turn proportional to the compound-Poisson statistics of the incoming X-rays and the energy deposition. For each discrete X-ray energy the standard deviation in energy deposition is then given by:

$$\sigma_{D,E} = E \cdot \sqrt{\Phi_E} \cdot \left(\frac{\mu_{ab}}{\mu}\right)_E \cdot \left(1 - e^{-\mu_\rho \cdot \rho_0 \cdot d}\right) \tag{4.57}$$

The total standard deviation in energy deposition can then be calculated using the root sum squared method:

$$\sigma_D = \sqrt{\sum_{E=0}^{E_{max}} \left(\sigma_{D,E}\right)^2} \tag{4.58}$$

Finally the noise in the output is calculated by assuming the image noise response is a linear function independent of energy, resulting in the following equation:

$$\overline{PV} \pm \sigma = \left(p_1 \cdot D + p_2\right) \pm \left(p_1 \cdot \sigma_D\right) \tag{4.59}$$

Although the results from their measurements showed that the relation between the image noise and σ_D is not linear but rather a second-order polynomial, they also showed that the image noise is highly correlated with σ_D. The reason the authors give for the deviation from linearity is that photon noise is not the only contributor to the image noise and that other sources such as thermal and dark noise are the causation. Despite the fact that the linear assumption made in equation 4.59 is likely not entirely correct, it can be used as a conservative estimate of the photon shot noise and interpreted as a best-case scenario. Furthermore, this method shows many similarities to the possible methods for calculating the energy response and equation 4.57 can easily be combined with either equations 4.42 or 4.47.

The other contributions to the temporal noise are much more complicated to compute as there are many different components which all require very in-depth knowledge of the detector to be calculated. Maolinbay et al. [87] developed a extensive model of additive noise, which is noise in absence of radiation. In this model they identify nine separate noise components for which information such as photodiode capacitance, TFT-off resistance and data line resistance is needed. Such a approach is very much outside the scope of this project, but it might be possible to get an estimation of the total effect of these components. As part of the first set of measurements dark images were taken, which can be used to calculate the standard deviation of the detector output in absence of radiation, giving an indication of the dark noise.

Besides the different kinds of noise discussed in the preceding part there are other temporal effects that can influence the image quality. Two identified by Kördel [72] are image lag and ghosting. Image lag is the phenomenon that residual signal remains on a pixel and is carried over to the next frame. Ghosting is the change in detector sensitivity due to previous exposure. The datasheet for the 3131 detector states that image lag is less than 0.1%, so neglecting its effect seems like an reasonable approximation. The datasheet does not provide any information on ghosting and identifying the effect would require specialized measurements. Kördel found that the signal showed a significant increase in signal even though the incoming X-ray intensity was kept constant. Although the measurements that could be done were done over much shorter time periods it might be wise to see if such an effect can be discovered.

Simulation based on ray-tracing techniques must be used with care because sampling is carried out when computing images. In a real detector, each pixel gives a signal corresponding to all the photons hitting its surface, whereas, in simulation, all the photons are "concentrated" in the center of the pixel. If this approximation is judged too rough, a finer computation can be performed by dividing each pixel into smaller sub-pixels. When the calculation is complete, the signals corresponding to the sub-pixels are just added to constitute the final signal.

4.4. Calculation of average densities

BESIDES the structure and relative density differences of the SC fluid the actual density values are also of interest. Unfortunately, as the images are a 2D projection of a 3D fluid at best only integrated or average densities along the path of the X-rays can be calculated. In order to get localized density values computed tomography would have to be used, which is not an option for the current setup. Calculation of average densities is a relatively simple procedure if using monoenergetic X-rays. This is done by taking equation 2.5 and factoring out ρ:

$$\rho = \frac{-\ln\left(\frac{I}{I_0}\right)}{\mu_\rho(E)\, x} \tag{4.60}$$

For the case of the SC fluid in the RB cell I would be the intensity measured with R-23 in the cell, I_0 the intensity with only air in the cell, $\mu_\rho(E)$ the mass attenuation coefficient at the energy of the monoenergetic X-rays and x the total distance through the fluid. This approach neglects the attenuation of the X-rays due to the air in the cell, but this can be taken into account if needed.

This method breaks down however when a polyenergetic X-ray source is used. The measured intensity is now a product of X-rays of many different energies and is described by an equation looking like 2.9. It is clear that rho can not be simply extracted from this equation. A proposed solution to this problem is the use of an effective or averaged attenuation coefficient $\langle\mu\rangle$ which is μ averaged over the energy fluence spectrum. In theory this would allow the calculation of the attenuation of the energy fluence:

$$\Psi(x) = \Psi_0 e^{-\langle\mu\rangle x} \tag{4.61}$$

This description is not complete however as it ignores the effect of beam hardening. As the X-rays travel through a medium the energy fluence spectrum changes as the beam hardens. This means that $\langle\mu\rangle$ is a function of the penetration depth. Taking inspiration from the paper by Alles and Mudde [88] the local measured mass attenuation coefficient for a homogeneous medium can be written as

$$\langle\mu_\rho\rangle_{\Psi(x)} = \frac{\int \Psi_E(x)\mu_\rho(E)dE}{\Psi(x)} = \frac{\int (\Psi_E)_0\, e^{-\mu_\rho(E)\rho x}\mu_\rho(E)dE}{\int (\Psi_E)_0\, e^{-\mu_\rho(E)\rho x}dE} \tag{4.62}$$

where the subscript $\Psi(x)$ indicates that the average coefficient is a function of the local energy fluence. The attenuation of the polychromatic beam can then be cast into the familiar Lambert-Beer form:

$$\Psi(L) = \Psi_0 e^{-\int_0^L \langle\mu_\rho\rangle_{\Psi(x)}\rho dx} \tag{4.63}$$

where L is the total distance traveled through the medium. Since the medium is considered homogeneous ρ is independent of the penetration depth and can be taken out of the integral. The equation can be further rewritten as

$$\rho\int_0^L \langle\mu_\rho\rangle_{\Psi(x)dx} = -\ln\left(\frac{\Psi(L)}{\Psi_0}\right) \tag{4.64}$$

From equation 4.62 it can be seen that $\langle\mu_\rho\rangle_{\Psi(x)}$ besides the penetration depth also depends on the density of the medium, which makes sense as denser media result in increased beam hardening. This means the integral in the equation above is a function of medium density:

$$\rho f(\rho) = F(\rho) = -\ln\left(\frac{\Psi(L)}{\Psi_0}\right) \tag{4.65}$$

By fitting a function dependent on the density to the left side of the equation the average density can be found by solving the equation. Depending on the form of the fit multiple solutions are possible, but since the valid range of possible densities is known nonphysical solutions can be discarded. The valid range can be determined by looking at the temperatures applied to the top and bottom of the cell and the pressure. $F(\rho)$ was calculated for R-23 densities ranging from 0.3 to 0.8 g/cm^3 with as $(\Psi_E)_0$ the energy fluence spectrum attenuated by 100 cm air and the glass of the first flange of the RB cell. The results of these calculations and the subsequent fit can be seen in figure 4.16. In the density region used the curve can be accurately fitted using a first-order polynomial of the form $F(\rho) = P_1\rho + P_2$ which results in only one solution to equation 4.65:

$$\rho = \frac{-\ln\left(\frac{\Psi(L)}{\Psi_0}\right) - P_2}{P_1} \tag{4.66}$$

with P_1 and P_2 equal to 1.1186 and 0.0029 respectively. Since the output of the detector is proportional to the deposited energy Ψ can be replaced by intensities in ADUs to calculate the average densities using the detector output. It should be taken into account that like the work by Alles and Mudde [88] a perfect detector was assumed in the derivation of the final expression. No energy response function was incorporated into the equations, but they state that this should be a simple operation. Although an attempt was made to find this response function as described in the previous section, due to time limitations and uncertainty of how this should be implemented it was decided that this could be done as part of a possible continuation project.

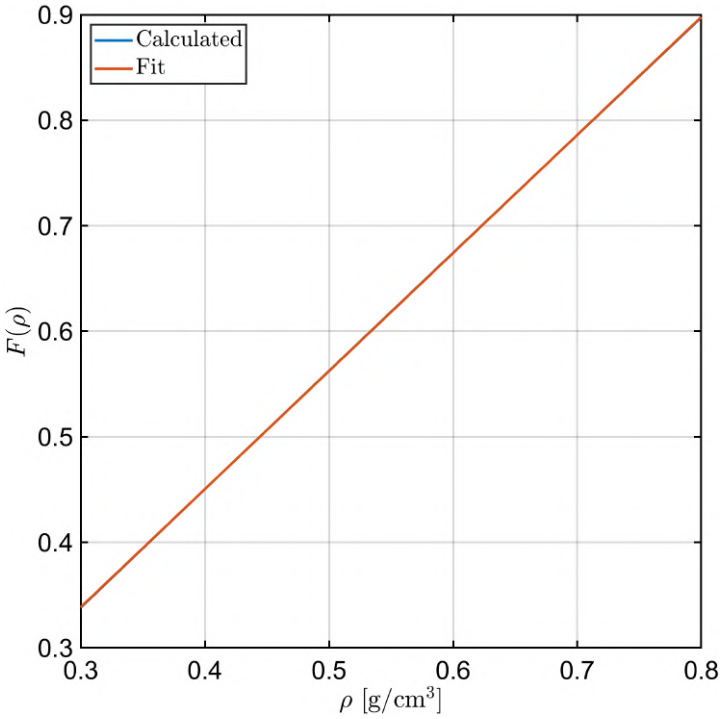

Figure 4.16: Calculated values of $F(\rho)$ and first-order polynomial fit to the results.

4.5. Computation of images

THE general process of computation of the images will be given an explanation in this section using pseudo-code. The calculation of transmission and scattering is split into two parts as they were calculated separately.

Define constant parameters
Define pixel pitch size and number of pixel elements
Define voxel size and number of voxels in x/y/z direction
Define ROI of the detector
Define source characteristics and calculate X-ray spectrum
Load and interpolate material properties
Construct sample density and material geometries

Transmission:
for each pixel **do**
Cast ray between S and P and calculate l_m and $\rho(i_m, j_m, k_m)$
for each energy E **do**
Calculate $(\Phi_E)_{det}$
end for
Calculate E_{dep} OR intensity in ADUs
Calculate σ_D
end for

Scattering:
for each voxel **do**
Cast ray between S and A and calculate l_m and $\rho(i_m, j_m, k_m)$
Calculate $(\Phi_E)_A$
for each pixel **do**
Cast ray between A and P and calculate l_m and $\rho(i_m, j_m, k_m)$
Compute $\cos(\theta)$, $d\Omega_P$, $\frac{d\sigma_T}{d\Omega}$
for each energy E **do**

Compute E_{Co}, x, $\frac{d\sigma_{KN}}{d\Omega}$, $[F(x)]^2$, $S(x)$, $\mu_{\rho,m}(E_{Co})$, $\frac{d\sigma_{Ra}}{d\Omega}$, $\frac{d\sigma_{Co}}{d\Omega}$, d^2N_{Ra}, d^2N_{Co}
end for
Calculate E_{dep} OR intensity in ADUs
Calculate σ_D
end for
end for

Data processing:
Convolution of image with PSF
Apply noise to image
Additional processing
Computation of average densities

Looking at the algorithm above it is clear that the main part of the calculations is performed using for-loops. Furthermore, these loops are independent of each other as the results from one loop are not influenced by or dependant on the results of another. This makes parallel computing a excellent tool to try to reduce calculation time. MATLAB has a parallel computing toolbox which allows the user to solve computationally and data-intensive problems using multicore processors, GPUs, and computer clusters. The simplest function that is included in this toolbox is the parfor-loop which executes for-loop iterations in parallel on workers. To speed up calculations both parallel computing on the local hardware and on a cluster were used.

5

Results & Discussion

In this chapter the results from both the experimental and numerical work will be shown and discussed. The first section will discuss the preliminary measurements that were performed together with the results and their significance for the simulations and possible future research. The second section will give a brief overview of the successes and failures of the model, after which the simulation results are discussed.

5.1. Experimental results

In section 3.2.1 it was mentioned that two sets of preliminary measurements were performed. The objective of the first set was to get acquainted with both the hardware and software. Out of these measurements the first two provide the most useful information for further use. The first measurement was the acquisition of dark field (DF) images. These images were taken in absence of incoming radiation, so the only measured signal is due to background radiation, dark current noise etc. 100 images were taken at a frequency of 22 Hz. Standard practice is to display these images in gray scale with pixel values above a certain threshold becoming red to indicate the intensity at said pixel is close to or above clipping. Figure 5.1 shows the average of the dark field intensities measured using a gray scale. As one would expect in absence of incoming X-rays the image is pure black, but the use of the gray scale might hide detail due to the large range of intensities it covers.

Figure 5.1: Gray scale image of the average dark field intensity.

Changing the scale to full colour covering a much smaller range of intensities results in the image shown

in figure 5.2(a). It is immediately clear that the DF images are not as uniform as previously thought. The image shows patterns of pixel columns with approximately constant intensity. The maximum difference in intensity between these lines is roughly 50 ADU. Furthermore there is also a clear divide between the top and bottom half of the detector. The most likely explanation for these effects is that they are the result of the manufacturing process where the total detector panel is made by combining two separate which are themselves made out of individual pixel rows. Although 50 ADU is a relatively small number compared to to maximum possible intensity value it still might prove to be a significant factor if the SC fluid produces intensity differences on this scale. Almost all pixels of the topmost row also display the maximum intensity value of 16383 indicating a faulty row. Ignoring this row the mean intensity of the image is almost 325 ADU. Besides the average intensity the standard deviation of each pixel was also calculated to get an idea of the dark noise intensity and is displayed in figure 5.2. This image shows an even clearer divide between the top and bottom part of the detector. The top half shows a largely uniform standard deviation asides from a small part near the top which might be related to the faulty row. The bottom part on the other hand shows much larger variations in noise intensity , again in columnar pattern, and higher average noise. It is however expected that the maximum value of dark noise will still be much lower than the noise intensity due to for example photon shot noise.

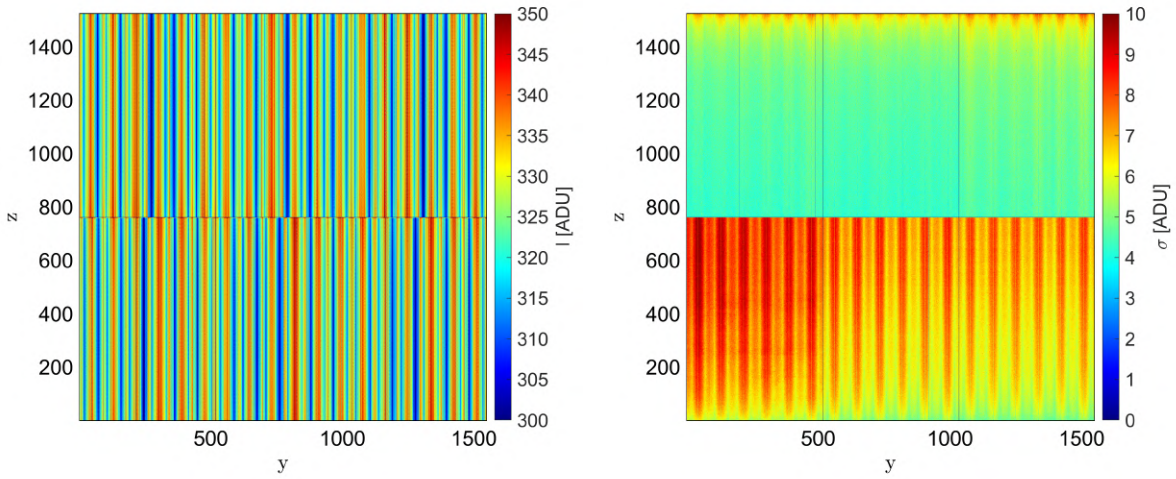

(a) Colour scale image of the average dark field intensity.

(b) Colour scale image of the dark field standard deviation.

Figure 5.2: Colour images of the average dark field intensity and standard deviation.

During the second measurement flat field images were acquired. The tube voltage was set to 120 kV and a tube current of 0.7 mA was used. This resulted in clipping in the image so the current was reduced to 0.5 mA. Like the first measurement 100 images were taken at a frequency of 22 Hz. Again the gray scale image implies a largely homogeneous intensity, but looking at the average colour scale image in figure 5.3(a) shows this is not true. Although the columnar pattern from figure 5.2(a) no longer appears there is a significant vertical asymmetry in the intensity. The most likely explanation is that this is due to the heel effect. Starting from the top moving downwards decreases the corresponding take-off angle, increasing the path length and subsequent attenuation in the target. The same can be said for the horizontal direction when starting in the center and moving either left or right, although this effect is much smaller which is in accordance with theory. Using the X-ray source model to calculate the relative decrease in intensity as the take-off angle decreases and comparing it with the measured relative decrease shows good agreement, indicating the model is accurate in simulating the heel effect.

Besides the apparent heel effect some other artifacts can be seen. The most notable are the dark lines running vertical along the detector. The pixels in these lines have values roughly 60% of the surrounding pixels. Possible explanations are that these pixels have a reduced sensitivity to incoming radiation, resulting in a lower intensity output, or are completely dead but still produce a output due to charge sharing with neighbours.

This second explanation seems more likely by looking at the left and right edges of the image. Here a several pixel wide dark strip can be seen. Looking more closely reveals that the intensity is lowest in the outermost column, slowly increasing while moving inwards until arriving at the innermost column whose values are approximately equal to those of the dark lines.

Like for the DF images the standard deviation of the FF images was also calculated and is displayed in figure 5.3(b). Like for the DF images the noise in the top half of the detector is largely homogeneous. The average noise in the bottom half is lower than in the top half which is expected as noise increases with signal intensity. One peculiar detail is that the noise appears to show a somewhat concave distribution in contrast to the average intensity in figure 5.3(a) where is more convex. It is unclear what the cause of this is, but it is most likely due to detector defects and inhomogeneities. Like it was expected the dark noise is only a small contributor to the total noise and can in all likelihood be neglected. In the previous chapter it was discussed that photon counting measurements display photon shot noise that follows a Poisson distribution. If that would also be true for these measurements the standard deviation should be approximately equal to the square root of the measured intensity. Taking the square root of the FF image and dividing it with the standard deviation shows that this is false and that the standard deviation is larger than the intensity. Some further investigation reveals that it is roughly equal to the square root of two times the intensity. A possible explanation might be that the imaging actually consists of two photon counting measurements: the first one is the detection of the X-rays while the second one is the detection of the scintillation photons. Assuming that each process results in noise equal to the square root of the measured intensity indeed results in a total noise equal to the square root of two times the intensity if using the square root sum method, but this seems too simplistic and lacks strong substantiation. Besides the DF and FF measurements other measurements were done involving a fluidized bed of micro particles, but the results of these measurement were not of further use.

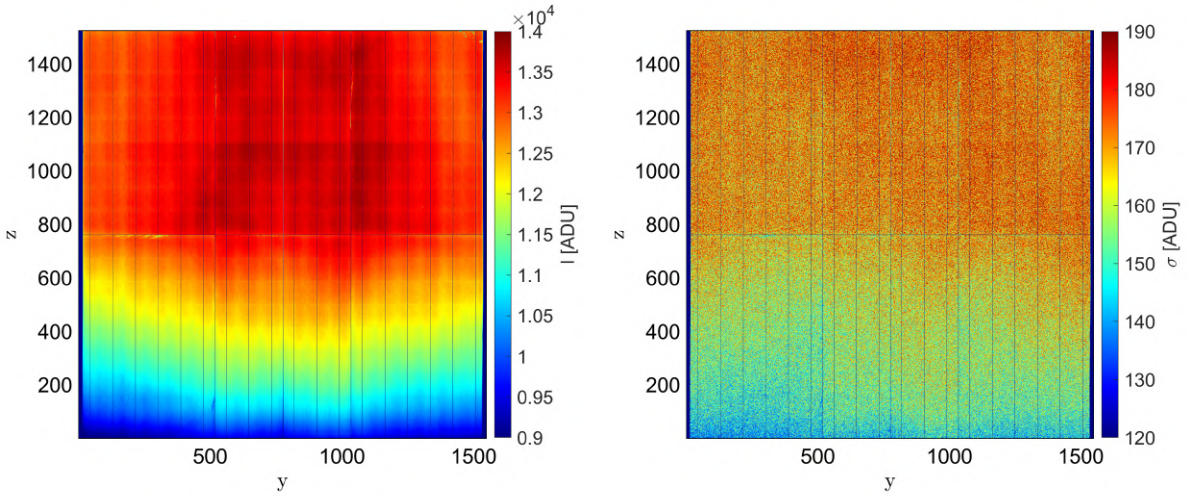

(a) Colour scale image of the average flat field intensity.

(b) Colour scale image of the flat field standard deviation.

Figure 5.3: Colour images of the average flat field intensity and standard deviation.

The second set of measurements was done to see if enough X-rays could pass through the cell to form an useful image and if so which settings for the X-ray tube should be used. All measurements were done at 22 Hz and for each measurement 100 images were taken, with the first couple of measurements done with the central cube of the cell empty. For the first measurement the tube voltage was set to 75 kV and the current to 5 mA, but this resulted in an approximate intensity of only 450 ADU directly behind the central part of the cell. The current was increased to 22.5 mA and another set of images was taken, but the intensity behind the windows was still to low so the tube voltage was increased. Due to the X-ray tube having a maximum power increasing the tube voltage meant that the current had to be decreased. Measurements were done with a voltage-current pairs of 100 kV and 18 mA, 120 kV and 15 mA and finally 150 kV, which is the maximum voltage, and 12 mA. The resulting average gray scale images are shown in figure 5.4. All images show clipping

on the detector parts not covered by the cell. It is clear that at 150 kV the intensity behind the windows is the highest even though the current is the lowest at these settings. This can be explained by the fact that at 150 kV the X-rays have the highest maximum and average energy, which means that they are less attenuated. Furthermore according to equation 2.1 at these energies the efficiency is proportional to the tube voltage so the higher voltage compensates for the lower current. Finally it can be seen that the orientation of the dark lines has changed with them now running horizontally. This is due to the detector being rotated 90 degrees for other measurements prior to this set. This meant the output images had to be rotated 90 degrees counter-clockwise to get the correct orientation, but there should be no further influences on the results.

(a) 75 kV, 22.5 mA

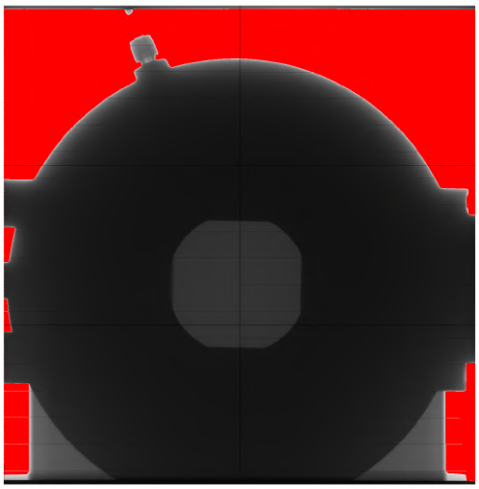

(b) 100 kV, 18 mA

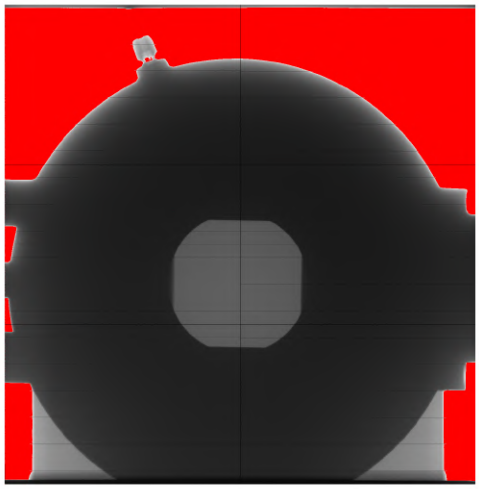

(c) 120 kV, 15 mA

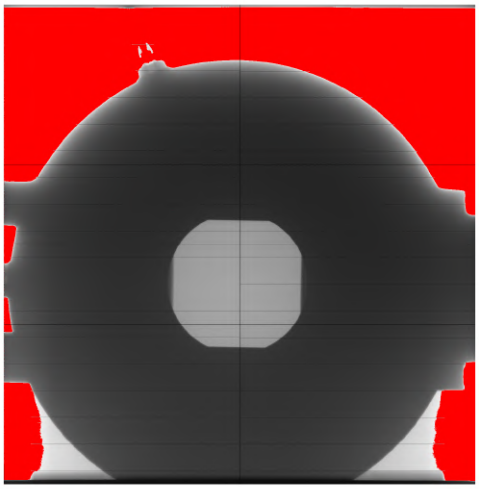

(d) 150 kV, 12 mA.

Figure 5.4: Average gray scale images for various voltage-current pairs.

Looking at the images in 5.4 besides the intensity behind the core the intensity behind the surrounding cage also increases, with values ranging from 3000 to 4000 ADU. It was expected that the thickness and high density of the cage would attenuate essentially all incoming X-rays, which is confirmed by a quick calculation. This implies the signal behind the cage is produced mostly by scattered X-rays. To see if the scattering contribu-

tion could be reduced two lead slit collimators were placed in front of the source with the slits perpendicular to each other, creating a square aperture. Figure 5.5(a) shows the resulting image. The collimator effectively blocks the X-rays from passing by the cell, removing the clipping. Although the collimator reduces the intensity everywhere in the image ignoring the clipped parts the effect is most significant behind the steel parts of the cell. Here the intensity is reduced by approximately a factor 6 compared to a roughly 10% reduction in the center, confirming the hypothesis that the image intensity behind the steel parts was mostly due to scattering. To get an estimate of the dynamic range that could be expected from the actual measurements with the SC R-23 the cell was partially filled with 0.5 mm polystyrene particles. The corresponding image is displayed in figure 5.5(b). The maximum intensity behind the filled part of the cell is approximately 4700 ADU, compared to the maximum of 9200 for the empty cell. Looking at figure 3.5 the attenuation by the cell filled with the particles is almost equal to attenuation by the cell filled with R-23 at high density. At low density the transmission is just above two-thirds of the transmission of the empty cell at the relevant energies, so the expected dynamic range for the actual measurements is likely to lie between 4700 and 6400 ADU.

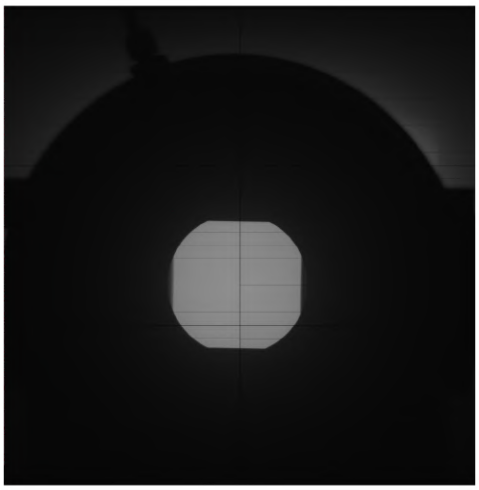

(a) Averaged gray scale image of the empty cell with a collimated beam, 150 kV and 12 mA tube settings.

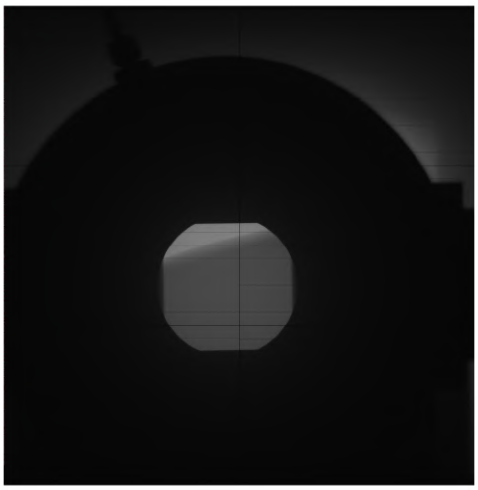

(b) Averaged gray scale image of the partially filled cell with a collimated beam, 150 kV and 12 mA tube settings..

Figure 5.5: Averaged gray scale images of the empty and partially filled cell with a collimated beam.

The scattering influence can be studied in more detail by looking at the respective color scale images of the images in 5.5, shown in figures 5.6(a) and 5.6(b) in which the central part of the images has been enlarged. Starting at the left image there seems to be a intensity distribution that has a maximum value close to the center and shows some point symmetry. The first thought is that this is due spatial inhomogeneities of the beam due to the heel effect, but this can quickly be disproven. First of all there is symmetry along the vertical axis, while the heel effect would result in high intensity at the top and low at the bottom. Furthermore the effect takes place over smaller spatial lengths than those seen in figure 5.3(a). Finally this close-up is located in the central part of the detector plane which is shown to be largely homogeneous in intensity in figure 5.3(a). The most likely explanation therefore is that this is the result of scattering in the glass windows and from the internal parts of the cell. Moving away from the center of the detector results in more and more of the scattered X-rays being blocked by the steel cage, resulting in a gradual decrease in total intensity as can be seen in figure 5.6(a). The image of the partially filled cell shows the same behaviour, although it appears to be more granulated as a result of the particles.

Looking at the standard deviation of the partially filled cell images allows for easy comparison of the noise of an empty cell and a filled one. As expected figure 5.7(a) shows that the standard deviation is lower for the filled part of the cell and the relative change in noise while moving away from the center is much smaller than for the intensity itself. Although the noise is lower behind the filled part this does not mean detail visibility will be better as noise level itself does not provide enough information. A better metric is the signal-to-noise ratio (SNR) which is the ratio between the average measured intensity and the corresponding standard deviation.

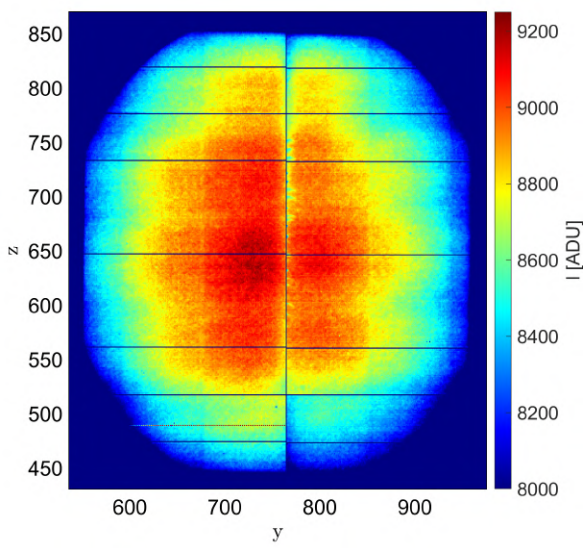

(a) Averaged colour scale image of the empty cell with a collimated beam, 150 kV and 12 mA tube settings.

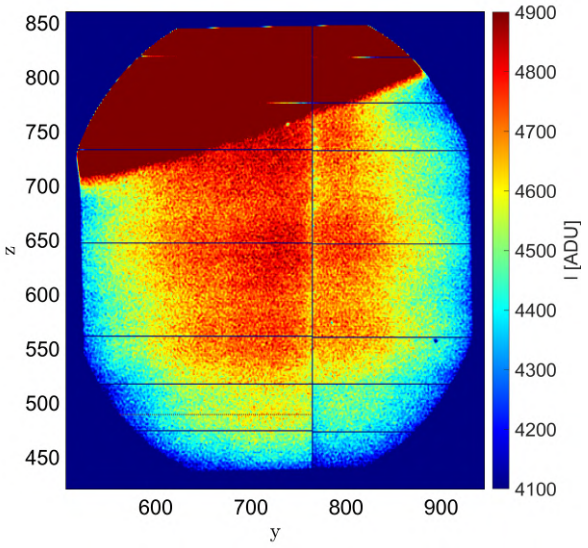

(b) Averaged colour scale image of the partially filled cell with a collimated beam, 150 kV and 12 mA tube settings..

Figure 5.6: Averaged colour scale images of the empty and partially filled cell with a collimated beam.

In ideal circumstances this ration would be infinite, but in practice this is never achievable. Figure 5.7(b) shows the SNR of the partially filled cell. Although the absolute noise level is higher for the empty part of the cell compared to the filled part the relative difference in average intensity is even bigger resulting in a higher SNR. From this image it can be estimated that the SNR of the measurements with the R-23 will lie between approximately 40 and 50.

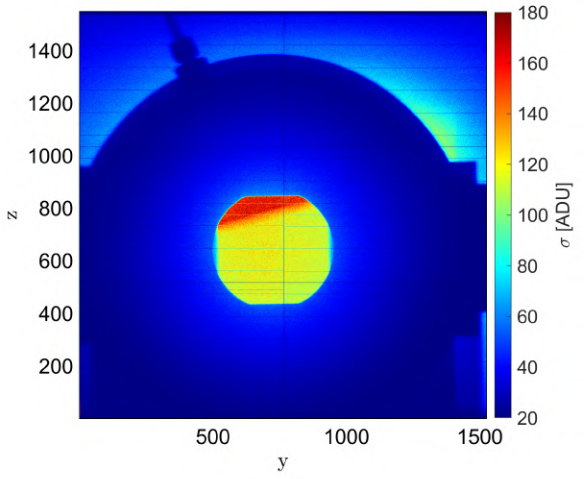

(a) Standard deviation colour scale image of the partially filled cell with a collimated beam, 150 kV and 12 mA tube settings.

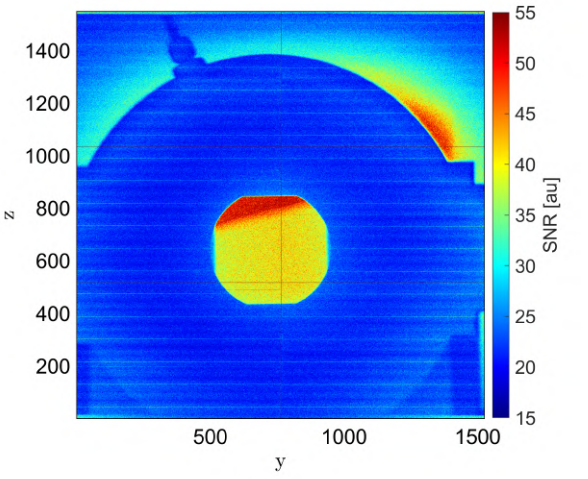

(b) SNR colour scale image of the partially filled cell with a collimated beam, 150 kV and 12 mA tube settings.

Figure 5.7: Standard deviation and SNR colour scale images of the partially filled cell with a collimated beam.

For optimal image quality the scatter contribution should be as low as possible. Besides using a collimator reducing the tube voltage should in theory reduce the relative contribution of scatter to the total signal as the photoelectric effect becomes more dominant at lower X-ray energies. A drawback of this method is that the

average intensity and therefore the SNR also decrease. The easiest way to see if reducing the tube voltage has a noticeable effect on the scattering contribution is to look at the intensity profiles. Figure 5.8(a) shows the horizontal intensity profiles of the images in figure 5.4 at vertical pixel number 640. Looking at the central peak it can be seen that the curve which is thought the be the result of scattering becomes less pronounced as tube voltage decreases. Comparing the values of the central peak with those to the left and right however shows that relative scattering contribution to the total signal actually increases. Furthermore the scattering contribution is also slightly higher at the left side, resulting in a somewhat lopsided curve. Although the absolute difference in intensity between the center of the curve and the ends has a significant on detail visibility the relative difference is equally important. To compare this for the different tube voltages the profiles in figure 5.8(a) have been normalized with respect to the surface underneath the curve and are plotted in figure 5.8(b). Comparing the curves reveals that for 75 kV is indeed flatter than the one for 150 kV, but for the other voltages the relative differences are largely the same. Additionally it confirms that for 150 kV the relative scatter contribution is the lowest.

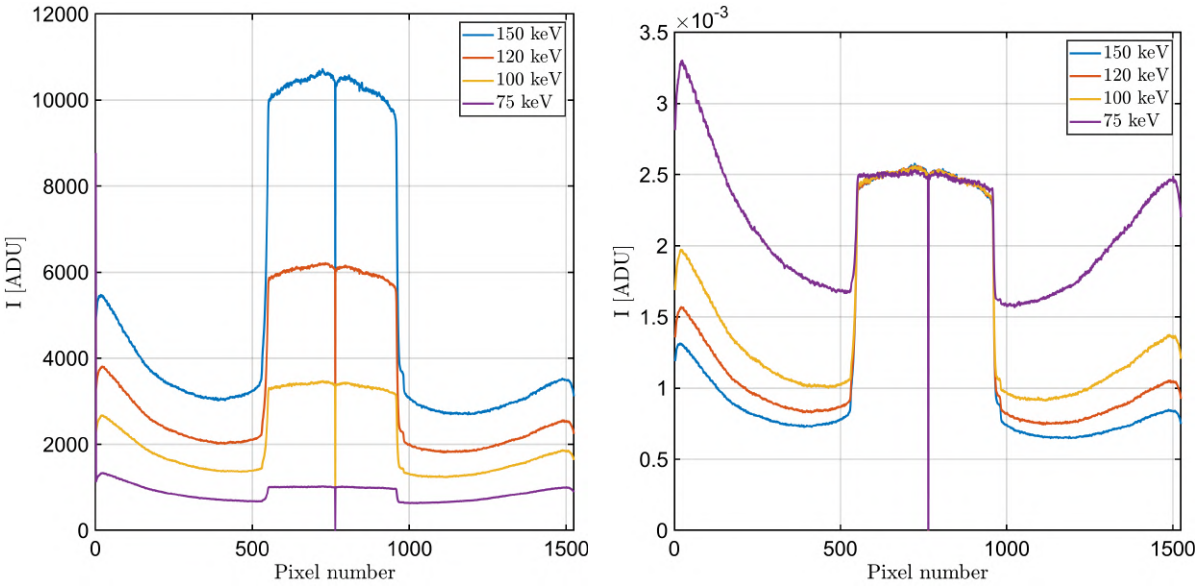

(a) Horizontal intensity profiles.

(b) Normalized horizontal intensity profiles.

Figure 5.8: Horizontal intensity profiles images acquired at 75, 100, 120 and 150 kV tube voltage without collimator.

Finally, to check the effects of the collimator and the polystyrene particles on the scatter profile the horizontal intensity profiles of the images acquired at 150 kV without collimator, with collimator and filled with particles are plotted in figure 5.9(a). Filling the cell with the particles involved removing it from the setup up and placing it back which resulted in a slight shift in location of the central peak. The profiles clearly show the effect of the collimator and its effectiveness at reducing scatter. For both collimated profiles the curve has become more symmetrical, but it also appears that the central peak has become more pronounced. Normalizing the curves and comparing them in figure 5.9(b) shows that the collimator and particles have no significant influence on the central curve, but filling the cell does increase the relative contribution of scatter. The profile of the partially filled cell was manually shifted to the right to get a better overlap with the other profiles. From these results it can be concluded that using the maximum tube voltage will likely result in the highest quality images. The SNR increases with image intensity and decreasing the tube voltage did not yield any appreciable decrease in scattering. The scattering itself appears to be largely independent of tube voltage and cell contents and seems to be mostly dependent on the X-ray intensity reaching the detector. This might make it possible to get an estimation of the scatter in the images which can then be subtracted to increase detail visibility.

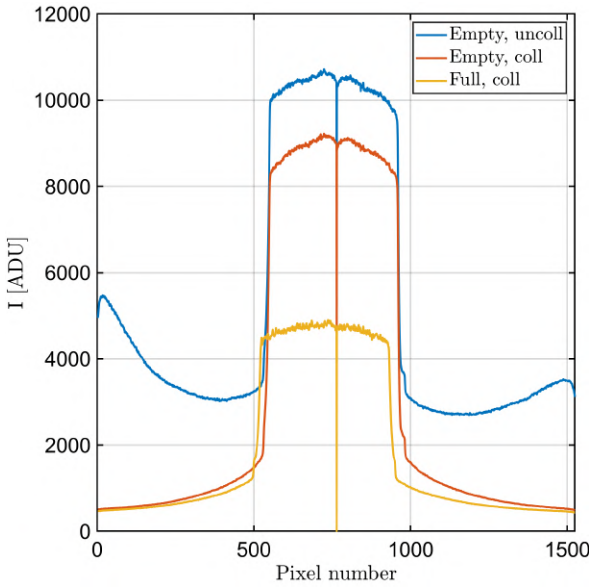

(a) Standard deviation colour scale image of the partially filled cell with a collimated beam, 150 kV and 12 mA tube settings.

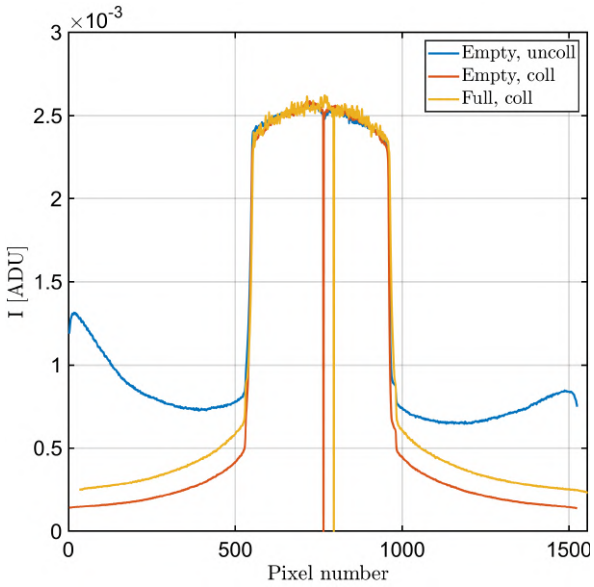

(b) SNR colour scale image of the partially filled cell with a collimated beam, 150 kV and 12 mA tube settings..

Figure 5.9: Standard deviation and SNR colour scale images of the partially filled cell with a collimated beam.

5.2. Numerical results

In this section the results of the simulations and their implications for future research will be discussed. In the first part the successes and failures of the simulation of X-ray transmission and scattering are reviewed. In the second part the simulation results are shown and examined. For the sake of brevity only the final results are discussed in detail.

5.2.1. Simulation validity

Transmission

It was hoped that using the X-ray tube model by Omar et al. [47] and the method and values of Cao et al. [51] would allow the calculation of detector output intensity without the need for experimental values to supplement the model. Unfortunately the simulation of some of the measurements mentioned in the previous section gave results that deviated significantly from those that were measured. It is difficult to pinpoint a precise cause of the deviation. Starting at the source it is possible that the modeled output does not match the actual one. The spectral distribution has been well validated against experimental and MC-calculated results, so it is expected that the model is accurate in this regard. For the output intensity itself Omar et al. [47] mention that the model is able to reproduce the number of produced X-rays per incident electron to within approximately 2% of MC-calculated results, but they stress that the output of individual X-ray tubes varies. They advise that by normalizing the spectrum to match the measured tube output more accurate predictions of the number of X-rays emitted from the tube in question might be achieved. The difference between the simulated and measured results however has a magnitude that is unlikely to be caused by this error.

A second possibility is that the attenuation in the object is not calculated correctly. As discussed in the previous chapter use of Bragg's law to calculate the mass attenuation coefficients of compounds and mixtures can result in large errors around the absorption edges of the elements that constitute said materials. The coefficients for single atoms themselves are based on theoretical calculations which might also deviate from the true values. Again it is unlikely that these are the cause of the discrepancy between the results. Both Bragg's law and the values from the XCOM database have been used for many years to get accurate results and would be completely unusable if they would lead to deviations of this magnitude.

Finally it is possible approach to model the detector is not correct. This seems like the most likely explanation. Aside from the pixel pitch and scintillator material very little is known about the properties that are relevant to the conversion from incoming X-rays to the output in ADU such as the scintillator thickness, scintillation

photon detection efficiency and several other factors. The model in its current state uses many estimations and assumptions that are based on the properties of other detector and other factors are completely left out. It is therefore not unexpected that the simulated detector output does not exactly match the measured one, but at the moment the difference is too large for the model output to be considered accurate enough for further use.

The second option that would not require experimental values was to convert the manufacturer supplied saturation dose to a corresponding absorbed energy dose per pixel and match said dose to the maximum pixel output. Unfortunately this method resulted in even bigger differences between model output and measured results. This might be due to the method used to convert the measured saturation dose in air at the surface of the detector to total energy absorbed per pixel. It also depends on detector properties that have been estimated which can also introduce errors. As both methods were deemed not accurate enough the decision was made to use the same method as Endrizzi et al. [70], who determined the conversion factor between absorbed energy and ADU experimentally. They were able to make use of monochromatic X-rays at multiple energies to determine this coefficient. This luxury was not available in this project so the coefficient has to be determined using one of the measurements that had been done beforehand.

Finally the compound-Poisson method to calculate the image noise produced noise values between a factor three and four lower then those measured. This is not unexpected as this method does not take other noise sources into account and the paper it was taken from also states it underestimates the total noise. The intensity differences as a result of density differences in the fluid are expected to be relatively small so image noise will be a significant factor in image quality. Underestimating it will result in simulated images with unattainable high quality, so a better method so introduce noise to the simulated images is to calculate the standard deviation using the measured SNRs. It is very likely those will lie between 40 and 50 and can thus be used to calculate an expectation of the noise by dividing the simulated intensity by the SNR to find the standard deviation.

Scattering

In order to check if the deterministic scattering algorithm was implemented correctly the same setup as the one used by Freud et al. [34] to check the validity of the algorithm was simulated. The results were compared to those of Freud et al. and showed good agreement, indicating good implementation. Due to the sheer number of calculations required to determine the scatter contribution of the cell some assumptions were made to reduce them and make the computation time more manageable. The first one was that is was assumed the collimator was aligned perfectly and that the X-ray beam would only pass through the glass windows and central cube. Combining this with a first-order approximation meant that only scattering in the glass and in the contents of the central cube would have to be simulated. The second assumption was that the scattering difference between voxels close to each other would be very small. As such scattering would not have to be calculated for all voxels but only a subset and the total contribution can then be calculated by interpolation between voxels of which scattering has been calculated. The easiest method to do so is to divide the voxels into 'sheets' perpendicular to the X-ray propagation direction. The contribution of each sheet is stored separately and is used to find the total scatter contribution.

To test this method radiography of an empty cell was simulated. The tube settings were set to 150 kV and 12 mA. The distance between the source and the surface of the front window was set to 100 cm and the distance between the surface of the back window to 20 cm. For the transmission image 0.1 mm cubic voxels were used to ensure no artificial artifacts are introduced in the image as they are smaller than the pixel pitch. Using this voxel size results in an object 2500 by 2500 by 1340 or more than 8 billion voxels. For the sample containing the material codes this is not an issue as the materials are represented using integers so the uint8 data type can be used. For the sample containing the density values this is different as the densities are not integer values. MATLAB uses double as the default numeric data type, but using double values causes the object data size to become too large. As a result single values have to be used, which are stored as 32-bit floating points as opposed to 64-bit for double values. This means the precision in density values is less, but for the current objective this difference should be negligible. A second consequence of the large object size is that parallel computation on the local hardware or on the cluster no longer works as not enough memory is available to handle it, even when using single values. Shortly after starting the parallel computation an error will display and the calculation continues in serial mode. Since the only area of interest is directly behind the glass windows and the surrounding area the transmission was not calculated for each pixel in the detector both only for a central ROI of 568 by 568 pixels. Finally energy bins of 0.5 keV were used for a total of 291 bins

ranging from 5 to 150 keV. These settings were also used for all other transmission images discussed in the next section.

Using these settings calculation of the transmission image took approximately 40 minutes. The resulting image can be seen in figure 5.10(a) with the deposited energy not yet converted to ADU. Comparing it to the measured image in figure 5.6(a) it looks like the edges of the window are visualized correctly. The exact distances between the source and cell and between the cell and detector during the measurements were unfortunately not recorded, so these had to be guessed. Comparing the width in pixels between the left and right edge in figure 5.6(a) and figure 5.10(a) shows that they are almost equal (around 410 and 430 pixels respectively) which means that the distances used for the simulation are close to those of the measurements. It can also be seen that the intensity decreases when moving away from the center, but the differences are very small. This decrease is the result of the inverse-square law and longer path lengths in the glass.

For the scattering image the same distances and tube settings were used, but this time energy bins of 5 keV were used for a total of 30 bins. Using bins this wide results in the characteristic peaks being neglected, but they only account for a small fraction of the total energy and since most calculation time is spend on energy integration reducing the number of bins significantly reduces the total computation time. The voxel size was set to 0.5 mm, which is the limit suggested by Freud et al. [34]. To further reduce the number of calculations two sheets were used, one in the middle of the first glass and one in the second. Scattering from the air inside the cell was ignored. Using these values the sample consists of only 65000 voxels and only scatter from 392 voxels had to be calculated although this would still take around 260 hours if the other settings were kept the same. As the sample size was much smaller parallel computing could be used. The laptop used had 6 cores available for parallel computations. The total calculation time using these settings and parallel computation was just above 2 hours. By using the contribution of each sheet as the average of each window the total scatter contribution is calculated by multiplying each sheet with the total number of sheets in the window and adding up the results. The total deposited energy in the detector due to scattered X-rays is shown in figure 5.10(b). It is immediately clear that the intensity distribution looks very similar to the ones in figures 5.6(a) and 5.6(b) although much cleaner. In the corners artifacts that are the result of the large voxels size are visible. At this size representing a circle using square blocks does not produce a smooth circumference.

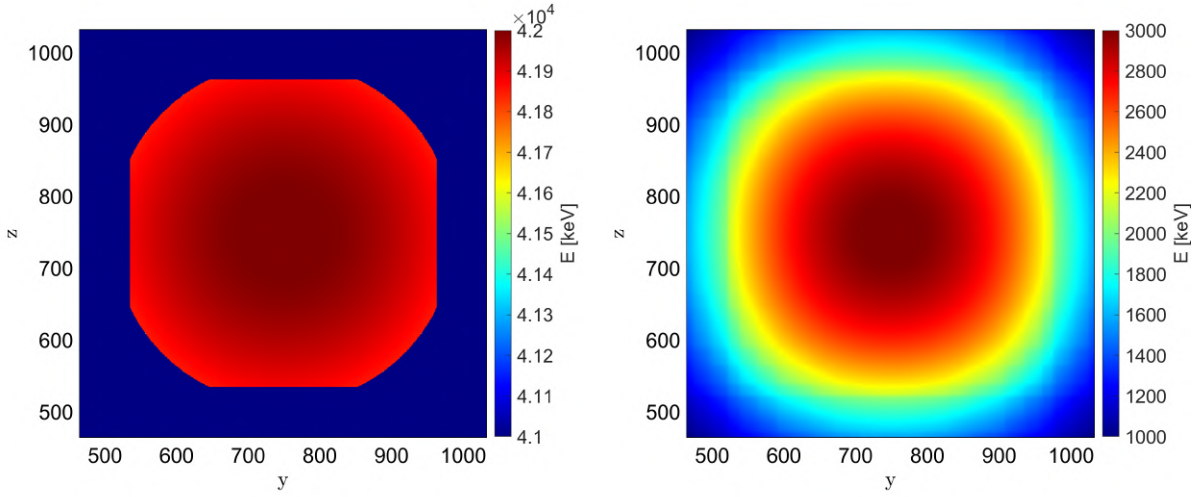

(a) Energy deposited by X-rays transmitted through the empty cell.

(b) Energy deposited by first-order scattered X-rays.

Figure 5.10: Energy deposited in the detector by X-rays transmitted through the empty cell and X-rays scattered in the windows.

Comparing the intensities of the transmission image with those of the scattering image shows that the contribution of the scatter to the total signal is only a very small fraction, approximately 7% in the center of the image. This much smaller than the estimated contribution based on the measurements which is around 30%. A possible explanation might be that since the collimator for the measurements was not aligned perfectly the X-ray beam was also incident on the internal walls of the central cube from which X-rays could

scatter towards the detector. It is also possible that the approach using sheets to calculate the total scattering contribution is flawed, but comparing the contribution of the sheet in the front window with the one from the back shows only a maximum difference of around 25%, indicating that calculation of scatter from all voxels in the glass instead of using average values would not result in significant higher scatter values, especially since the difference between voxels located in the same window would be much smaller.

It should also be remembered that only single scattered X-rays are taken into account and that it is possible the majority of the scatter signal is from multiple scattered X-rays. By looking at the mean free path of the X-rays in borosilicate glass shown in figure 5.11(a) an estimation of the average number each X-ray incident on the detector was scattered can be made. Combining this with the partial mass attenuation coefficients in figure 5.11(b) and the total glass thickness of 6.4 cm it can be seen that although X-rays are very likely to interact before leaving the glass below 50 keV the photoelectric effect dominates here, so only a very small fraction of attenuated X-rays will undergo multiple scattering and leave the glass. Above 50 keV Compton scattering becomes the dominant interaction, but the mean free path also increases. Furthermore Compton scattering reduces the energy of the X-ray, decreasing the mean free path and making absorption in the subsequent interaction more likely. Additionally multiple scattered X-rays are more likely to change their direction and to no longer move towards the detector. In the end the process of multiple scattering is too complicated to get a quick estimate of and requires MC-calculations to accurately map. In order for the total scattering to be 30% of the total signal the scattering contribution of multiple scattered X-rays would have to be around 5 times the contribution of the single scattered X-rays, which does seem to be very high.

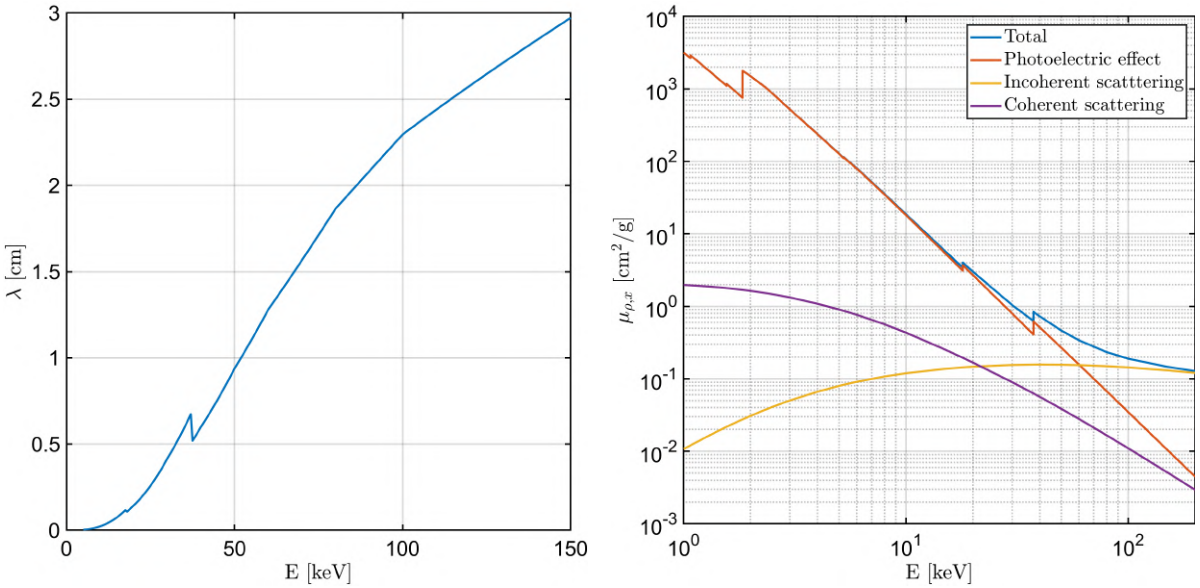

(a) Mean free path of X-rays in the borosilicate glass.

(b) Total and partial mass attenuation coefficients of borosilicate glass.

Figure 5.11: Mean free path of the X-rays in the flange windows and mass attenuation coefficients of the glass.

Lastly it is also possible that the FF and ISF approximations are not adequate for calculation of the scattering is this particular setup, although their widespread use in photon transport simulations would suggest otherwise. In all likelihood it is a combination of all possibilities discussed above. The best way to check the validity of the scatter results would be to use smaller voxels and to use more voxels to calculate the scatter contribution, but with the current hardware this is not feasible. A computer cluster with 12 cores was used to calculate the scatter from 5 voxels sheets of 35 by 35 0.2 mm cubic voxels with the calculation time taking almost 24 hours and also resulted in a lower scatter signal than expected. Accepting these results as valid introduces a big risk of underestimating the scatter even if a perfectly aligned collimator is used.

Since scattering is expected to be a big influence on detail visibility it was deemed sensible to find a second method to calculate the scatter contribution. The results discussed in the previous section showed that the relative scatter distribution is very constant in shape and is largely dependent on the intensity. The new idea was to fit a function to the scatter curve which could then be used to calculate the scatter in other situations. Finding the scatter contribution would require estimating the intensity of the primary signal as a result of only

the transmitted X-rays. The horizontal profiles in the previous section show the intensity dropping sharply on the left and right side of the peak. This drop was thought to be due to the steel cage blocking X-rays from directly reaching the detector and is as such an indication of the primary signal intensity. Furthermore it was assumed that due to many different scattering contributions and the continuous shape of the scattering DCSs the scatter signal itself should be a smooth curve with no jumps or discontinuities. By subtracting the average dark signal from the entire profile and then an estimation of the primary signal from the central peak the scatter signal could be approximated. Finding the correct estimation of the primary signal required using different estimations and seeing which one resulted in the most natural looking scatter curve. This method is not very scientific or even accurate, but since the exact value of the scatter was not that important and the goal was to obtain a general idea of the scatter contribution it was considered good enough. The estimation of the primary signal would also be needed to find the conversion factor from deposited energy to ADU since the simulated scatter was not accurate enough. After using different estimations of the primary signal it was found that subtracting 6100 ADU from the profile resulted in the most natural curve, although 6000 and 6200 were also valid choices. Subtracting this value from the central peak results in the curve shown in figure 5.12(a). A Gaussian function was used to make a fit to the curve, shown in figure 5.12(b). This function was not the overall best fit, but it was the most accurate in the center and the intensity outside the central region is not of interest, so inaccuracies in that part are of no importance. The one-dimensional fit was converted to a point-symmetric two-dimensional Gaussian function and was normalized with respect to the center value. This function can then be re-scaled with respect to the intensity of a transmission image to find an estimation of the scatter.

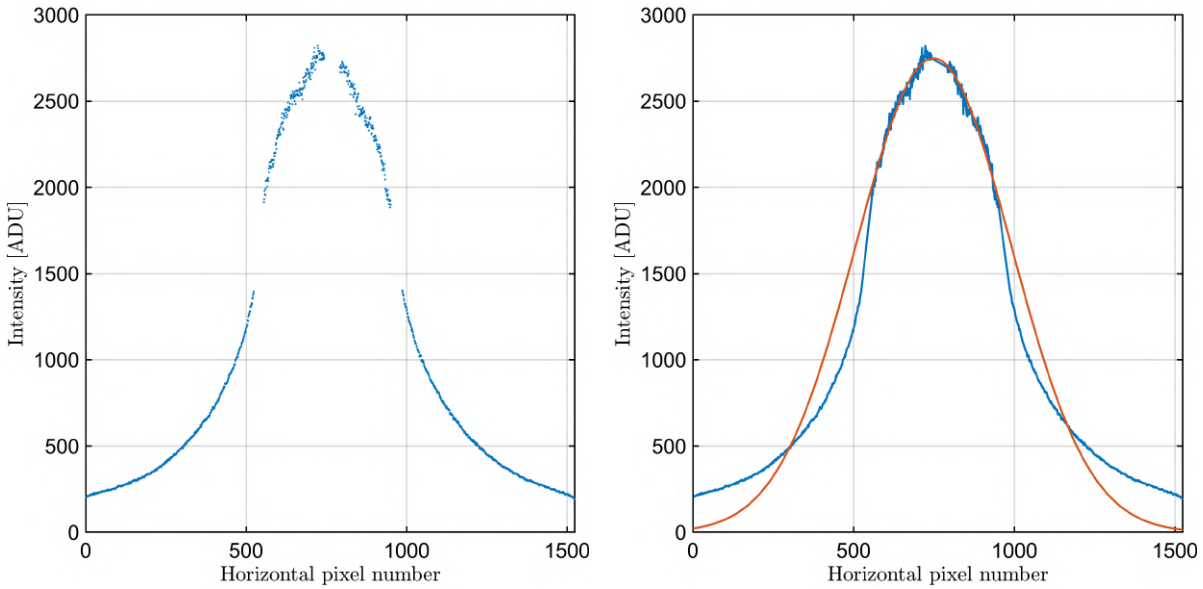

(a) Estimated measured scatter signal.

(b) Total and partial mass attenuation coefficients of borosilicate glass.

Figure 5.12: Estimated measured scatter signal and Gaussian fit to the curve. The fit is only accurate in the central part, but outside of this area the scatter signal is of no interest so inaccuracies there do not matter.

5.2.2. Simulation results

The choice was made to use the measurement with the empty cell and collimated beam as the benchmark for the simulation results. Any errors made in matching the simulation results to the measured results would then at least by applied consistently since the there is little change in experimental conditions when the cell is filled and they might be reduced by looking at relative intensities in the end. Using the estimation of a primary signal of 6100 ADU for the empty cell a conversion factor of approximately 0.145 ADU/keV is found. Applying this conversion factor to figure 5.10(a) results in the intensity image shown in figure 5.13(a). Estimating that the scatter contribution in the center would be around 30% the scatter function was re-scaled to the transmission image and added to it, resulting the the total intensity image in figure 5.13(b). Following this the image was blurred by convolution with the PSF and Gaussian noise was added based on a 50 SNR. For the empty cell there is no reason to use non-averaged images as there are no changes is time. Averaging

over 100 images results in the average intensity image shown in figure 5.13(c). Comparing it to the measured image in figure 5.6(a) shows the simulated image is relatively similar, although the detector defects are of course not included. In contrast to the measurements the blur and noise that degrade the image quality are exactly known which should in theory allow for optimal image restoration. When both the PSF and additive noise are known to a certain agree MathWorks advises to use Wiener deconvolution to improve the image quality, utilizing the `deconvwnr` function. The basic input arguments for this function are the blurred image, the PSF and the noise-to-signal ratio (NSR). Applying this function to the blurred image results in the image displayed in figure 5.13(d). Ideally the image in figure 5.13(b) would be retrieved, but it is clear that the blurred image is closer to the unblurred image than the deblurred one. Deconvolution results in an overall decrease in intensity and also introduces some artifacts at the edges. This indicates that even with perfect knowledge of the noise and PSF finding the undegraded image is not easy and that using the noisy image might be better. Deconvolution of the individual images before averaging does not produce noticeable different results.

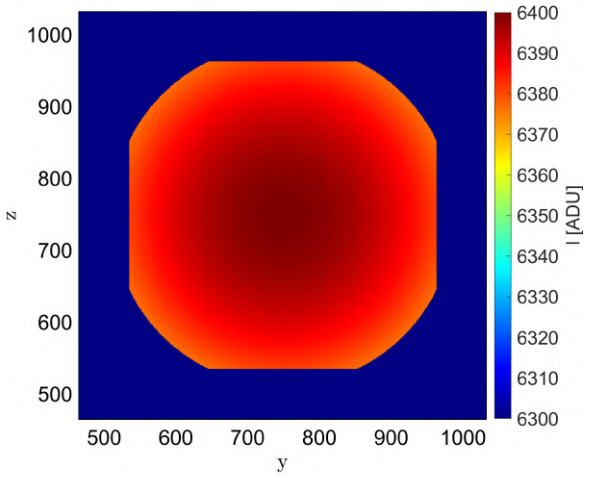

(a) Empty cell, transmission.

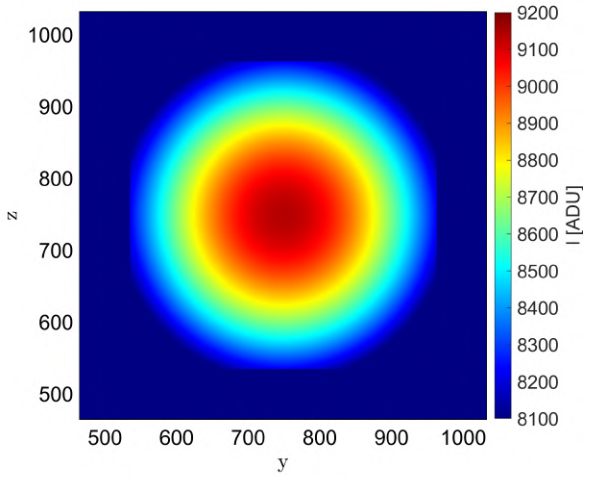

(b) Empty cell, transmission and scatter.

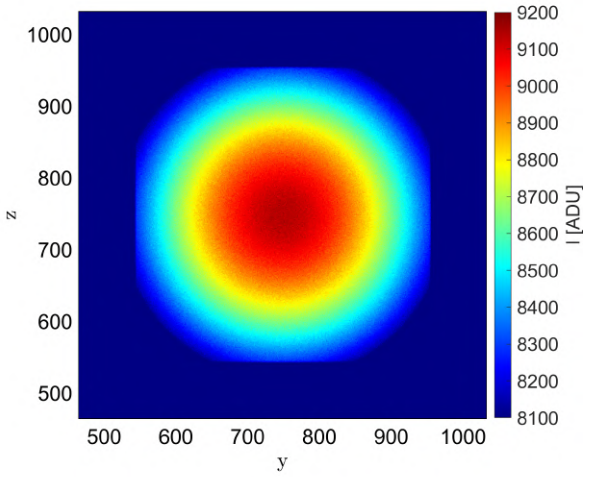

(c) Empty cell, average total intensity with blur and noise.

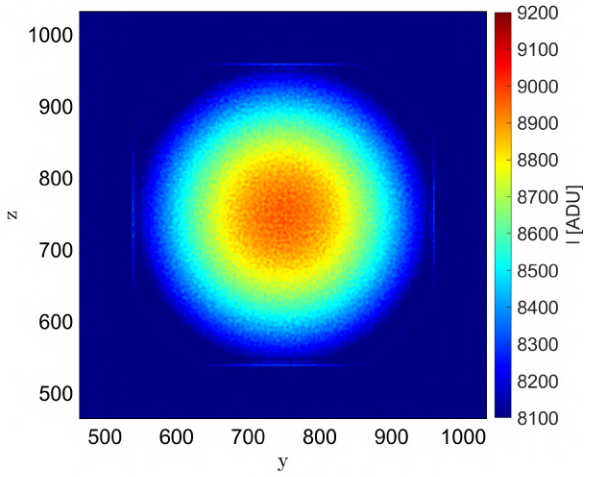

(d) Empty cell, average total intensity filtered and deblurred.

Figure 5.13: Simulation result of the empty cell. Figure 5.13(a) shows the transmission results. In figure 5.13(b) scatter has been added to the image, after which blur and noise are added in figure 5.13(c) and the average of 100 images is calculated. Finally an attempt is made to increase image quality by filtering and deblurring the image in figure 5.13(d)

An additional check to see if the blur and noise are applied correctly is to compare an instantaneous measured and simulated image. Figure 5.14(a) shows an instantaneous measured image of the empty cell with the simulated image in figure 5.14(b). Comparing the measured one with the averaged image in figure 5.6(a) confirms that averaging is efficient at reducing the noise in the image. The simulated image shows a finer noise distribution, which can be explained by the fact that for the simulated image the blur and noise are applied in sequence, while in reality part of the noise is also influenced by the blur. Applying a small Gaussian filter to image 5.14(b) seems to result in a image (figure 5.14(c)) that is more similar in noise to the measured one. The application of this filter is however somewhat arbitrary and not expected to significantly influence image quality so it was therefore decided to omit it from subsequent image processing.

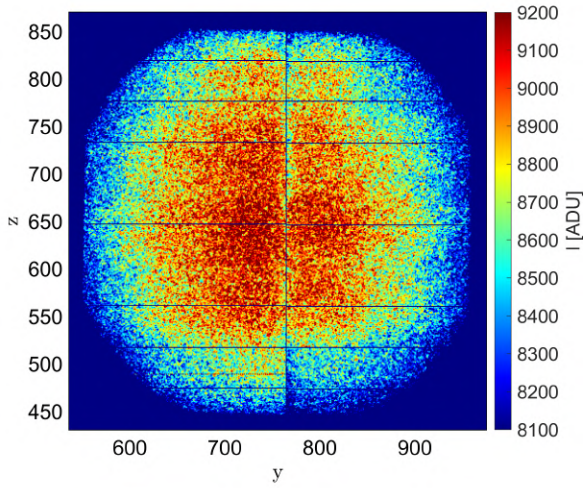

(a) Instantaneous measured image.

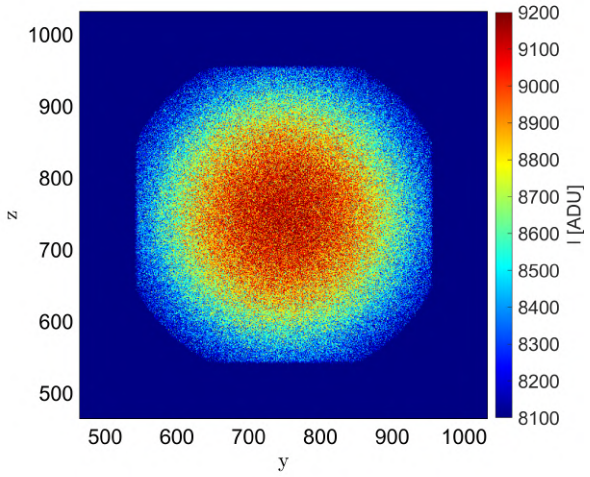

(b) Instantaneous simulated image.

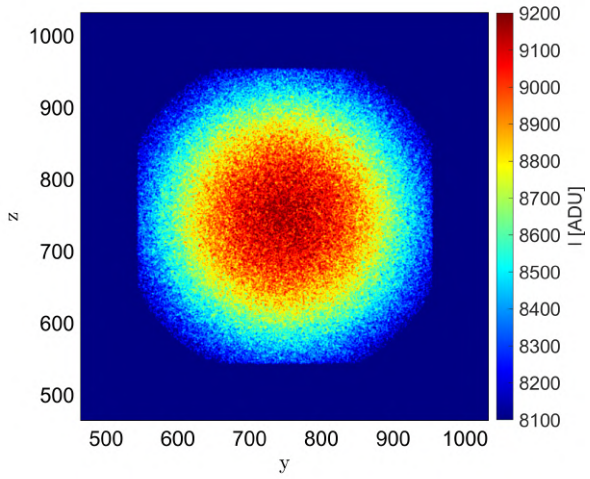

(c) Instantaneous simulated image with additional blur.

Figure 5.14: Simulation result of the empty cell. Figure 5.13(a) shows the transmission results. In figure 5.13(b) scatter has been added to the image, after which blur and noise are added in figure 5.13(c) and the average of 100 images is calculated. Finally an attempt is made to increase image quality by filtering and deblurring the image in figure 5.13(d).

$SC_{max\Delta\rho}$ region
The first experimental conditions applied to the SC R-23 are those corresponding to the $SC_{max\Delta\rho}$ region in table 3.1 and figure 3.3(a). In this region the density gradient is the steepest and the largest relative density differences for a ΔT of around 2.5 K can be expected. Figure 5.15(a) shows the average density of the R-23 in these conditions along the propagation direction of the X-rays. The colour scale has been inversed to better match the intensity images. The center of the image is relatively homogeneous in density with most of the density structures located at the edges, but even there they are only on the scale of 0.01 g/cm^3 indicating that even in the pure transmission image intensity differences will be very small. Figure 5.15(b) shows the transmission image of the fluid. By choosing the right limits for the colour scale considerable density structure can be revealed, but the difference between the minimum and maximum value is only 70 ADU. Using a conservative estimate of a 30% scatter fraction in the center figure 5.15(c) shows the total intensity image. As expected all detail of structures in the center of the image disappears, but around the edges still some details can be seen. To see the effect of the PSF on the image blur and noise are added separately. Looking at figure 5.15(d) it can be seen that blur does reduce the structure visibility, the effect is not very significant.

While for the empty cell averaging is the most logical choice it is not that easy for when the cell is filled with R-23. Although it will reduce the noise in the image the R-23 is not in steady-state and the structures change in time. Depending on the time-scale of the changes averaging over the instantaneous images or using an imaging frequency that is too low might result in them not being imaged. the detail visibility in instantaneous images should therefore also be studied. Figure 5.15(e) shows the blurred image with added noise, where a best-case scenario of a SNR of 50 has been used. In reality it will be lower, lying somewhere between 40 and 50. Unfortunately the noise removes all detail visibility, which is not unexpected. At a SNR of 50 the standard deviation in signal is just above 70 ADU and as such larger than the maximum difference in intensity due to density variations. Deconvolution of the image does not bring back some of the details as the noise is simply too large and destroys essentially all information on the density structure. A final possibility to increase image quality is to look at the relative intensity $\frac{I}{I_0}$ by dividing the image with the empty cell image. Figure 5.15(g) shows the relative intensity image of the noisy image of the filled cell and of the empty cell, while for figure 5.15(h) the deconvoluted images where used, but both regrettably result in only pure noise.

From these results it seems very unlikely that using just instantaneous images will produce useful results, at least at these experimental conditions. Averaging over multiple images however might still produce useful results. Figure 5.16(a) shows the average of 100 noisy images. Comparing it with the instantaneous image in figure 5.15(e) shows that in the average image still some details can be seen. Furthermore it is very similar to the image in figure 5.15(d) that only has been blurred. Deblurring the image does not seem to improve the image quality, similarly to the instantaneous images. Finally, looking at the relative intensities in figures 5.16(c) and 5.16(d) reveals that for the average images dividing by the empty cell image does bring back details. Furthermore it might even be argued that deconvolution of the images before division even increases the detail visibility in the relative image this time. These results would suggest that X-ray imaging of the SC fluid should be possible if enough images are used to calculate an average, but as mentioned earlier this is also very dependent on the time-scales of the fluid. It does seem likely that at least density differences located at the edges can be visualized.

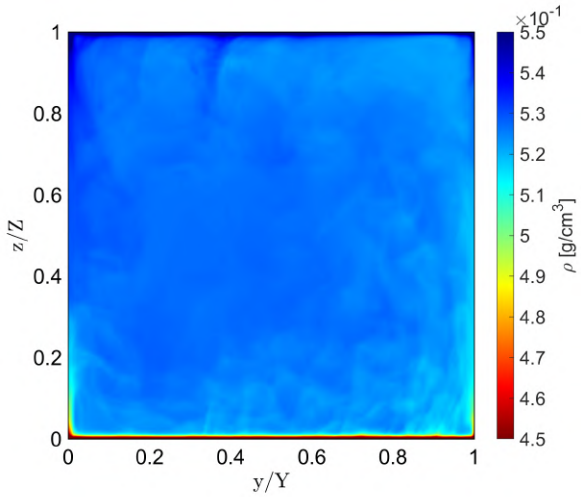

(a) Average density of the R-23.

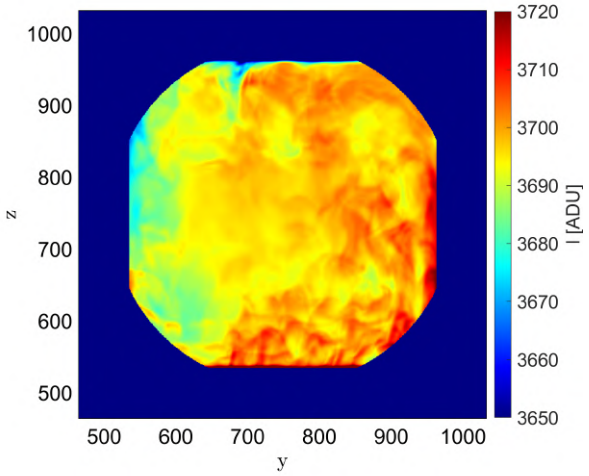

(b) Transmission image.

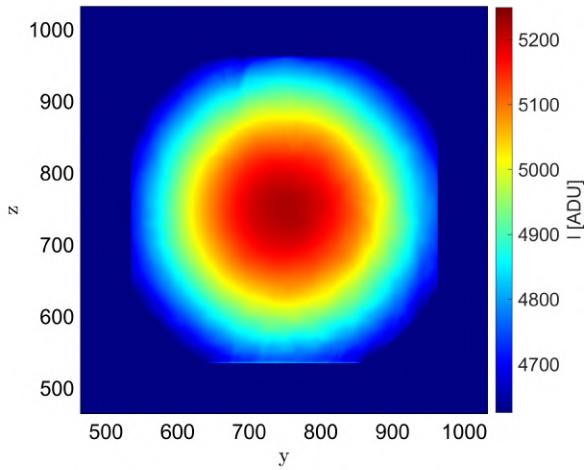

(c) Total intensity image.

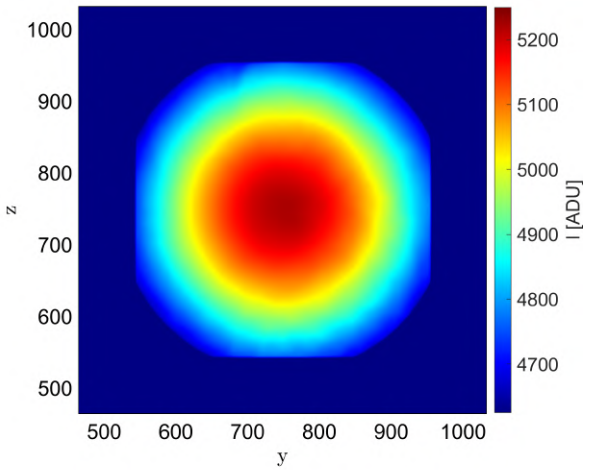

(d) Blurred image.

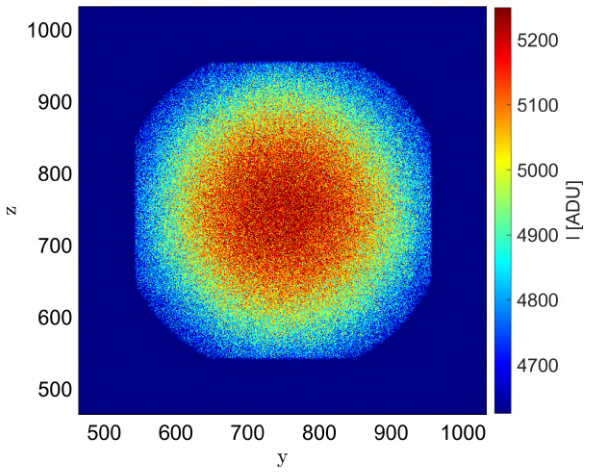

(e) Blurred, noisy image.

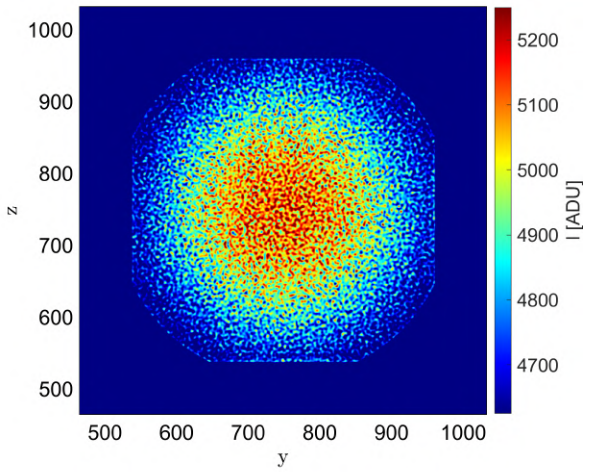

(f) Deconvoluted image.

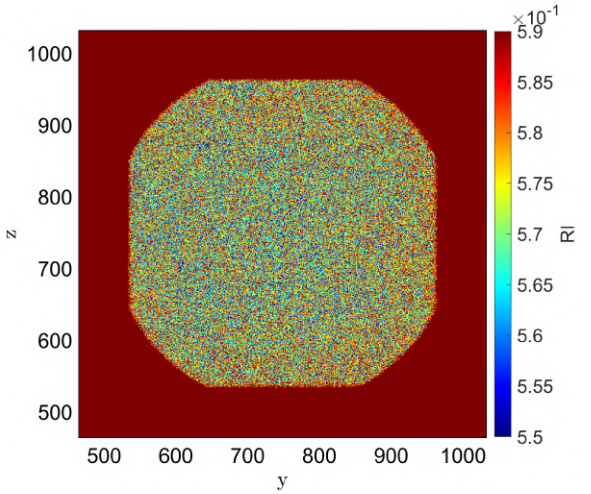

(g) Relative intensity

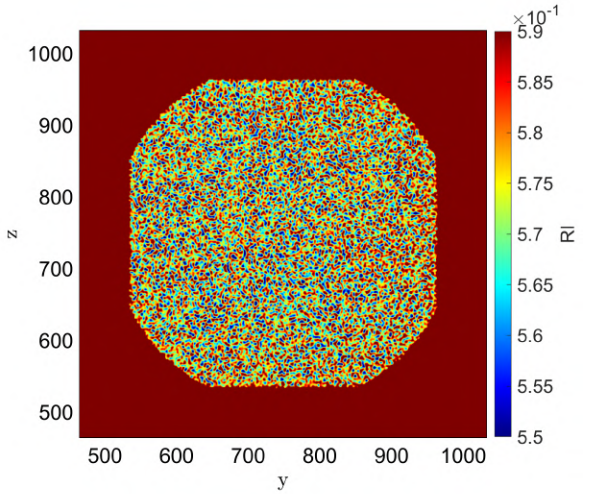

(h) Deconvoluted relative intensity.

Figure 5.15: Simulation results of the cell filled with R-23 in the $SC_{max\Delta\rho}$ region. Figure 5.15(a) shows the average density of the R-23 in these conditions and 5.15(b) the transmission image. In figures 5.15(c) and 5.15(d) scatter and blur are subsequently added to the image. Figure 5.15(e) displays an instantaneous image with noise added which is then deblurred in figure 5.15(f). Relative intensities with respect to the empty cell are displayed in figures 5.15(g) and 5.15(h), respectively without and with deconvolution.

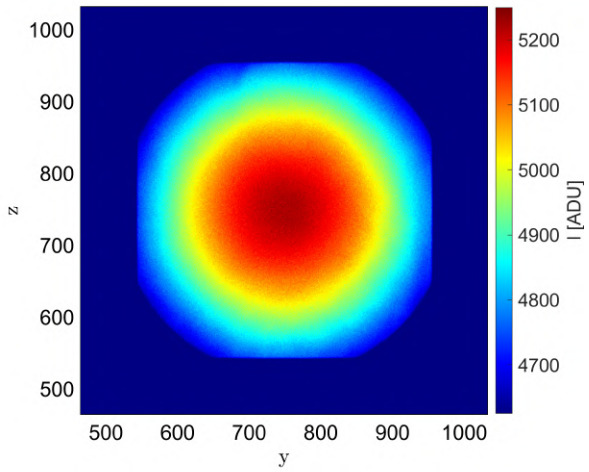

(a) Average blurred, noisy image.

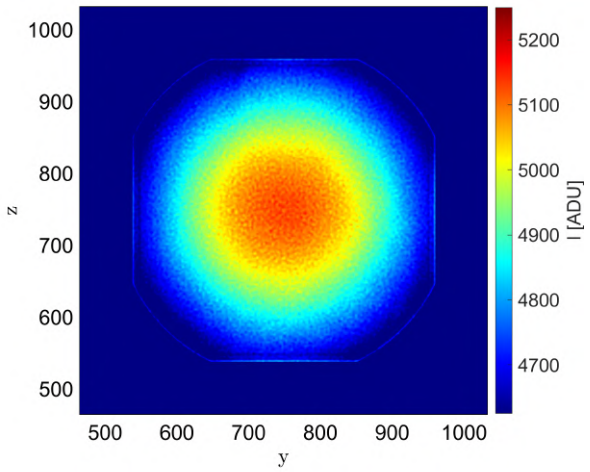

(b) Average deconvoluted image.

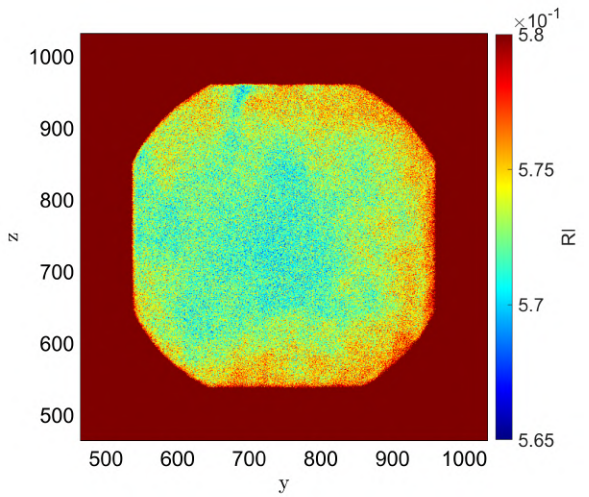

(c) Average relative intensity

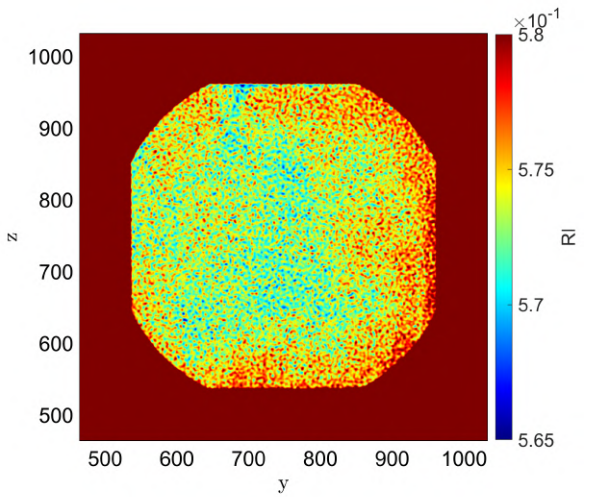

(d) Average deconvoluted relative intensity.

Figure 5.16: Averaged simulation results of the cell filled with R-23 in the $SC_{max\Delta\rho}$ region. Figure 5.16(a) shows the average of the noisy images which is deblurred in figure 5.16(b). Figures 5.16(c) and 5.16(d) show the relative intensities with respect to the empty cell results where the images have been deblurred prior to division in the second one.

SC_{tot} region
As it is expected that the largest density differences occur in the max $\Delta\rho$ region looking at the other experimental conditions in table 3.1 will in all likelihood only produce worse results. A better option might be to study the fluid in the conditions of the SC_{tot} region in 3.2. The temperature difference between the top and bottom plate is considerable larger than in the conditions of table 3.1 which should result in higher density differences. Figure 5.17 shows the same process for the instantaneous images as figure 5.15. As expected the intensity differences in figure 5.17(b) are larger due to the larger temperature difference. The first images are similar to the ones for the $SC_{max\Delta\rho}$ region, but the results are quite different after the noise has been added. Unlike the previous instantaneous images with noise some details still can be seen in these images. Furthermore the relative images are able to bring back some of the details from the transmission image in figure 5.17(b). Looking at the averaged images in figure 5.18 they show even better results. The relative intensity images in figures 5.18(c) and 5.18(d) are quite similar to the transmission image in figure 5.17(b), inspiring hope that it is possible to clearly visualize density structures at these experimental conditions.

Finally the image in figure 5.18(c) is used to calculate the average density using the method described in section 4.4. The result is shown in figure 5.19(b) and from comparing the two images it appears the used method results in a underestimation of the density. Comparing values at multiple points gives an average error of approximately 7%. Since the average density is underestimated it appears the average attenuation coefficient is overestimated. This might be explained by the fact that the method of Alles and Mudde [88] was developed for a homogeneous situation, where an X-ray spectrum is attenuated by a layer of a certain material after which it passes through the medium of interest. Between said medium and the detector there is no additional material. The RB cell filled with R-23 does not satisfy these conditions as there is a second glass window behind the R-23 resulting in further beam hardening. This additional hardening should result in a lower average attenuation coefficient and as such a higher average density, giving a better estimation of the real average density. Furthermore the energy response of the detector is not taken into account in the current method, while it has been used in the calculation of the intensities. As the detection efficiency of the detector can vary significantly for different X-ray energies it is likely the average attenuation coefficient of the detected X-rays deviates from the perfect detector one.

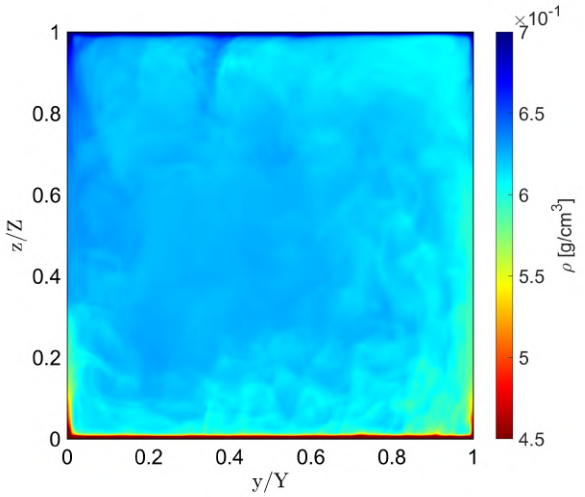

(a) Average density of the R-23.

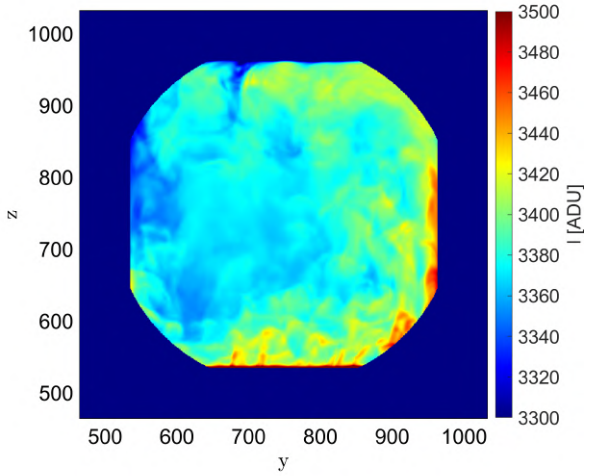

(b) Transmission image.

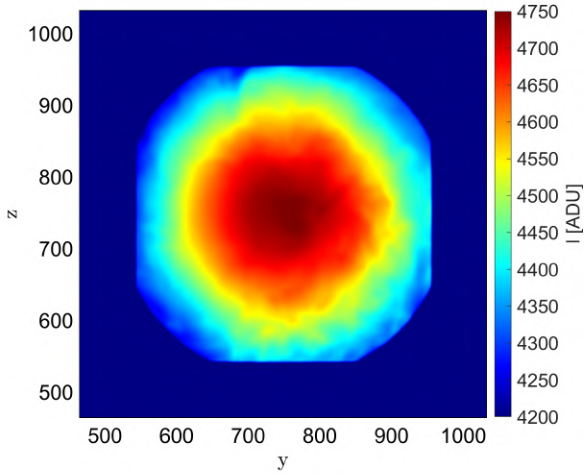

(c) Total intensity image.

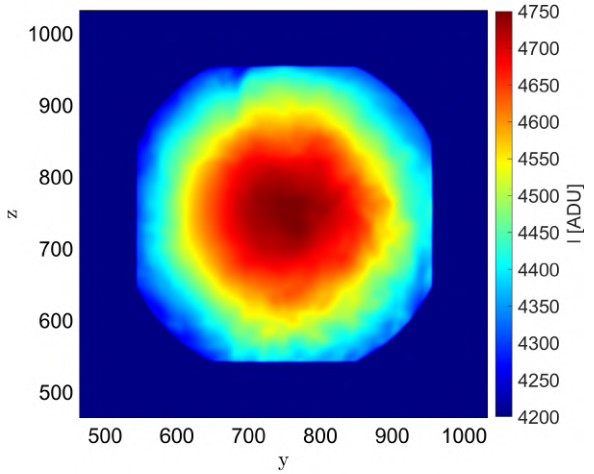

(d) Blurred image.

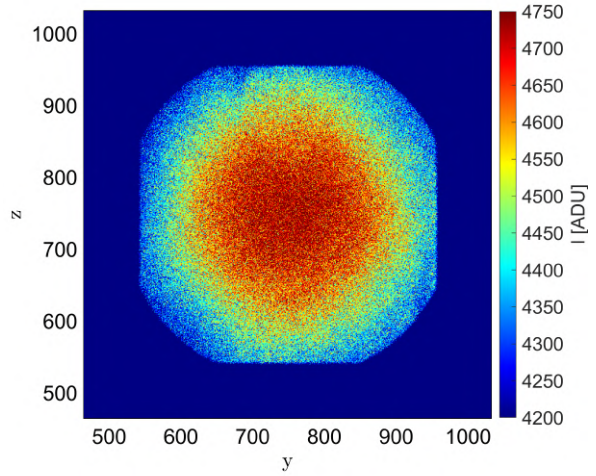

(e) Blurred, noisy image.

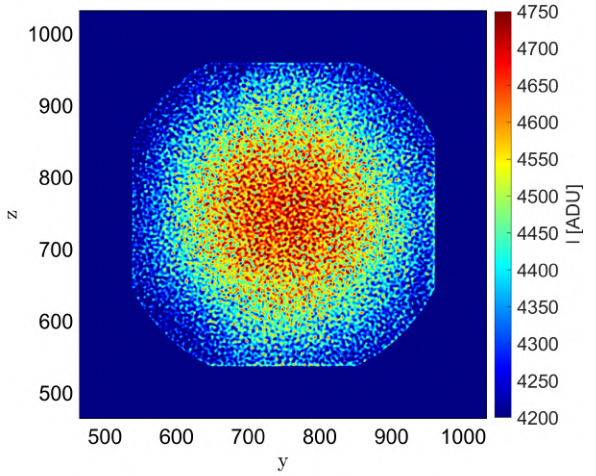

(f) Deconvoluted image.

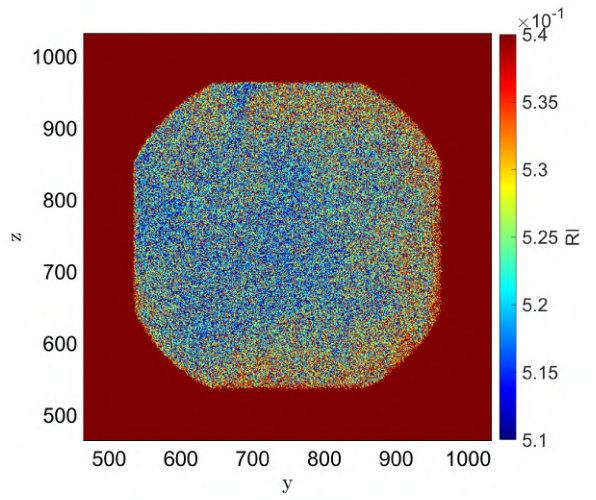

(g) Relative intensity

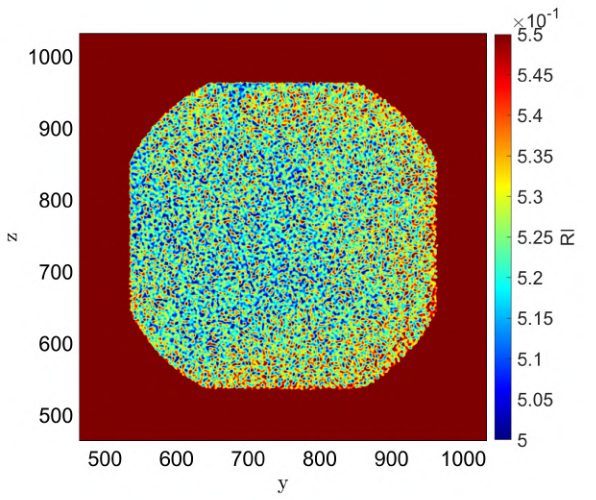

(h) Deconvoluted relative intensity.

Figure 5.17: Simulation results of the cell filled with R-23 in the SC_{tot} region. Figure 5.17(a) shows the average density of the R-23 in these conditions and 5.17(b) the transmission image. In figures 5.17(c) and 5.17(d) scatter and blur are subsequently added to the image. Figure 5.17(e) displays an instantaneous image with noise added which is then deblurred in figure 5.17(f). Relative intensities with respect to the empty cell are displayed in figures 5.17(g) and 5.17(h), respectively without and with deconvolution.

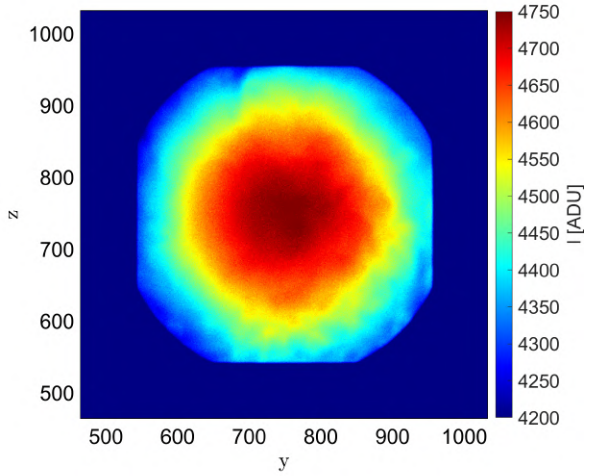

(a) Average blurred, noisy image.

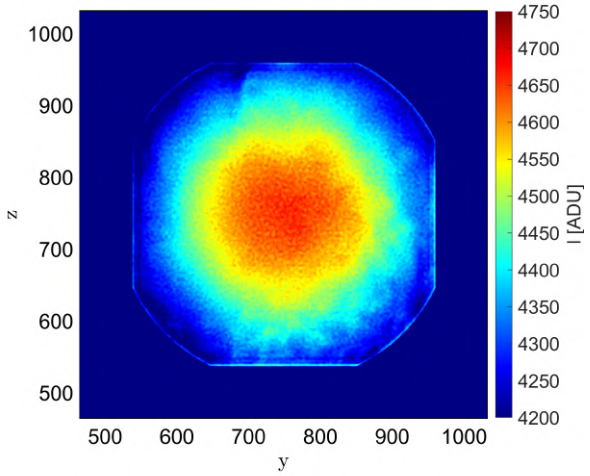

(b) Average deconvoluted image.

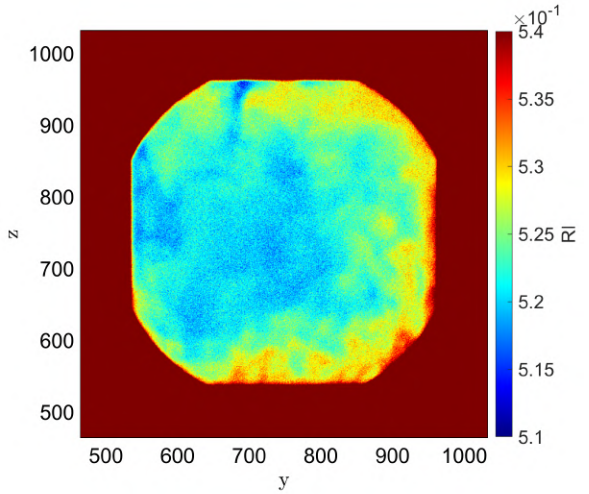

(c) Average relative intensity

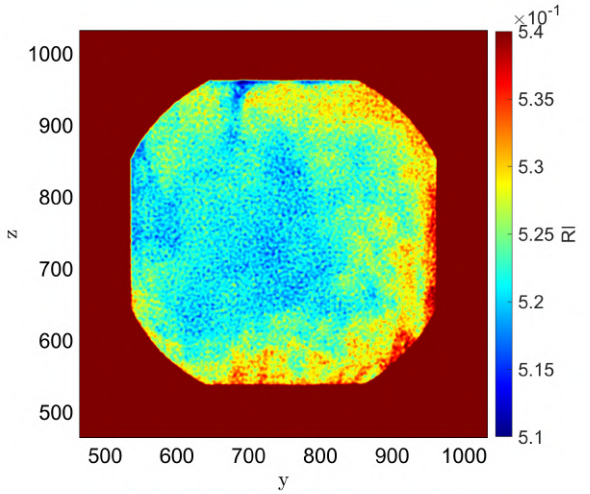

(d) Average deconvoluted relative intensity.

Figure 5.18: Averaged simulation results of the cell filled with R-23 in the SC_{tot} region. Figure 5.18(a) shows the average of the noisy images which is deblurred in figure 5.18(b). Figures 5.18(c) and 5.18(d) show the relative intensities with respect to the empty cell results where the images have been deblurred prior to division in the second one.

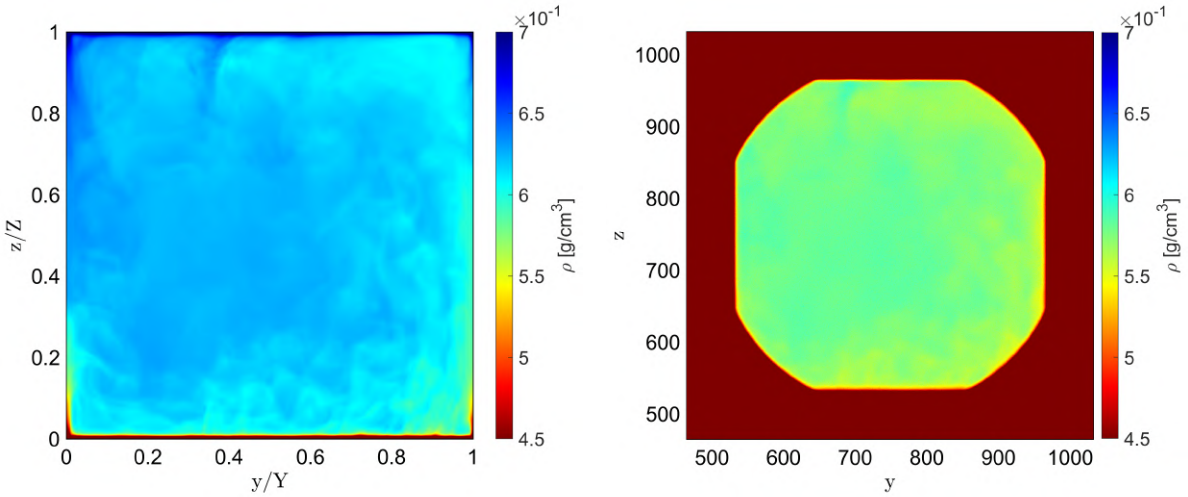

(a) Average density of the R-23.

(b) Calculated average density of the R-23.

Figure 5.19: The actual average density and the one calculated using the empty and full cell images and the method described in section 4.4.

6

Conclusions & Recommendations

6.1. Conclusions

An algorithm was developed to simulate the X-ray imaging of supercritical fluoroform in a specially designed Rayleigh-Bénard cell as the actual experiments could not be performed due to the COVID-19 pandemic. This algorithm consists of three main parts: X-ray production, X-ray transport and finally detection. For the production an analytical model is used that is able to calculate the number of X-rays produced per incident electron within 2% of MC-calculated results. The X-ray transport is split into two sections treating X-ray transmission through and scattering from a voxelated object respectively. The transmission is calculated using the NIST X-com database, the Lambert-Beer law and Bragg's additive law. Scattering is simulated using a first-order approximation in combination with the form-factor and incoherent scattering function approximations. Regarding the X-ray detection many of the important properties of the simulated detector are unfortunately unknown, which makes developing a purely analytical detection model quite complicated. Two different approaches were attempted, with the first one based on the properties of a different detector produced by the same manufacturer. The second method made use of the saturation dose specified on the datasheet of the detector. Unfortunately both methods were unable to produce accurate results, so a third method was adopted in the end that used the results of measurements that had been done prior to the lockdown. Finally a beam hardening model was developed in order to calculate average densities using a modified version of the Lambert-Beer law.

6.2. Recommendations

Experiments
Simulations

Bibliography

[1] Anthony A Clifford and John R Williams. Introduction to supercritical fluids and their applications. In *Supercritical Fluid Methods and Protocols*, pages 1–16. Springer, 2000.

[2] Gerd Brunner. Applications of Supercritical Fluids. *Annual Review of Chemical and Biomolecular Engineering*, 1(1):321–342, jun 2010. ISSN 1947-5438. doi: 10.1146/annurev-chembioeng-073009-101311.

[3] Department of Trade and Industry. Supercritical steam cycles for power generation applications. January 1999.

[4] Yoshiaki Oka and Sei-Ichi Koshizuka. Concept and design of a supercritical-pressure, direct-cycle light water reactor. *Nuclear Technology*, 103(3):295–302, 1993.

[5] ME Shitsman. Impairment of the heat transmission at supercritical pressures(heat transfer process examined during forced motion of water at supercritical pressures). *High temperature*, 1:237–244, 1963.

[6] H. S. Swenson, J. R. Carver, and C. R. Kakarala. Heat Transfer to Supercritical Water in Smooth-Bore Tubes. *Journal of Heat Transfer*, 87(4):477–483, 11 1965. ISSN 0022-1481. doi: 10.1115/1.3689139. URL `https://doi.org/10.1115/1.3689139`.

[7] J. W. Ackerman. Pseudoboiling Heat Transfer to Supercritical Pressure Water in Smooth and Ribbed Tubes. *Journal of Heat Transfer*, 92(3):490–497, 08 1970. ISSN 0022-1481. doi: 10.1115/1.3449698. URL `https://doi.org/10.1115/1.3449698`.

[8] ORNATSKI. AP, SI Kalachev, and GLUSHCHE. LF. Heat-transfer with rising and falling flows of water in tubes of small diameter at supercritical pressures. *Thermal Engineering*, 18(5):137–141, 1971.

[9] K Yamagata, K Nishikawa, S Hasegawa, T Fujii, and S Yoshida. Forced convective heat transfer to supercritical water flowing in tubes. *International Journal of Heat and Mass Transfer*, 15(12):2575 – 2593, 1972. ISSN 0017-9310. doi: https://doi.org/10.1016/0017-9310(72)90148-2. URL `http://www.sciencedirect.com/science/article/pii/0017931072901482`.

[10] JD Jackson and J Fewster. Forced convection data for supercritical pressure fluids. *HTFS*, 21540, 1975.

[11] John E. Kelly. Generation IV International Forum: A decade of progress through international cooperation. *Progress in Nuclear Energy*, 77:240–246, 2014. ISSN 01491970. doi: 10.1016/j.pnucene.2014.02.010. URL `http://dx.doi.org/10.1016/j.pnucene.2014.02.010`.

[12] Jacopo Buongiorno and P MacDonald. Supercritical water reactor (scwr). *Progress Report for the FY-03 Generation-IV R&D Activities for the Development of the SCWR in the US, INEEL/Ext-03-03-01210, INEEL, USA, September*, 2003.

[13] Mohammad Mizanur Rahman, Ji Dongxu, Nusrat Jahan, Massimo Salvatores, and Jiyun Zhao. Design concepts of supercritical water-cooled reactor (SCWR) and nuclear marine vessel: A review. *Progress in Nuclear Energy*, 124, 2020. ISSN 01491970. doi: 10.1016/j.pnucene.2020.103320. URL `https://doi.org/10.1016/j.pnucene.2020.103320`.

[14] Ian H. Bell, Jorrit Wronski, Sylvain Quoilin, and Vincent Lemort. Pure and pseudo-pure fluid thermophysical property evaluation and the open-source thermophysical property library coolprop. *Industrial & Engineering Chemistry Research*, 53(6):2498–2508, 2014. doi: 10.1021/ie4033999. URL `http://pubs.acs.org/doi/abs/10.1021/ie4033999`.

[15] Jung Yul Yoo. The turbulent flows of supercritical fluids with heat transfer. *Annual review of fluid mechanics*, 45:495–525, 2013.

[16] Valentina Valori, Gerrit E Elsinga, Martin Rohde, Jerry Westerweel, and Tim HJJ van Der Hagen. Particle image velocimetry measurements of a thermally convective supercritical fluid. *Experiments in Fluids*, 60(9):143, 2019.

[17] E. W. Lemmon, I.H. Bell, M. L. Huber, and M. O. McLinden. NIST Standard Reference Database 23: Reference Fluid Thermodynamic and Transport Properties-REFPROP, Version 10.0, National Institute of Standards and Technology, 2018. URL `https://www.nist.gov/srd/refprop`.

[18] G. E. Elsinga, B. W. Van Oudheusden, F. Scarano, and D. W. Watt. Assessment and application of quantitative schlieren methods: Calibrated color schlieren and background oriented schlieren. *Experiments in Fluids*, 36(2):309–325, 2004. ISSN 07234864.

[19] Márton Balaskó, László Horváth, Ákos Horváth, Attila Kiss, and Attila Aszódi. Study on the properties of supercritical water flowing in a closed loop using dynamic neutron radiography. *Physics Procedia*, 43: 254–263, 2013. ISSN 18753892. doi: 10.1016/j.phpro.2013.03.029. URL `http://dx.doi.org/10.1016/j.phpro.2013.03.029`.

[20] Florentina Maxim, Cristian Contescu, Pierre Boillat, Bojan Niceno, Konstantinos Karalis, Andrea Testino, and Christian Ludwig. Visualization of supercritical water pseudo-boiling at Widom line crossover. *Nature Communications*, 10(1), 2019. ISSN 20411723. doi: 10.1038/s41467-019-12117-5.

[21] Tatsuhiko Kawamoto, Masami Kanzaki, Kenji Mibe, Kyoko N. Matsukage, and Shigeaki Ono. Separation of supercritical slab-fluids to form aqueous fluid and melt components in subduction zone magmatism. *Proceedings of the National Academy of Sciences of the United States of America*, 109(46):18695–18700, 2012. ISSN 00278424. doi: 10.1073/pnas.1207687109.

[22] Kuldeep Chaudhary, Eric J. Guiltinan, M. Bayani Cardenas, Jessica A. Maisano1, Richard A. Ketcham, and Philip C. Bennett. Wettability measurement under high P-T conditions using X-ray imaging with application to the brine-supercritical CO2 system. *Geochemistry, Geophysics, Geosystems*, 16(9):2858–2864, 2015. doi: 10.1002/2015GC005936.

[23] Burton L Henke, Eric M Gullikson, and John C Davis. X-ray interactions: photoabsorption, scattering, transmission and reflection e= 50-30,000 ev, z= 1-92. *Atomic data and nuclear data tables*, 54(2), 1993.

[24] Rolf Behling. *Modern Diagnostic X-Ray Sources: Technology, Manufacturing, Reliability*. CRC Press, Boca Raton, 2015. ISBN 9781482241334. doi: 10.1201/b18655.

[25] Bettyann Kevles. *Naked to the bone: medical imaging in the twentieth century*. Rutgers University Press, 1997.

[26] Faiz M. Khan and John P. Gibbons. *The Physics of Radiation Therapy*. Lippincott Williams \& Wilkins, 5th edition, 2014. ISBN 9781451182453.

[27] W.R. Hendee. *Medical Radiation Physics*. Year Book Medical Publishers, 2nd edition, 1979. ISBN 9780815142393.

[28] Sarah Abdulla. X-ray tube diagram. URL `https://www.radiologycafe.com/radiology-trainees/frcr-physics-notes/production-of-x-rays`. Last accessed 2020-12-09.

[29] D. Gonzales, B. Cavness, and S. Williams. Angular distribution of thick-target bremsstrahlung produced by electrons with initial energies ranging from 10 to 20-keV incident on Ag. *Physical Review A*, 84(5), 2011.

[30] Carl A. Carlsson and Gudrun Alm Carlsson. Basic physics of X-ray imaging. Technical report, Department of Radiation Physics, Faculty of Health Sciences, Linköping University, 1996.

[31] J. Kenneth Shultis and Richard E. Faw. *Fundamentals of Nuclear Science and Engineering*. Marcel Dekker, 2002. ISBN 9781439894088. doi: 10.1201/b12824.

[32] M.J. Berger, J.H. Hubbell, S.M. Seltzer, J. Chang, J.S. Coursey, R. Sukumar, D.S. Zucker, and K. Olsen. Xcom: Photon cross section database (version 1.5). 2010. URL `https://www.nist.gov/pml/xcom-photon-cross-sections-database`. Last accessed 14-12-2020.

[33] J. H. Hubbell, Wm J. Veigele, E. A. Briggs, R. T. Brown, D. T. Cromer, and R. J. Howerton. Atomic Form Factors, Incoherent Scattering Functions, and Photon Scattering Cross Sections. *Journal of Physical and Chemical Reference Data*, 4(3):471—-538, 1975. ISSN 15297845. doi: 10.1063/1.555554.

[34] N. Freud, P. Duvauchelle, S. A. Pistrui-Maximean, J. M. Létang, and D. Babot. Deterministic simulation of first-order scattering in virtual X-ray imaging. *Nuclear Instruments and Methods in Physics Research, Section B: Beam Interactions with Materials and Atoms*, 222(1-2):285–300, 2004. ISSN 0168583X. doi: 10.1016/j.nimb.2004.01.001.

[35] Beevil. Light spreading in the scintillator material leads to loss of resolution in indirect detectors which direct detectors do not experience, 23-07-2017. URL `https://commons.wikimedia.org/w/index.php?curid=61264494`. Last accessed 13-01-2021.

[36] Jan Jakubek. Data processing and image reconstruction methods for pixel detectors. *Nuclear Instruments and Methods in Physics Research, Section A: Accelerators, Spectrometers, Detectors and Associated Equipment*, 576(1):223–234, 2007. ISSN 01689002. doi: 10.1016/j.nima.2007.01.157.

[37] John R. Williams, Anthony A. Clifford, and Salim H.R. Al-Saidi. Supercritical fluids and their applications in biotechnology and related areas. *Molecular Biotechnology*, 22(3):263–286, 2002. ISSN 10736085. doi: 10.1385/MB:22:3:263.

[38] G. G. Simeoni, T. Bryk, F. A. Gorelli, M. Krisch, G. Ruocco, M. Santoro, and T. Scopigno. The Widom line as the crossover between liquid-like and gas-like behaviour in supercritical fluids. *Nature Physics*, 6(7):503–507, 2010. ISSN 17452481. doi: 10.1038/nphys1683.

[39] Min Young Ha, Tae Jun Yoon, Tsvi Tlusty, Yongseok Jho, and Won Bo Lee. Widom Delta of Supercritical Gas-Liquid Coexistence. *Journal of Physical Chemistry Letters*, 9(7):1734–1738, 2018. ISSN 19487185. doi: 10.1021/acs.jpclett.8b00430.

[40] D.T. Banuti. Crossing the widom-line – supercritical pseudo-boiling. *The Journal of Supercritical Fluids*, 98:12 – 16, 2015. ISSN 0896-8446. doi: https://doi.org/10.1016/j.supflu.2014.12.019. URL `http://www.sciencedirect.com/science/article/pii/S0896844614004306`.

[41] Valentina Valori. *Rayleigh-Bénard convection of a supercritical fluid: PIV and heat transfer study*. PhD thesis, TU Delft, 2018. URL `http://repository.tudelft.nl/`.

[42] Evert Wagner. *Radiation Safety Pertaining to the X Ray Tomographic Scanner setup of ChemE TP, located at RID*, 2018.

[43] Evert Wagner. *User's manual X-ray high speed tomography setup*, 2019.

[44] A Omar, P Andreo, and G Poludniowski. Matlab implementation of an analytical model for the emission of x rays from an x-ray tube. 2020.

[45] Artur Omar, Pedro Andreo, and Gavin Poludniowski. A model for the emission of K and L x rays from an x-ray tube. *Nuclear Instruments and Methods in Physics Research, Section B: Beam Interactions with Materials and Atoms*, 437:36–47, 2018. ISSN 0168583X. doi: 10.1016/j.nimb.2018.10.026. URL `https://doi.org/10.1016/j.nimb.2018.10.026`.

[46] Artur Omar, Pedro Andreo, and Gavin Poludniowski. A model for the energy and angular distribution of x rays emitted from an x-ray tube. Part I. Bremsstrahlung production. *Medical Physics*, 47(10):4763–4774, 2020. ISSN 00942405. doi: 10.1002/mp.14359.

[47] Artur Omar, Pedro Andreo, and Gavin Poludniowski. A model for the energy and angular distribution of x rays emitted from an x-ray tube. Part II. Validation of x-ray spectra from 20 to 300 kV. *Medical Physics*, 47(9):4005–4019, 2020. ISSN 0094-2405. doi: 10.1002/mp.14360.

[48] Artur Omar, Pedro Andreo, and Gavin Poludniowski. Performance of different theories for the angular distribution of bremsstrahlung produced by kev electrons incident upon a target. *Radiation Physics and Chemistry*, 148:73 – 85, 2018. ISSN 0969-806X. doi: https://doi.org/10.1016/j.radphyschem.2018.02.009. URL `http://www.sciencedirect.com/science/article/pii/S0969806X17312525`.

[49] Philippe Duvauchelle, Nicolas Freud, Valérie Kaftandjian, and Daniel Babot. Computer code to simulate X-ray imaging techniques. *Nuclear Instruments and Methods in Physics Research, Section B: Beam Interactions with Materials and Atoms*, 170(1):245–258, 2000. ISSN 0168583X. doi: 10.1016/S0168-583X(00)00185-3.

[50] Lili Zhou, K S Clifford Chao, and Jenghwa Chang. Fast polyenergetic forward projection for image formation using OpenCL. *Medical Physics*, 39(11):6745–6756, 2012. doi: https://doi.org/10.1118/1.4758062. URL `https://aapm.onlinelibrary.wiley.com/doi/abs/10.1118/1.4758062`.

[51] Qian Cao, Alejandro Sisniega, Michael Brehler, J. Webster Stayman, John Yorkston, Jeffrey H. Siewerdsen, and Wojciech Zbijewski. Modeling and Evaluation of a High-Resolution CMOS Detector for Cone-Beam CT of the Extremities Qian. *Medical Physics*, 45(1):114–130, 2018. doi: 10.1002/mp.12654. URL `https://europepmc.org/articles/PMC5774240`.

[52] N. Freud, P. Duvauchelle, J. M. Létang, and D. Babot. Fast and robust ray casting algorithms for virtual X-ray imaging. *Nuclear Instruments and Methods in Physics Research, Section B: Beam Interactions with Materials and Atoms*, 248(1):175–180, 2006. ISSN 0168583X. doi: 10.1016/j.nimb.2006.03.009.

[53] J. W. R. Peeters. personal communication.

[54] Robert L. Siddon. Fast calculation of the exact radiological path for a three-dimensional CT array. *Medical Physics*, 12(2):252–255, 1985. doi: https://doi.org/10.1118/1.595715.

[55] Filip Jacobs, Erik Sundermann, Bjorn De Sutter, Mark Christiaens, and Ignace Lemahieu. A fast algorithm to calculate the exact radiological path through a pixel or voxel space. *Journal of Computing and Information Technology*, 6(1):89–94, 1998. ISSN 18463908.

[56] Huaxia Zhao and Andrew J. Reader. Fast ray-tracing technique to calculate line integral paths in voxel arrays. In *2003 IEEE Nuclear Science Symposium. Conference Record (IEEE Cat. No. 03CH37515)*, volume 4, pages 2808–2812, 2003. ISBN 0780382579. doi: 10.1109/nssmic.2003.1352469.

[57] Dermott E. Cullen. EPICS2017: April 2019 Status Report. Technical report, IAEA-NDS, 2019.

[58] B. R. Kerur, M. T. Lagare, and R. Nathuram. Non-validity of Bragg's additivity law for rare-earth compounds. *Radiation Physics and Chemistry*, 75(1):7–13, 2006. ISSN 0969806X. doi: 10.1016/j.radphyschem.2005.02.009.

[59] S B Kaginelli and B R Kerur. Studies of Bragg's Additivity Law Near Ledges. In *Proceedings of the NSRP*, 19, 2011.

[60] Cody Crewson. *AN EXPERIMENTAL RE-EVALUATION OF PHOTON MASS ATTENUATION COEFFICIENTS*. PhD thesis, University of Saskatchewan, 2013.

[61] H. Zaidi. Comparative evaluation of photon cross-section libraries for materials of interest in PET Monte Carlo simulations. *IEEE Transactions on Nuclear Science*, 47(6):2722–2735, 2000. ISSN 00189499. doi: 10.1109/23.901179.

[62] Guillaume Landry, Mark J. Rivard, Jeffrey F. Williamson, and Frank Verhaegen. Monte carlo techniques in radiation therapy. In Frank Verhaegen Joao Seco, editor, *Monte Carlo Methods and Applications for Brachytherapy Dosimetry and Treatment planning*, IMAGING IN MEDICAL DIAGNOSIS AND THERAPY, chapter 9, pages 125–144. CRC Press, 2015. ISBN 13: 978-1-4665-0792-0.

[63] Min Cheol Han, Han Sung Kim, Maria Grazia Pia, Tullio Basaglia, Matej Batic, Gabriela Hoff, Chan Hyeong Kim, and Paolo Saracco. Validation of Cross Sections for Monte Carlo Simulation of the Photoelectric Effect. *IEEE Transactions on Nuclear Science*, 63(2):1117–1146, 2016. ISSN 00189499. doi: 10.1109/TNS.2016.2521876.

[64] Min Cheol Han, Maria Grazia Pia, Paolo Saracco, and Tullio Basaglia. First Assessment of ENDF/B-VIII and EPICS atomic data libraries. *IEEE Transactions on Nuclear Science*, 65(8):2268–2278, 2018. ISSN 00189499. doi: 10.1109/TNS.2018.2849328.

[65] Tullio Basaglia, Maria Grazia Pia, and Paolo Saracco. Evolutions in Photoelectric Cross Section Calculations and Their Validation. *IEEE Transactions on Nuclear Science*, 67(3):492–501, 2020. ISSN 15581578. doi: 10.1109/TNS.2020.2971173.

[66] Dermott E. Cullen. A survey of photon cross section data for use in epics2017. IAEA Nuclear Data Services. Technical report, IAEA-NDS, 2018.

[67] Glenn F. Knoll. *Radiation Detection and Measurement*, chapter 8. John Wiley & Sons, Inc., 4th edition, 2010. ISBN 978-0-470-13148-0.

[68] P. Dorenbos, J. T.D. de Haas, and C. W.V. van Eijk. Non-Proportionality in the Scintillation Response and the Energy Resolution Obtainable with Scintillation Crystals. *IEEE Transactions on Nuclear Science*, 42 (6):2190–2202, 1995. ISSN 15581578. doi: 10.1109/23.489415.

[69] Agnieszka Syntfeld-Kaẓuch, Łukasz Świderski, Wiesław Czarnacki, Michał Gierlik, Włodzimierz Klamra, Marek Moszyński, and Paul Schotanus. Non-proportionality and energy resolution of CsI(Tl). *IEEE Transactions on Nuclear Science*, 54(5):1836–1841, 2007. ISSN 00189499. doi: 10.1109/TNS.2007.906168.

[70] Marco Endrizzi, Piernicola Oliva, Bruno Golosio, and Pasquale Delogu. CMOS APS detector characterization for quantitative X-ray imaging. *Nuclear Instruments and Methods in Physics Research, Section A: Accelerators, Spectrometers, Detectors and Associated Equipment*, 703:26–32, 2013. ISSN 01689002. doi: 10.1016/j.nima.2012.11.080. URL http://dx.doi.org/10.1016/j.nima.2012.11.080.

[71] Amit Jain, Daniel R. Bednarek, and Stephen Rudin. Experimental and theoretical performance analysis for a CMOS-based high resolution image detector. In *Medical Imaging 2014: Physics of Medical Imaging*, volume 9033, 2014. ISBN 9780819498267. doi: 10.1117/12.2043053.

[72] Mikael Kördel. *A Physical X-Ray Scintillator Detector Model for CBCT Imaging Applications*. PhD thesis, KTH Royal Institute of Technology, 2014.

[73] Rongqing Hui. Chapter 4 - photodetectors. In Rongqing Hui, editor, *Introduction to Fiber-Optic Communications*, pages 125–154. Academic Press, 2020. ISBN 978-0-12-805345-4. doi: https://doi.org/10.1016/B978-0-12-805345-4.00004-4. URL https://www.sciencedirect.com/science/article/pii/B9780128053454000044.

[74] R Celestre, M Rosenberger, and G Notni. A novel algorithm for bad pixel detection and correction to improve quality and stability of geometric measurements. *Journal of Physics: Conference Series*, 772:012002, nov 2016. doi: 10.1088/1742-6596/772/1/012002. URL https://doi.org/10.1088/1742-6596/772/1/012002.

[75] J. H. Hubbell and S. M. Seltzer. Tables of X-Ray Mass Attenuation Coefficients and Mass Energy-Absorption Coefficients from 1 keV to 20 MeV for Elements Z = 1 to 92 and 48 Additional Substances of Dosimetric Interest. Technical report, National Institute of Standards and Technology, Gaithersburg, MD, 1995. URL https://www.nist.gov/pml/x-ray-mass-attenuation-coefficients.

[76] J. H. Hubbell. Photon Mass Attenuation and Energy-Absorption Coefficients from 1 keV to 20 MeV. *The International Journal Of Applied Radiation And Isotopes*, 33(11):1269–1290, 1982. ISSN 0020708X. doi: 10.1016/0020-708X(82)90248-4.

[77] Jacob Beutel, Harold L Kundel, and Richard L Van Metter. *Handbook of medical imaging*, volume 1. Spie Press, 2000.

[78] Heang-ping Chan and Kunio Doi. Energy and angular dependence of x-ray absorption and its effect on radiographic response in screen-film systems. *Physics in Medicine & Biology*, 28(5):565–579, 1983.

[79] Charles E Metz and Carl J Vyborny. Wiener spectral effects of spatial correlation between the sites of characteristic x-ray emission and reabsorption in radiographic screen-film systems. *Physics in Medicine & Biology*, 28(5):547–564, 1983.

[80] J Yao and I A Cunningham. Parallel cascades : New ways to describe noise transfer in medical imaging. *Medical physics*, 28(10):2020–2038, 2001. doi: https://doi.org/10.1118/1.1405842.

[81] Adrian Howansky, Boyu Peng, A R Lubinsky, and Wei Zhao. Deriving depth-dependent light escape efficiency and optical Swank factor from measured pulse height spectra of scintillators. *Medical Physics*, 44(3):847–860, 2016. doi: 10.1002/mp.12083.

[82] E. W. Marchand. Derivation of the Point Spread Function from the Line Spread Function. *Journal of the Optical Society of America*, 54(7):915, 1964. ISSN 0030-3941. doi: 10.1364/josa.54.000915.

[83] R. Clark Jones. On the Point and Line Spread Functions of Photographic Images. *Journal of the Optical Society of America*, 48(12):934–937, 1958. ISSN 0030-3941. doi: 10.1364/josa.48.000934.

[84] C. B. Johnson. Point-Spread Functions, Line-Spread Functions, and Edge-Response Functions Associated with MTFs of the Form exp $[(-\omega/\omega_c)^n]$. *Applied Optics*, 12(5):1031, 1973. ISSN 0003-6935. doi: 10.1364/ao.12.001031.

[85] Natalie Baddour. Chapter 1 - two-dimensional fourier transforms in polar coordinates. In Peter W. Hawkes, editor, *Advances in Imaging and Electron Physics*, volume 165, pages 1–45. Elsevier, 2011. doi: https://doi.org/10.1016/B978-0-12-385861-0.00001-4. URL `https://www.sciencedirect.com/science/article/pii/B9780123858610000014`.

[86] Ho-hui Hsieh, Yu-ching Ni, Sheng-pin Tseng, Fan-pin Tseng, and Liang-cheng Chen. Compound Poisson Noise Verification for X-ray Flat Panel Imager. In *2015 IEEE International Conference on Imaging Systems and Techniques (IST)*, pages 1–5, 2015. ISBN 9781479986330. doi: 10.1109/IST.2015.7294576.

[87] M Maolinbay, Y El-mohri, L E Antonuk, and K Jee. Additive noise properties of active matrix flat-panel imagers. *Medical Physics*, 27(9):1841–1854, 2000. doi: 10.1118/1.1286721.

[88] J. Alles and R. F. Mudde. Beam hardening: Analytical considerations of the effective attenuation coefficient of x-ray tomography. *Medical Physics*, 34(7):2882–2889, 2007. ISSN 00942405. doi: 10.1118/1.2742501.